COMPUTATION OF HEAT TRANSFER IN TURBINE ROTOR BLADE COOLING CHANNELS WITH ANGLED RIB TURBULATORS

By

Guy Austin Flynt

Approved:

Kidambi Sreenivas Research Professor of Computational Engineering (Chair)	Robert S. Webster Associate Research Professor of Computational Engineering (Committee Member)
W. Roger Briley Professor of Computational Engineering (Committee Member)	Eric McFarland Research Professor of Engineering (Committee Member)
William H. Sutton Dean of the College of Engineering and Computer Science	Jeral Ainsworth Dean of the Graduate School

COMPUTATION OF HEAT TRANSFER IN TURBINE ROTOR BLADE COOLING CHANNELS WITH ANGLED RIB TURBULATORS

By

Guy Austin Flynt

A Thesis Submitted to the Faculty of the University
of Tennessee at Chattanooga in Partial
Fulfillment of the Requirements of the
Degree of Master's of Science

The University of Tennessee, Chattanooga
Chattanooga, Tennessee

May 2013

ABSTRACT

The effects of rotation and Reynolds number on heat transfer in rotating two-pass square and rectangular channels with smooth walls and walls with 45° angled and V-shaped rib turbulators were investigated numerically using an unstructured, incompressible, Reynolds-averaged Navier-Stokes flow solver. The influence of 45° angled ribs and channel orientation on the local Nusselt number ratios for leading and trailing surfaces in a two-pass square channel (AR=1) are compared to experimental data for Reynolds numbers from 5,000 to 25,000 and dimensionless rotation numbers from 0.0 to 0.118. The influence of V-shaped ribs and channel orientation on the local Nusselt number ratios for leading and trailing surfaces in a two-pass rectangular channel (AR=2) are compared to experimental data for Reynolds numbers from 5,000 to 40,000 and rotation numbers from 0.0 to 0.210. It is concluded that rotation causes significant changes to the local Nusselt number ratio distribution relative to stationary conditions. Generally, the first pass trailing and second pass leading surfaces have increased local Nusselt number ratios due to the secondary flow impingement induced by rotation. Alternatively, the first pass leading and second pass trailing surface Nusselt number ratios tend to decrease with increased rotation.

TABLE OF CONTENTS

LIST OF TABLES

LIST OF FIGURES

LIST OF SYMBOLS

τ_w, wall shear stress ($\mu\ \partial u/\partial y|_{y=0}$), (Pa)

u^*, friction velocity $\left(\sqrt{\frac{\tau_w}{\rho}}\right)$

y^+, nondimensional wall distance $(u^* y/\nu)$

α_T, coefficient of thermal expansion

$\bar{R}$, mean rotational radius of channel (m)

β, angle of channel orientation with respect to axis of rotation

$\frac{\Delta\rho}{\rho}$, inlet coolant-to-wall density ratio $((T_w - T_{bi})/T_w)$

$\hat{p}$, combined pressure (N/m^2)

μ, viscosity of air $(kg/m \cdot s)$

ν, kinematic viscosity, μ/ρ (m^2/s)

Ω, rotational speed (rad/s)

$\overrightarrow{\nabla}$, partial differential vector operator $\left(\frac{\partial}{\partial x}, \frac{\partial}{\partial y}, \frac{\partial}{\partial z}\right)$

Φ_{RL}, inviscid source term

$\Phi_{v_{ij}}$, viscous source term

ρ, density of air (kg/m^3)

τ_{ij}, stress tensor

$\tilde{\Lambda}$, diagonal matrix with eigenvalues on diagonal

$\tilde{\sigma}$, deviatoric part of Stokes tensor

$\tilde{A}$, flux Jacobian matrix

$\tilde{I}$, identity matrix

$\tilde{L}$, left eigenvalue matrix

$\tilde{R}$, right eigenvalue matrix

$\underline{b}$, gravitational body force $\left(-\nabla \cdot (g x_2 \tilde{I})\right)$

$\underline{u}$, velocity vector (u, v, w)

Υ, temperature vector

$\vec{F_v}$, viscous flux vector

$\vec{F}$, inviscid flux vector

$\vec{n}$, unit normal vector (n_x, n_y, n_z)

$\vec{x_i}$, coordinate location of node i

A, surface area of the copper plate (m^2)

A_c, cross-sectional area of channel (m^2)

AR, Aspect Ratio (Width : Height)

C_p, specific heat at constant pressure, $\frac{\partial h}{\partial T}|_p$ $\left(\frac{J}{kg\ K}\right)$

D_h, hydraulic diameter of rectangular channel, $4 \cdot A_c / P_w$ (m)

e, rib height (m)

Fr_∞, Froude number, $\left(\frac{u_\infty}{\sqrt{gL}}\right)$

g, acceleration due to gravity $\left(\frac{m}{s^2}\right)$

Gr_∞, Grashoff number $\left(\frac{g\alpha_T(T_w - T_\infty)L^3}{\nu_\infty^2}\right)$

h, convective heat transfer coefficient (W/m^2K)

k, thermal conductivity of coolant (W/mK)

N_{iters}, number of time-step iterations taken by flow solver

Nu, local Nusselt number, (hD_h/k)

Nu_s, Nusselt number in fully-developed, non-rotating smooth tube (hD_h/k)

P, rib pitch (m)

p, pressure (N/m^2)

P_w, wetted perimeter of channel (m)

Pe_∞, Peclet number, $(Re_\infty \cdot Pr_\infty)$

Pr, Prandtl number, viscous to thermal diffusion ratio $(\mu C_p/k)$

Q, solution variable matrix

q_s'', surface heat flux (W/m^2)

Re, Reynolds number $(\rho V D_h/\mu)$

Ro, rotation number $(\Omega D_h/V)$

T, temperature (K)

t, time (s)

T_∞, freestream temperature (K)

T_{bx}, average bulk flow temperature at streamwise x-located cross-section (K)

T_w, local wall temperature (K)

V, average axial flow velocity (m/s)

CHAPTER 1

INTRODUCTION

To improve thermal efficiency and achieve higher power density, the trend in advanced gas turbine design is toward high entry gas temperatures that exceed the melting point of the material. To lower thermal stresses and creep rates, highly sophisticated cooling technologies, including internal airfoil cooling, are employed for blades and vanes of advanced gas turbine engines. Internal cooling is achieved by passing the coolant through several rib-enhanced serpentine passages inside the blades and extracting the heat from the outside of the blades. Through analytical and experimental studies, the aim of this study is to gain insight regarding the effect of rotation on heat transfer in turbine blade passages, to develop a broad database for heat transfer in rotating coolant passages, and to improve computational techniques and develop correlations that can be useful to the gas turbine industry for turbine blade design. Among the primary goals of the Integrated High Performance Turbine Engine Technology (IHPTET) initiative was the requirement that turbines should operate near that of stoichiometric fuel-to-air mixture ratios with inlet temperatures in the range of $2,200 - 2,500\ K$ ($3,500 - 4,000$°F), while using total coolant flows less than 5 percent of engine air flow rate [1]. A further complication of the internal coolant flow field is that "rotation of turbine blade cooling passages gives rise to Coriolis and buoyancy forces, which can significantly alter the local heat transfer in the internal coolant passages due to the development of cross-stream (Coriolis) as well as radial (buoyant) secondary flows" [2].

Gas Turbine Heat Transfer and Cooling Technology, the book by Han, et al. [3], serves as a comprehensive reference for heat-transfer and cooling issues related to turbine airfoils. Han, et al. [4] studied the effect of rib angle orientation on local mass transfer distribution in

a three-pass rib-roughened channel. Naphthalene-coated ribs were attached to two opposite walls of the cooling passages to model heat transfer emanating predominantly from the pressure and suction surfaces of the turbine blade. It was concluded that parallel ribs performed better than crossed rib configurations. It was found that, for the smooth channel cases, the average mass transfer coefficients in the second pass where 60% higher than those found in the first pass. Also, the angled ribs provided higher mass transfer coefficients than the transverse ribs. It was observed that the "rib angle, rib orientation, and the sharp 180° turn significantly affected the local heat/mass transfer distributions. The combined effects of these parameters increased and decreased the local heat/mass coefficients after the sharp 180° turns" [4].

Han, et al. [5] studied the effect of the rib angle orientation on local heat transfer distributions and pressure drop in a non-rotating square channel with opposite, in-line ribbed walls. They found that the 60° and 45° V-shaped ribs performed better than the 60° and 45° crossed ribs or 90° transverse ribs. "The V-shaped rib produces the highest heat transfer augmentation while the inverted V-shaped rib generates the greatest pressure drop" [5].

Ekkad and Han [6] studied heat transfer distributions in two-pass square channels with rib turbulators using a transient liquid crystal technique. Four configurations of 90° parallel, 60° parallel, 60° V-shaped, and 60° inverted V-shaped ribs were discussed. They noted that "The periodic ribs break the laminar sublayer and create local wall turbulence due to flow separation and reattachment between the ribs, greatly enhancing the heat transfer" [6]. They also found that Nusselt number ratios are highest on top of the ribs and lowest immediately before and after the ribs for all ribbed channels.

Rotation of turbine blade cooling passages gives rise to Coriolis and buoyancy forces. Wagner, et al. [7, 8] studied heat transfer in rotating passages with smooth walls and radial outward flow. The results indicate the Coriolis forces caused the leading and trailing side heat transfer to vary by factors as large as five, and effects of buoyancy, which caused heat transfer to increase by as much as a factor of two [7]. They concluded that the first pass channel, with

radially outward flow, created a thinner boundary layer on the trailing surface and a thicker boundary layer on the leading surface resulting in increased heat transfer and decreased heat transfer, respectively. The second pass channel showed opposite characteristics. With flow coming radially inward, the reversal of the Coriolis force direction causes the leading surface Nusselt number ratios in the second pass to be higher than the corresponding trailing surface Nusselt number ratios. Taslim, et al. [9] conducted an experimental investigation of heat transfer coefficients in a spanwise rotating channel with two opposite rib-roughened walls. They concluded that channels with low rib blockage ratios had increased heat transfer coefficients in both the stationary and rotating cases.

Johnson, et al. [2] studied heat transfer in rotating serpentine square channels with trips skewed to the flow. A parametric experiment was performed to investigate the effects of buoyancy and Coriolis forces on the heat transfer distribution of four-pass square channels with 45° skewed ribs. It was concluded that heat transfer ratios are well correlated by a $Nu \propto Re^{0.8}$ relationship. The density ratio was less of a factor in heat transfer for skewed trips where the flow is well mixed. They also noted that the rotation number correlates heat transfer ratios better for skewed rib cases rather than smooth tube flows.

The effect that model orientation has on heat transfer in rotating serpentine channels was also studied by Johnson, et al. [1]. The channels were subjected to rotation in both directions to simulate coolant passages with rearward or forward flow of coolant. They concluded that both the rotation and channel orientation could change the leading and trailing surface heat transfer coefficients of the ribbed channel [10]. At typical flow conditions, the heat transfer on the leading surfaces for flow outward in the first passage with smooth walls was twice as much for the model at 45° compared to the model rotating orthogonally [1]. The effects of buoyancy and Coriolis forces on heat transfer in the rotating passage were decreased with the model at 45°, compared to the results at 0°. The heat transfer in the turn regions and immediately downstream of the turns in the second passage, with flow inward, and in the third passage, with flow outward, was also a function of model orientation; with differences

as large as 40 to 50 percent occurring between the model orientations with forward flow and rearward flow of coolant [1]. It was also concluded that the model orientation has little effect in the second leg of the channel where flow is flowing inward toward the center of rotation.

Han, et al. [11] studied uneven wall temperature effects on local heat transfer in a rotating two-pass square channel with smooth walls. It was found that rotation caused Nusselt number ratios for the first pass trailing and second pass leading surfaces to increase. The effect of uneven wall temperature was to enhance the heat transfer coefficients in the rotating channel compared to the uniform wall temperature boundary conditions. The cause of this heat transfer enhancement is attributed to the interactions between rotation-induced secondary flows and uneven wall temperatures [11].

Parsons, et al. [12, 13] investigated wall heating effect and channel orientation on local heat transfer in a rotating two-pass square channel with ribbed walls. The rotating ribbed wall heat transfer coefficients were found to be two to three times higher than their corresponding rotating smooth wall values. The difference between the leading and trailing wall Nusselt number ratios was found to increase with increasing rotation number. The cause for this was that the rotation creates a thinner boundary layer on the trailing wall and a thicker boundary layer on the leading wall [12]. The leading wall Nusselt number ratios in the second pass were higher than the trailing wall Nusselt number ratios due to a reversal of the Coriolis force direction. The channel orientation change from orthogonal, $\beta = 90°$, to angled, $\beta = 135°$, caused the effects of the cross-stream flow and Coriolis force on heat transfer to be reduced. Parsons, et al. [13] also isolated the effects that model orientation and rib angle have on local heat transfer in a rotating two-pass square channel with rib turbulators. When subjected to angled rotation, the Nusselt number ratios in the channel with 60° angled ribs were up to 40% higher than the channel using 90° ribs.

Dutta and Han [14] investigated the local heat transfer in rotating smooth and ribbed, two-pass square channels with three channel orientations. They concluded that rotation causes destabilization (enhancement of turbulence) on one side and stabilization (suppression

of turbulence) on the other. The enhanced turbulence caused greater heat transfer from the destabilized walls than from the stabilized walls. The Nusselt number ratios of ribbed, stabilized sides show a mixed dependence on the rotation number. At lower rotation numbers, the Nusselt number ratios on the ribbed, stabilized sides increased with an increase in rotation number. This increase is followed by a decrease with a further increase in rotation number [14].

Park and Lau [15] and Park, et al. [16] conducted experimental work using Naphthalene sublimation to determine the effects of channel orientation, Coriolis force, and sharp 180° turn on local heat/mass transfer distributions in a two-pass square channel. They found that the geometry of the sharp turn dominates the local mass transfer distributions in the turn and immediately downstream of the turn. The combined effect of the turn and rotation causes a strong swirling flow and flow impingement near the outer edges of the leading wall in the turn and immediately downstream of the turn.

Huh, et al. [17] studied the effect of rib height on heat transfer in a narrow, two-pass rectangular channel (AR = 1:4) with a sharp entrance at high rotation numbers. Because of the large distance between the leading and trailing surfaces in the narrow channel, the heat transfer results are very similar for both blockage ratios (e/D_h). Their correlations show that the buoyancy parameter is a reliable predictor of heat transfer at high rotation numbers.

Taslim, et al. [18] conducted an experimental investigation of heat transfer in an orthogonally rotating channel roughened with 45 degree criss-cross ribs on two opposite walls. They found that rotational effects are more pronounced in rib turbulator channels with high aspect ratios and low blockage ratios. In these cases, "a steady increase in heat transfer coefficient is observed on the trailing side as rotation number increases while the heat transfer coefficient on the leading side shows a steady decrease with rotation number" [18].

Fu, et al. [19] studied heat transfer in two-pass rotating rectangular channels (AR=1:2 and AR=1:4) with 45° angled rib turbulators. They showed that the Nusselt number ratio

decreases with increasing Reynolds number in both non-rotating and rotating cases. They also concluded that rotation has a relatively small effect in the second pass of narrow channels. This is attributed to "the large width between leading and trailing walls for the lower aspect ratio channels" [19].

Bonhoff, et al. [20] conducted an experimental and numerical study of developed flow and heat transfer in coolant channels with 45 degree ribs. The experimental study was conducted using a stereoscopic digital PIV measurements system to measure local velocities. The numerical study used Navier-Stokes regimes with three sets of wall and turbulence models. The experimental measurements and numerical results were in good qualitative agreement with a difference of 12% using the Reynolds-stress turbulence model (RSM). The comparison showed that the RSM results were "more consistent with the experimental results than the $k - \epsilon$ results with and without wall functions" [20].

Iacovides, et al. [21] determined experimentally, using laser doppler anemometry (LDA), the flow and heat transfer in a rotating U-bend with 45° ribs. The angled ribs induced streamwise vortices which enhanced mixing. This dynamic mixing meant that the flow and average Nusselt numbers were relatively unaffected by rotation. However, it was noted that rotation causes "local hot or cold spots which in an actual blade would mean large temperature gradients with consequent stress concentrations" [21].

Han and Chen [22] provided a summary of experimental and numerical research into turbine blade internal cooling passages with rib turbulators. They highlighted the ability of Reynolds averaged Navier-Stokes (RANS) models to resolve the complex three-dimensional flow physics that exist in rotating turbine blade internal coolant passages.

Murata and Mochizuchi [23] compared laminar and turbulent heat transfer in a stationary square duct with either transverse or angled rib turbulators. The heat transfer in the channel was numerically simulated using a second-order finite difference method. In the turbulent cases using both 60° and 90° ribs, the flow reattachment at the midpoint between the ribs and the unsteady reverse flow in front of the rib formed high values of the time-averaged heat

transfer. For the laminar flow case, the low momentum fluid near the ribbed wall resulted in the ribs having a smaller effect on the flow field.

Viswanathan and Tafti [24] conducted a detached eddy simulation (DES) of turbulent flow and heat transfer in a two-pass internal cooling duct. The simulation was applied to a stationary duct with 90° ribs. The solver used a generalized incompressible regime with direct numerical simulation and large eddy simulation of turbulence using a DES version of the $k - \omega$ model. "The flow in the inter-rib spacing is dominated by vortex enhanced heat transfer in front of the rib, in the reattachment region behind the rib and at the junction of the rib with the smooth walls" [24].

Sewall and Tafti [25] conducted a large eddy simulation (LES) of flow and heat transfer in the developing flow region of a rotating gas turbine blade internal cooling duct with Coriolis and buoyancy forces. The geometry consisted of a rotating straight channel with 90° ribs. The solver used a generalized incompressible regime with direct numerical simulation and large eddy simulation of turbulence similar to that used by Viswanathan and Tafti [24]. They studied why heat transfer decreased and then increased on the leading wall as the buoyancy parameter increases. LES results show that the initial decrease in heat transfer is a result of larger separated regions at the leading wall. However, as the separated region spans the full pitch between ribs with an increase in buoyancy parameter, it leads to increased turbulence and increased entrainment of mainstream fluid, which is redirected toward the leading wall by the presence of a rib.

Valentino, et al. [26] compared heat transfer and friction augmentation for symmetric and non-symmetric wedge turbulators on two opposite walls of a narrow rectangular duct (AR = 2). The Nusselt number augmentation of the side walls was recorded to determine thermal performance of each wedge geometry. They found that the non-symmetric wedge shapes produced 30 to 50 percent lower heat transfer augmentations than the symmetric wedges, but benefited from 20 to 50 percent lower friction factor augmentations.

Taslim and Spring [27] and Kamali, et al. [28] studied the effects of turbulator profile and spacing on heat transfer and friction in a channel. It was concluded that the optimum pitch-to-height ratio is around 8 for 90° square turbulators. They noted the relative differences in heat transfer behavior due to turbulator shape and pitch-to-height ratio changes.

Mahadevan, et al. [29] showed that heat transfer can be increased with high blockage ratio channels. However this increase in heat transfer comes at the expense of larger pressure drops. Liou, et al. [30] studied turbulent transport phenomena in a channel with periodic rib turbulators. They found that increasing the pitch to rib-height ratio (P/e) beyond 10 causes a decrease in heat transfer augmentation. The maximum observed increase in average Nusselt number was 94% for P/e = 10. Rallabandi, et al. [31] presented heat transfer and pressure drop correlations for square channels with 45° ribs at high Reynolds numbers ranging from 30,000 to 400,000. Their results showed higher heat transfer coefficients occurred at smaller values of P/e and larger values of e/D, though at the cost of higher friction losses [31].

The remainder of this thesis is laid out as follows: The following chapter describes the numerical analysis relating to the fundamental governing equations that apply to internal coolant flow heat transfer. The governing equations are then implemented in their nondimensional form and discretized for application in the flow solver. This is followed by a detailed description of the experimental test apparatus used by Al-Hadhrami [10]; whose Nusselt number ratio results are used for comparison. A description of the heated channel is given with commentary on the conceptual secondary flow vortices induced by rotation and rib arrangement. A data reduction analysis is presented to inform how the Nusselt number ratio is derived from related physical properties. Numerical results are then presented for the two-pass square channel. Test cases include internal coolant flows with Reynolds number ranging from 5,000 to 25,000 and subjected to no rotation, orthogonal rotation ($\beta = 90°$), and angled rotation ($\beta = 135°$). The numerical results for a two-pass rectangular channel are then discussed. Three channel setups are examined including a smooth channel, Case (a), and two configurations, Case (c) and (d), utilizing V-shaped and inverted V-shaped ribs. Finally,

conclusions are made for both square and rectangular channels. Limitations of present work are presented and recommendations for future work are suggested.

CHAPTER 2

GOVERNING EQUATIONS AND NUMERICAL APPROACH

Fundamental Equations

This chapter describes the governing equations implemented in the numerical flow solver. The governing equations are derived from the three-dimensional Navier-Stokes equations with the energy equation coupled in. The continuity equation is shown in Equation 2.1 which disregards any change in density (incompressible assumption):

$$\vec{\nabla} \cdot \underline{u} = 0 \tag{2.1}$$

Conservation of momentum is shown in Equation 2.2:

$$\rho \frac{\partial \underline{u}}{\partial t} + \rho \vec{\nabla} \cdot (\underline{u}\ \underline{u}) = -\vec{\nabla} \cdot \left(p\tilde{I} \right) + \vec{\nabla} \cdot \tilde{\sigma} + \rho \underline{b} \tag{2.2}$$

Finally, the conservation of energy is shown in Equation 2.3:

$$\rho C_p \frac{\partial T}{\partial t} + \rho C_p \vec{\nabla} \cdot (\underline{u} T) = \vec{\nabla} \cdot (k \nabla T) \tag{2.3}$$

where $\underline{u}$ is inertial velocity, ρ is density, p is pressure, T is temperature $\tilde{I}$ is the identity matrix, $\tilde{\sigma}$ is the deviatoric part of the Stokes tensor, $\underline{b}$ is the body force per unit mass, k is the thermal conductivity, and C_p is the specific heat at constant pressure. The momentum equation includes gravity as the only body force taken into account. Therefore, the body force per unit mass is defined as

$$\underline{b} = -\vec{\nabla} (g x_2) = -\vec{\nabla} \cdot \left(g x_2 \tilde{I} \right) \tag{2.4}$$

Density is treated as a constant, except in the body force term, where a Boussinesq approximation is employed. A truncated Taylor series expansion of density yields:

$$\begin{aligned} \rho\left(T\right) &= \rho_{\infty} + \left(\frac{\partial \rho}{\partial T}\right)_{p} \left(T - T_{\infty}\right) \\ &= \rho_{\infty}\left[1 - \alpha_{T}\left(T - T_{\infty}\right)\right] \end{aligned} \tag{2.5}$$

where α_T, the coefficient of thermal expansion for a fluid at constant pressure, is defined as

$$\alpha_{T} = -\frac{1}{\rho_{\infty}}\left(\frac{\partial \rho}{\partial T}\right)_{p}$$

The expression for ρ may be rewritten as

$$\rho = \rho_{\infty}\left(1 + \rho'\right) \tag{2.6}$$

where

$$\rho' = -\alpha_{T}\left(T - T_{\infty}\right)$$

With these formulations, we may rewrite the momentum equation as

$$\frac{\partial \underline{u}}{\partial t} + \vec{\nabla} \cdot \left(\underline{u}\ \underline{u}\right) + \frac{1}{\rho_{\infty}} \vec{\nabla} \cdot \left(\hat{p}\tilde{I} - \tilde{\sigma}\right) = -\rho' \vec{\nabla} \cdot \left(g x_{2} \tilde{I}\right) \tag{2.7}$$

where $\hat{p} = p + \rho_{\infty} g x_2$, which absorbs hydrostatic pressure into the pressure definition. Finally, using the artificial compressibility approach [32], a fictitious time derivative of pressure is added to the continuity equation which is then expressed as:

$$\frac{1}{\beta}\frac{\partial \hat{p}}{\partial t} + \vec{\nabla} \cdot \underline{u} = 0 \tag{2.8}$$

where β is the artificial compressibility parameter. This parameter is often set in the range from 5 to 15 [33]. Together, equations 2.8, 2.7, and 2.3 form the governing equations for the cases considered here.

Nondimensional Implementation

Nondimensionalization of the governing equations can scale the variables to show relative magnitudes, as well as aid in iterative convergence stability. "Since our basic equations of motion are extremely difficult to analyze in general, we should cast them in their most efficient form, thereby increasing the usefulness of whatever solutions we find. This is accomplished by nondimensionalizing the equations and boundary conditions" [34]. Assuming constant C_p and C_v which is approximately true for all non-reacting gas flows with relatively small changes in temperature, our four variables p, ρ, $\underline{u}$, and T, will depend upon space and time and eight parameters that occur in the basic equations and boundary conditions:

$$\underline{u} \text{ or } p \text{ or } \rho \text{ or } T = f(x_m, t, \mu, k, g, C_p, T_w, q_w, l, \mathcal{T}) \tag{2.9}$$

Selection of *constant* reference properties appropriate to the flow include:

1. Reference velocity u_∞ (freestream velocity)

2. Reference length L (duct diameter, D_h, for internal flows)

3. Freestream properties $p_\infty,\ \rho_\infty,\ T_\infty,\ \mu_\infty,\ k_\infty$ [34].

Dimensionless variables are now defined and denoted by an asterisk.

$$
\begin{aligned}
x^* &= \frac{x}{L} & p^* &= \frac{p - p_\infty}{\rho_\infty u_\infty^2} \\
y^* &= \frac{y}{L} & T^* &= \frac{T - T_\infty}{T_w - T_\infty} \\
z^* &= \frac{z}{L} & \rho^* &= \frac{\rho}{\rho_\infty} \\
t^* &= t\frac{u_\infty}{L} & \mu^* &= \frac{\mu}{\mu_\infty} \\
u^* &= \frac{u}{u_\infty} & k^* &= \frac{k}{k_\infty} \\
\tilde{\sigma}^* &= \frac{L}{\mu_\infty u_\infty}\tilde{\sigma}
\end{aligned}
\tag{2.10}
$$

The nondimensionalized variables also create new operators:

$$
\begin{aligned}
div^*(\cdot) = \vec{\nabla}^* \cdot (\cdot) &= \frac{1}{L}\frac{\partial(\cdot)}{\partial x_m^*} \cdot \hat{i}_m,\ m = 1,2,3 \\
grad^*(\cdot) = \vec{\nabla}^* (\cdot) &= \frac{1}{L}\frac{\partial(\cdot)}{\partial x_m^*}\hat{i}_m,\ m = 1,2,3
\end{aligned}
\tag{2.11}
$$

The above variables are used to create dimensionless parameters:

$$
\begin{aligned}
\text{Reynolds number}: \quad Re_\infty &= \frac{\rho_\infty u_\infty L}{\mu_\infty} \\
\text{Froude number}: \quad Fr_\infty &= \frac{u_\infty}{\sqrt{gL}} \\
\text{Prandtl number}: \quad Pr_\infty &= \frac{\mu_\infty C_p}{k_\infty} \\
\text{Peclet number}: \quad Pe_\infty &= Re_\infty Pr_\infty = \frac{\rho_\infty C_p u_\infty L}{k_\infty} \\
\text{Grashoff number}: \quad Gr_\infty &= \frac{g\alpha_T (T_w - T_\infty) L^3}{\nu_\infty^2}
\end{aligned}
\tag{2.12}
$$

With the * superscripts dropped for clarity, the nondimensionalized equations are expressed as

Continuity

$$\frac{1}{\beta}\frac{\partial \hat{p}}{\partial t} + \vec{\nabla} \cdot \underline{u} = 0 \tag{2.13}$$

Momentum

$$\frac{\partial \underline{u}}{\partial t} + \vec{\nabla} \cdot (\underline{u}\ \underline{u}) + \vec{\nabla} \cdot \left(\hat{p}\tilde{I} - \frac{1}{Re_\infty}\tilde{\sigma} \right) = \frac{Gr_\infty}{Re_\infty^2} T\ \vec{\nabla} \cdot \left(x_2 \tilde{I} \right) \tag{2.14}$$

Energy

$$\frac{\partial T}{\partial t} + \vec{\nabla} \cdot (\underline{u} T) = \vec{\nabla} \cdot \left(\frac{k}{Pe_\infty} \nabla T \right) \tag{2.15}$$

where $\hat{p} = p + x_2/Fr_\infty^2$. With the variables nondimensionalized according to the previous definitions, the variables in the following equations may be assumed to be nondimensional unless otherwise stated. The unsteady, three-dimensional, nondimensionalized incompressible Navier-Stokes equations in Cartesian coordinates can be written in conservative and integral form as

$$\frac{\partial}{\partial t}\int_\Omega Q\ dV + \int_{\partial\Omega} F \cdot \vec{n}\ dA - \int_{\partial\Omega} F_v \cdot \vec{n}\ dA - \frac{Gr_\infty}{Re_\infty^2}\int_\Omega \Upsilon\ dV = 0 \tag{2.16}$$

where

$$Q = \begin{bmatrix} p \\ u \\ v \\ w \\ T \end{bmatrix},\ F = \begin{bmatrix} \beta\theta \\ u\theta + \frac{pn_x}{\rho} \\ v\theta + \frac{pn_y}{\rho} \\ w\theta + \frac{pn_z}{\rho} \\ T\theta \end{bmatrix} = \begin{bmatrix} \beta u & \beta v & \beta w \\ u^2 + \frac{p}{\rho} & uv & uw \\ uv & v^2 + \frac{p}{\rho} & vw \\ uw & vw & w^2 + \frac{p}{\rho} \\ Tu & Tv & Tw \end{bmatrix} \begin{bmatrix} n_x \\ n_y \\ n_z \end{bmatrix} \tag{2.17}$$

$$F_v = \frac{1}{\rho}\begin{bmatrix} 0 \\ \tau_{xx}n_x + \tau_{xy}n_y + \tau_{xz}n_z \\ \tau_{xy}n_x + \tau_{yy}n_y + \tau_{yz}n_z \\ \tau_{xz}n_x + \tau_{yz}n_y + \tau_{zz}n_z \\ q_x n_x + q_y n_y + q_z n_z \end{bmatrix} = \frac{1}{\rho}\begin{bmatrix} 0 & 0 & 0 \\ \tau_{xx} & \tau_{xy} & \tau_{xz} \\ \tau_{xy} & \tau_{yy} & \tau_{yz} \\ \tau_{xz} & \tau_{yz} & \tau_{zz} \\ q_x & q_y & q_z \end{bmatrix}\begin{bmatrix} n_x \\ n_y \\ n_z \end{bmatrix}, \ \Upsilon = \begin{bmatrix} 0 \\ 0 \\ T \\ 0 \\ 0 \end{bmatrix} \tag{2.18}$$

and

$$\begin{aligned} \tau_{xx} &= \tfrac{2\mu}{Re_\infty}\tfrac{\partial u}{\partial x} \\ \tau_{yy} &= \tfrac{2\mu}{Re_\infty}\tfrac{\partial v}{\partial y} \\ \tau_{zz} &= \tfrac{2\mu}{Re_\infty}\tfrac{\partial w}{\partial z} \end{aligned} \tag{2.19}$$

$$\begin{aligned} \tau_{xy} = \tau_{yx} &= \tfrac{\mu}{Re_\infty}\left(\tfrac{\partial u}{\partial y} + \tfrac{\partial v}{\partial x}\right) \\ \tau_{xz} = \tau_{zx} &= \tfrac{\mu}{Re_\infty}\left(\tfrac{\partial u}{\partial z} + \tfrac{\partial w}{\partial x}\right) \\ \tau_{yz} = \tau_{zy} &= \tfrac{\mu}{Re_\infty}\left(\tfrac{\partial v}{\partial z} + \tfrac{\partial w}{\partial y}\right) \end{aligned} \tag{2.20}$$

$$\begin{aligned} q_x &= \tfrac{k}{Pe_\infty}\tfrac{\partial T}{\partial x} \\ q_y &= \tfrac{k}{Pe_\infty}\tfrac{\partial T}{\partial y} \\ q_z &= \tfrac{k}{Pe_\infty}\tfrac{\partial T}{\partial z} \end{aligned} \tag{2.21}$$

$$\theta = un_x + vn_y + wn_z$$

A discretization of the differential and integral operators with respect to space and time results in the following numerical formulation for a genaral node i:

$$V_i \frac{\Delta Q_i}{\Delta t_i} + \sum_j \left(\Phi_{ij} \cdot \hat{n}_{ij}\right) S_{ij} - \sum_j \left(\Phi_{v_{ij}} \cdot \hat{n}_{ij}\right) S_{ij} - \frac{Gr_\infty}{Re_\infty^2} V_i \Upsilon_i = 0 \tag{2.22}$$

where V_i is the volume, Δt_i is the timestep, and Υ_i is the source term vector. Φ_{ij} and $\Phi_{v_{ij}}$ are the discretized inviscid and viscouse flux contributions respectively, $\hat{n}_{ij}$ is the outward pointing unit normal vector, and S_{ij} is the area vector associated with the edge connecting node i and j[35]. The summation over j includes all the nodes surrounding node i. The inviscid terms are determined by

$$\Phi_{RL} = \frac{1}{2}\left[(F(Q_L) + F(Q_R)) - \tilde{A}(Q_R, Q_L)(Q_R - Q_L)\right]$$

where Q_R and Q_L are the dependent variable vectors evaluated at the node on the right and left hand side of the edge, respectively. $F(Q_R)$ and $F(Q_L)$ are the inviscid flux vectors. $\tilde{A}$ is the flux Jacobian matrix which can be factored by the following formula

$$\tilde{A} = \tilde{R}\tilde{\Lambda}\tilde{L}$$

where $\tilde{R}$ and $\tilde{L}$ are the right and left eigenvector matrices, and $\tilde{\Lambda}$ is a diagonal matrix with the absolute values of the eigenvalues on the diagonal. The viscous terms are determined using the directional derivative method. The viscous terms are numerically approximated using the formula:

$$\Phi_{v_{ij}} = \frac{1}{Re_\infty} \sum_j C_j (Q_j - Q_i)$$

where C_j is a matrix of coefficients used to emulate the viscous characteristics of the fluid; with j being the index of any neighboring node connected to node i. We obtain higher order spatial accuracy by including information from each neighboring node:

$$Q_L = Q_i + \vec{\nabla} Q_i \cdot (\vec{x_f} - \vec{x_i})$$
$$Q_R = Q_j + \vec{\nabla} Q_j \cdot (\vec{x_f} - \vec{x_j}) \tag{2.23}$$

where $\vec{x_f}$ is the coordinate vector of the midpoint of the edge connecting node i to node j, and $\vec{x_i}$ and $\vec{x_j}$ are the coordinate vectors for each node.

Flow Solver

The flow solver applied to internal coolant flow heat transfer is implemented using the *Tenasi* code which has been developed in-house at the SimCenter: National Center for Computational Engineering. The *Tenasi* flow solver employs a finite volume, implicit scheme with high resolution fluxes and a Newton iteration procedure for time accuracy. The solver is node-centered with control volumes assembled from a median dual surrounding each vertex of the mesh. The unstructured algorithm solves systems of field equations on meshes with mixed element types. Isotropic tetrahedral elements are employed in regions removed from surfaces. Prisms and hexahedral elements are extruded from the triangular or quad surface meshes where resolution of the boundary layer is necessary.

The *Tenasi* framework is designed to solve field equations cast into the following integral conservative form: Convective fluxes in the governing field equations are evaluated using a Roe-averaged flux difference splitting approach. The gradients in the diffusive terms are evaluated using a local directional derivative technique. Higher order accuracy is achieved via the use of variable extrapolation using gradients computed via a least squares formulation. Time stepping is accomplished via a fully implicit backwards Euler approximation, where the resulting linear system is solved by an LU/SGS point iterative process.

The unstructured solver is parallelized using the MPI message passing library for the required inter-subdomain communication. A block-Jacobi type updating of the subdomain

interfaces provides efficient parallelization. A small incremental cost is incurred due to the linear subiterations required to recover the convergence rate of the sequential algorithm.

A suite of turbulence models are available in *Tenasi*. In this study, the two-equation $k-\epsilon/k-\omega$ hybrid turbulence model was used for all computations. This model has shown high performance for wall bounded flows in the absence of high adverse pressure gradients. The model equations are integrated through the viscous sublayer, which requires high mesh resolution near walls.

CHAPTER 3

DESCRIPTION OF TEST SECTION

Test Section Apparatus

Figure 3.1 on the following page shows a schematic of the experimental apparatus used by Al-Hadhrami, et al. [10] and Han, et al. [11]. Compressed air, flows through a rotary seal, up an aluminum hollow shaft, and through a Teflon pipe to establish a fully developed flow before entering the heat transfer model [10]. When subjected to rotation, air flows radially outward in the first pass of the heat transfer model and radially inward in the second pass. Air exhausts into the atmosphere through an opening at the end of the second unheated pass.

Figure 3.2 on page 21 shows a schematic of the two-pass square channel without ribs attached. The hydraulic diameter (D_h) of the square test section is 12.7 mm. "The heated test section length-to-hydraulic diameter ratio is 24. Each pass is 12 hydraulic diameters long connected by a sharp 180° turn" [10]. The channel walls are composed of copper plates separated by Teflon strips. The copper plates are heated with electric resistance heaters which provide a uniform heat flux [10]. Figure 3.2 on page 21 also indicates the model rotating about a centerline with flow moving radially outward in the first-pass and radially inward in the second-pass. The mean radius-to-hydraulic diameter ($\bar{R}/D_h$) is 30 [11].

Heated Channel Description

Figure 3.3 on page 22 shows the rib arrangement, channel orientation, and secondary flows generated by rotation and rib placement. The parallel ribs are attached to the leading

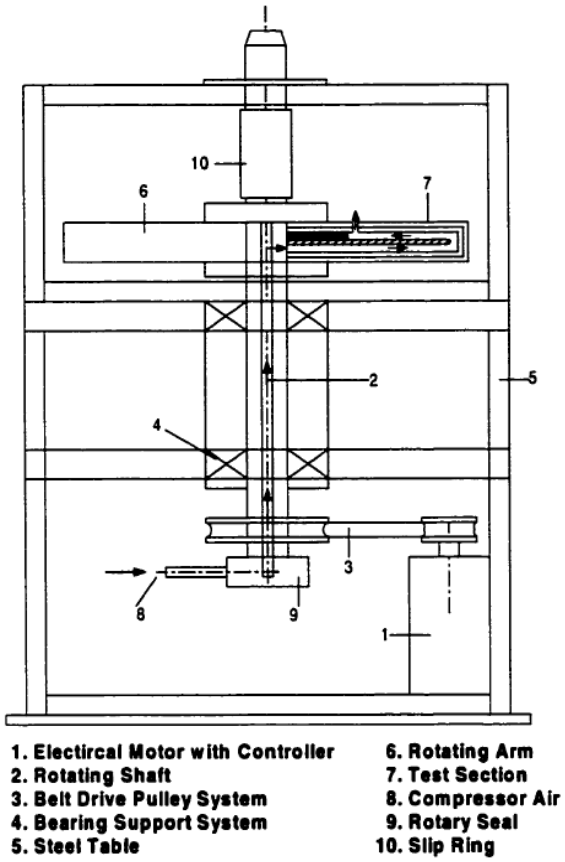

Figure 3.1 Schematic of the experimental apparatus [10]

and trailing surfaces at +45°. The rib height-to-hydraulic diameter radio (e/D_h) is 0.125 and the rib pitch-to-height ratio (P/e) is 10.

Figure 3.3 also shows a top view of the model with the direction of rotation indicated by an arrow pointing from the trailing surfaces toward the leading surfaces. The normal orientation of $\beta = 90°$ represents a typical configuration for a multipass channel located in the middle of a turbine blade. The angled orientation of $\beta = 135°$ represents a configuration found more toward the rear of turbine blades where the blade surfaces are angled with respect to the direction of rotation.

The conceptual view of secondary flows induced by ribs are indicated by solid lines. The secondary flows generated by rotational forces are indicated by the dashed lines. "The

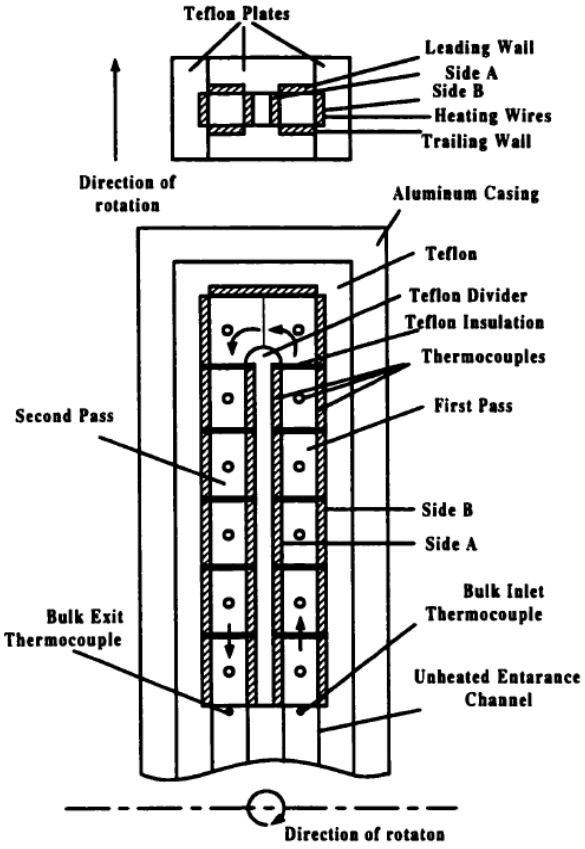

Figure 3.2 Schematic of the two-pass channel [10]

conceptual view shows that the secondary flow by rotation is mostly on the bulk flow region, whereas the rib effect is expected to be nearer the rib mounted-surfaces" [10]. The channel rotates at a constant 550 rpm. Therefore, both rotation number ($Ro = \Omega D_h/u_\infty$) and Reynolds number ($Re = \rho u_\infty D_h/\mu$) are set primarily by the inlet flow velocity.

Data Reduction

The convective heat transfer flux for coolant flow over a flat plate is expressed as

$$q_s^{''} = h\,(T_s - T_\infty) \tag{3.1}$$

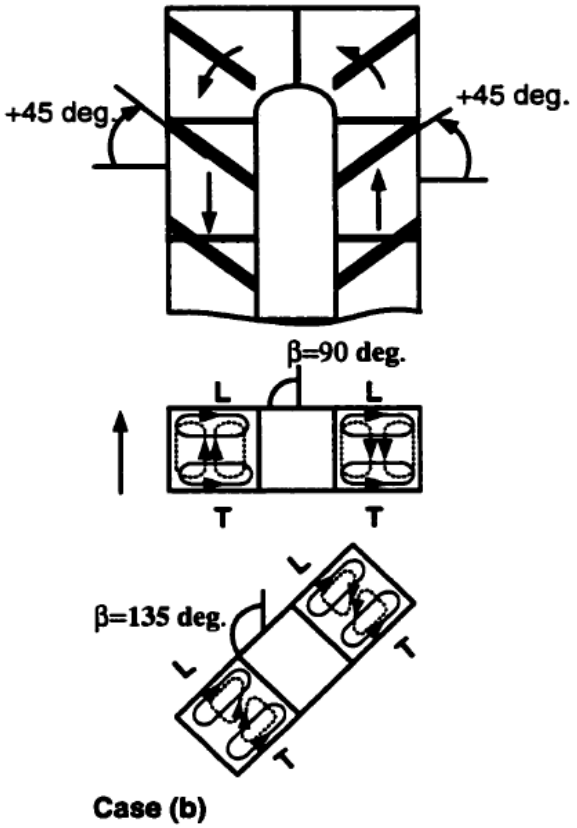

Figure 3.3 Conceptual view of secondary flow vortices (dash line: rotation-induced vortices, solid line: rib-induced vortices)[10]

where h is the convective heat transfer coefficient, T_s is the surface temperature, and T_∞ is the bulk flow temperature beyond the thermal boundary layer. At the surface, the heat transferred to the fluid is matched by the heat transferred from the wall by the conduction equation

$$q_s^{''} = -k_f \left(\frac{\partial T}{\partial y} \right) \Bigg|_{y=0} \tag{3.2}$$

where k_f is the conduction coefficient of the fluid. Substituting the definition of $q_s^{''}$ from Equation 3.2 into Equation 3.1 we can rearrange to express the local convective heat transfer coefficient as

$$h = \frac{-k_f \left(\frac{\partial T}{\partial y}\right)\Big|_{y=0}}{(T_s - T_{bx})} \tag{3.3}$$

where T_{bx} represents the local bulk flow temperature at a given x location. The formal definition of Nusselt number for internal flow is expressed as

$$Nu = \frac{h \cdot D_h}{k_f} \tag{3.4}$$

where D_h is the hydraulic diameter $(4 \cdot A_c/P_w)$; a ratio of cross-sectional area, A_c, to wetted perimeter length, P_w. Substituting for h, we obtain a definition for the local Nusselt number given by:

$$Nu = \frac{\left(\frac{\partial T}{\partial y}\right)\Big|_{y=0} D_h}{T_s - T_{bx}} \tag{3.5}$$

To reduce the influence of Reynolds number when comparing heat transfer coefficients, the local Nusselt numbers are normalized by the Nusselt number for fully developed turbulent flow in smooth circular tubes with no rotation correlated by Dittus-Boelter [36] as:

$$Nu_s = 0.023 \cdot Re^{0.8} \cdot Pr^{0.4} \tag{3.6}$$

The Prandtl number for air is $Pr = 0.72$. Air properties are based on the mean bulk air temperature. To match the experimental methods, the local bulk mean temperature used in Equation 3.5 is found by linear interpolation between the measured inlet and outlet bulk temperatures. The experimental results of Al-Hadhrami [10], used for numerical comparison, have error bars obtained by applying the method described by Kline and McClintock [37]. Inspection of the governing heat transfer equations indicate that the uncertainty of the measured Nusselt number ratio increases for low wall-to-coolant temperature difference $(T_w - T_{bx})$ and for low net heat input. Al-Hadhrami describes the error in measured heat transfer

by noting "the typical uncertainty in the Nusselt number is estimated to be less than 8% for Reynolds number larger than 10,000. However, the maximum uncertainty could be up to 20% for lower heat transfer coefficients for the lowest Reynolds number tested" [10].

Computational Domain

The two-pass square channel was discretized using a computational mesh with 9,438,801 nodes. This mesh includes 8,104,160 tetrahedral volume elements, 238,058 pyramids, and 15,635,378 Prism cells extruded off of boundary walls. The smooth walled rectangular channel, case (a), was meshed with 15,996,246 nodes. Cases (c) and (d), with V-shaped ribs attached to leading and trailing surfaces, have volume meshes with 13,997,462 and 13,621,331 nodes respectively. Figure 3.4 shows the volume mesh for the two-pass square channel at a cross-section located at the inlet to the heated test section. Prism layers can be seen extruded off all walls. These small cells are blended into larger tetrahedral elements in the core flow region at the center of the channel.

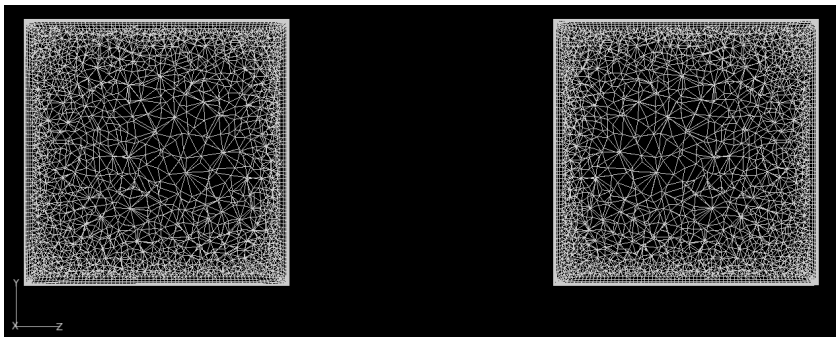

Figure 3.4 Square channel volume mesh

Figure 3.5 shows the surface mesh on the leading surface boundaries. The nodes are generally distributed evenly with local packing on rib corners. The turn region surfaces have slightly less dense surface meshes, but retain the same number of prism layers off the wall and the same volume mesh density.

Figure 3.5 Square channel volume mesh

Figure 3.6 shows a zoomed in view of one 45° angled rib in the first pass channel. Again, the nodes are evenly distributed on flat surfaces but have local packing in rib corners and faces where velocity and temperature gradients may be higher.

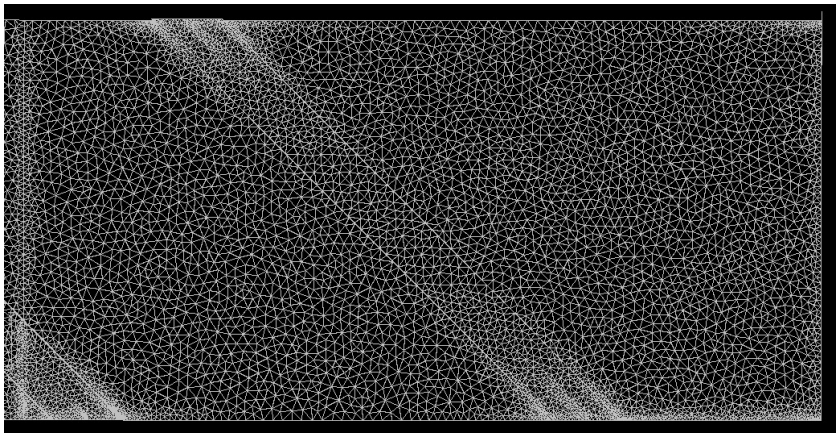

Figure 3.6 Square channel volume mesh

Figure 3.7 shows a cross-sectional cutting plane along the centerline of the first pass channel. The prism layer extrusion is maintained over the flat surfaces as well as the ribs. Prisms in this viscous region are blended using pyramids at the interface to to tetrahedral elements.

Boundary Conditions

The inlet and oulets of the computational domain were located 10 hydraulic diameters away from the test section entrance and exit. The walled boundaries in this region were

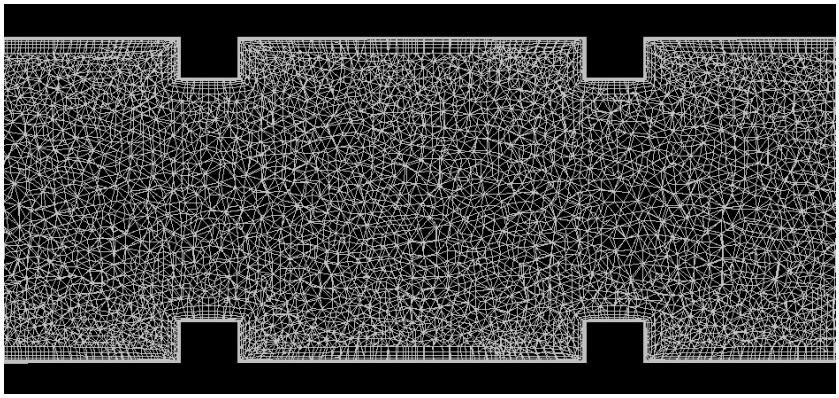

Figure 3.7 Square channel volume mesh

viscous but adiabatic. This allowed the flow field to become fully developed before entering the test section. The inlet boundary condition was a constant velocity for each run. The inlet velocity varied between runs to match the experimental Reynolds number. The inlet temperature was set to a constant 300 K. The outlet boundary condition used a pressure specification using an atmospheric backpressure of 101,325 Pa. The viscous walls of the test section were set to an isothermal temperature of 338 K. For the cases involving channel rotation, the whole channel was rotated about the $-Z$ axis with an average non-dimensional radius $\overline{R}/D_h = 30$. The rotational speed was a constant 550 rotations per minute.

CHAPTER 4

SQUARE CHANNEL RESULTS, AR = 1

Test Case Summary

Table 4.1 summarizes the cases run for the square test channel. Inflow velocities were set to 6.18, 12.36, and 30.90 m/s to match experimental Reynolds numbers of 5,000, 10,000, and 25,000 respectively. For each Reynolds number, the channel was tested under stationary conditions, orthogonal rotation ($\beta = 90°$), and angled rotation ($\beta = 180°$). The rotation number necessarily decreases from 0.118 at $Re = 5,000$, down to 0.024 for $Re = 25,000$. For low coolant flows of $Re = 5,000$, the average temperature of the fluid is 328 K at the exit of the heated channel. For higher flow rates, at $Re = 25,000$, the average temperature of the fluid is only 322 K by the time it reaches the channel exit. The Dittus-Boelter [36] relation includes the proportionality $Nu_s \propto Re^{0.8}$. Therefore, the baseline Nusselt numbers, Nu_s, are 18.36, 31.96, and 66.53 for Reynolds numbers of 5,000, 10,000, and 25,000 respectively. Using the Schlichting [38] approximation formula to determine the local skin friction coefficient, the non-dimensional wall distance from wall to first off-wall grid point, y^+, was computed for the square and rectangular channels. For the square channel with Reynolds numbers ranging from 5,000 to 25,000, values of y^+ ranged from 3.10×10^{-3} to 1.25×10^{-2}. Finally, Table 4.1 indicates N_{iters}, the number of time steps that each case ran. Psuedo-time-step iterative time marching was achieved by using volume-dependent local time stepping for each grid node. Most cases reached a steady state before 5,000 iterations as evidenced by both residual and mass balance convergence. However, some cases were set to run significantly longer in order to verify convergence and solution stability. The results near 20,000 iterations were not significantly different than those obtained near 10,000 iterations.

Table 4.1 Square channel case summary

Re	**Orientation**	**Ro**	$\mathbf{V_i}$ (m/s)	$\mathbf{T_{exit}}$ (K)	$\mathbf{Nu_s}$	$\mathbf{N_{iters}}$
5,000	stationary	0.000	6.18	328.8	18.36	20,000
5,000	$\beta = 90°$	0.118	6.18	328.0	18.36	18,000
5,000	$\beta = 135°$	0.118	6.18	328.3	18.36	7,200
10,000	stationary	0.000	12.36	326.2	31.96	7,000
10,000	$\beta = 90°$	0.059	12.36	325.6	31.96	18,400
10,000	$\beta = 135°$	0.059	12.36	325.3	31.96	7,200
25,000	stationary	0.000	30.90	322.8	66.53	10,000
25,000	$\beta = 90°$	0.024	30.90	321.7	66.53	10,000
25,000	$\beta = 135°$	0.024	30.90	321.5	66.53	12,000

Reynolds Number of 5,000

No Rotation

Figure 4.1 shows the regionally averaged Nusselt number ratios (Nu/Nu_s) from leading and trailing surfaces for a Reynolds number of 5,000. The Nusselt numbers were obtained via a surface integral average applied to 12 surface sections on both the leading and trailing surfaces. the experimental heating plate. The regionally averaged Nusselt numbers were obtained using Outside the turn region, the non-rotating Nusselt numbers are two to three times that of the Nusselt number for fully developed turbulent flow in smooth circular tubes with no rotation, Nu_s, specified in Equation 3.6 on page 23. With no rotation, the leading and trailing surfaces have nearly identical Nusselt number ratios. Overall, the numerical Nusselt number ratios follow the trends of the experiment while remaining consistently lower across the heated flow passage. The peak Nusselt number ratio occurs around the middle of the first pass ($X/D_h = 6$); due to the counter rotating cells and increased turbulence caused by the +45° parallel ribs. The Nusselt number ratios decrease as the fluid approaches the 180° turn ($X/D_h = 9$). In the second pass, The Nusselt number ratio increases then decreases moderately and increases again toward the end of the heated test section.

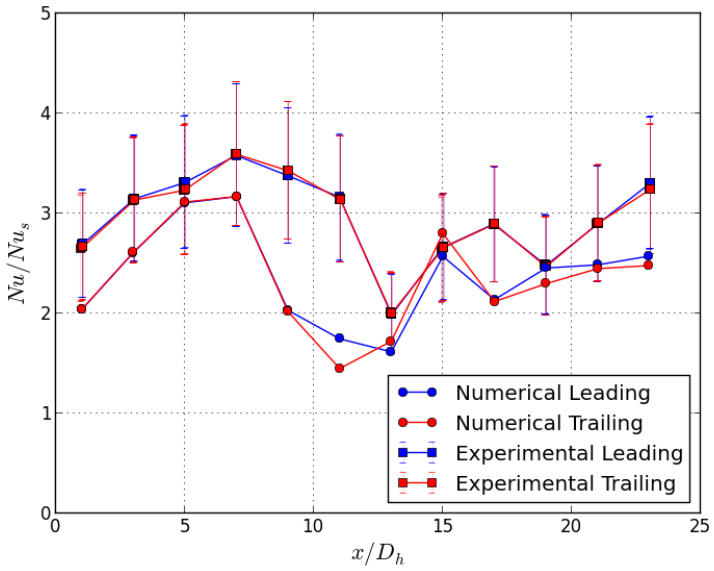

Figure 4.1 Square channel with Re = 5,000 and no rotation; Ro = 0.0

Orthogonal Rotation

Figure 4.2 on the next page shows the effect that rotation has on Nusselt number ratios for the heated turbulator with $\beta = 90°$ and Re = 5,000. This case represents the highest tested rotation number at $Ro = 0.118$. This means that there are significant rotational effects coupled with relatively low fluid mass inflow. It is evident that rotation significantly increases Nusselt number ratios on the first pass trailing and second pass leading surfaces. Conversely, Nusselt number ratios for the first pass leading and second pass trailing surfaces are lower. Wagner, et al. [7, 8], in their study on the effects of rotation on the local heat transfer of multi-pass channels, concluded that the first pass of the coolant passage with rotation created a thinner boundary layer on the trailing surface and a thicker boundary layer on the leading surface resulting in increased heat transfer and decreased heat transfer, respectively. The second pass had opposite characteristics with the reversal of the Coriolis force direction. We see that the second pass leading surface Nusselt number ratio increases to about 3.5 after the 180° turn, then decreases slightly as the developing boundary layer suppresses heat

transfer, and finally increases as the secondary flows begin to increase turbulent mixing and heat transfer in the channel.

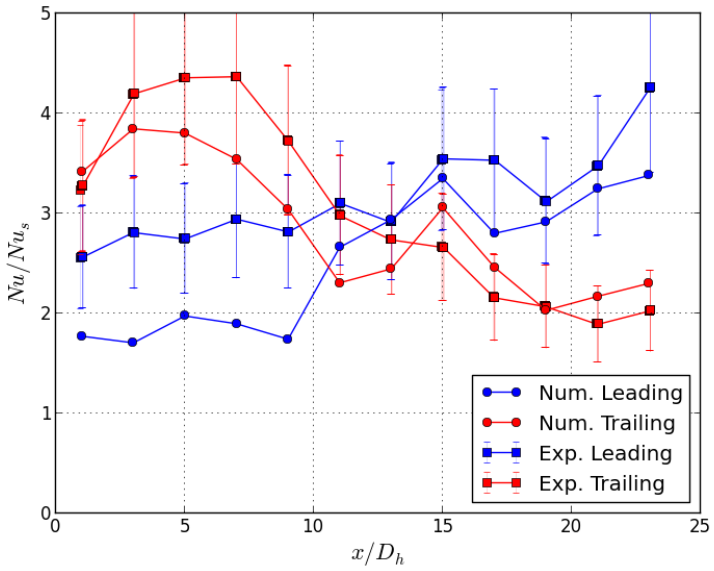

Figure 4.2 Square channel with Re = 5,000 and $\beta = 90°$; Ro = 0.118

Angled Rotation

We see in Figure 4.3 on the following page that the 135° channel orientation also shows enhanced heat transfer caused by rotation. Specifically, the first pass trailing surfaces and the second pass leading surfaces show higher Nusselt number ratios compared to the no rotation case, while the first pass leading and second pass trailing surfaces are lower. However, the difference between leading and trailing Nusselt number ratios in each pass is much less than what is seen for $\beta = 90°$. "The effect of Coriolis forces on the first pass trailing and second pass leading surfaces for the 90° rotation is greater since the two counter vortices are normally incident on the first pass trailing surface and second pass leading surface" [10]. Thus, the angled rotation spawns secondary flow vortices which typically impinge on the ribbed surfaces at a non-orthogonal angle. This angled rotation case is subjected to the highest

tested rotation number of $Ro = 0.118$. Such high relative rotation generally produces the largest difference between leading and trailing surface Nusselt number ratios.

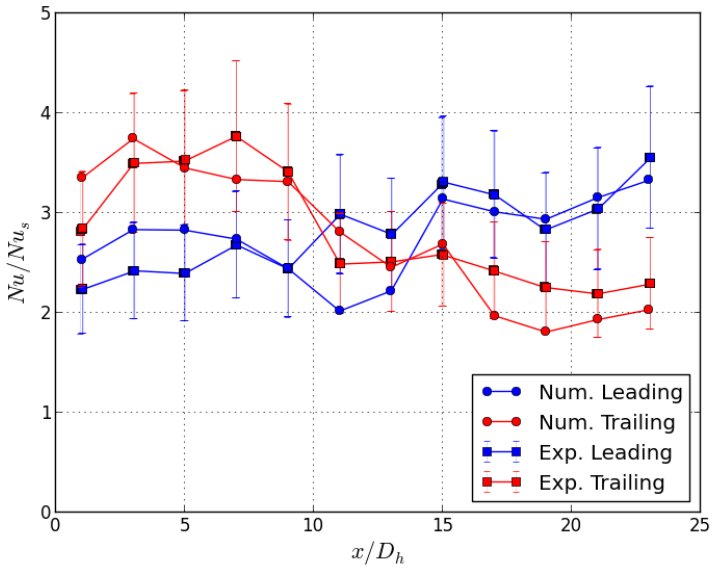

Figure 4.3 Square channel with Re = 5,000 and $\beta = 135°$; Ro = 0.118

Reynolds Number of 10,000

No Rotation

The local surface temperature gradient distributions on the leading surfaces are shown in Figure 4.4 on the next page for $Re = 10,000$ and no rotation. We see that the temperature gradients are highest in the first-pass channel leading surface where the bulk flow temperature is near $300°K$ while the surface is a constant $338°K$. The bulk flow temperature increases as it moves from the first pass, around the 180° bend, and through the second pass.

Figure 4.5 on the following page shows the pressure distribution on the leading surfaces of the channel. The grid is viewed from a positive y perspective with flow entering the heated section of the channel with high pressure and traveling right to left in the first pass. The

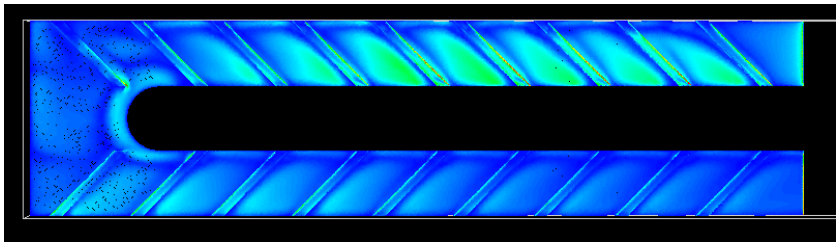

Figure 4.4 Square channel Nusselt number distribution, Re = 10,000, no rotation

pressure drops from a maximum, shown in red, of 102.167 kPa, down to a minimum, shown in blue, of 101.177 kPa.

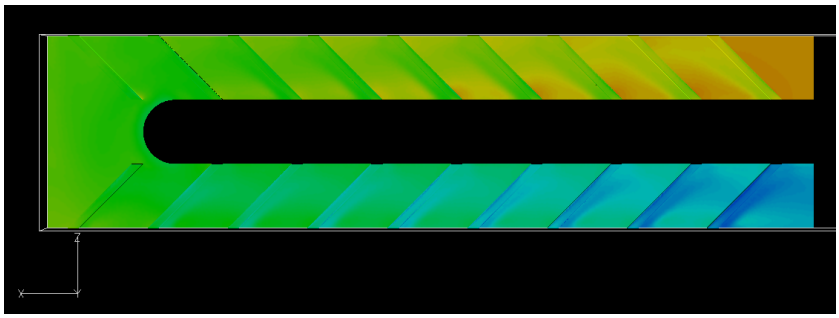

Figure 4.5 Pressure distribution on leading surfaces of square channel

Figure 4.6 on the next page shows an isometric view of the pressure distribuition in the non-rotating channel. This view gives a better perspective on the channel layout as well as rib location. We see that the pressure decreases over the top surface of each rib, as indicated by the local color spectrum change from red toward blue. The 45° ribs force the near-wall fluid to flow toward the outer wall in the first pass and toward the inner wall in the second pass.

Figure 4.7 on the following page shows the temperature distribution of the fluid along a cross-section located at $x/D_h = 10$, just before the 180° turn. The temperature varies from a high of $338°K$ shown in red at the wall, to a local minimum of $310.8°K$ in the bulk flow region. The second pass cross-section shows a general increase in bulk flow temperature when compared with the first pass cross-section. It can be seen that the flow travels up the outer

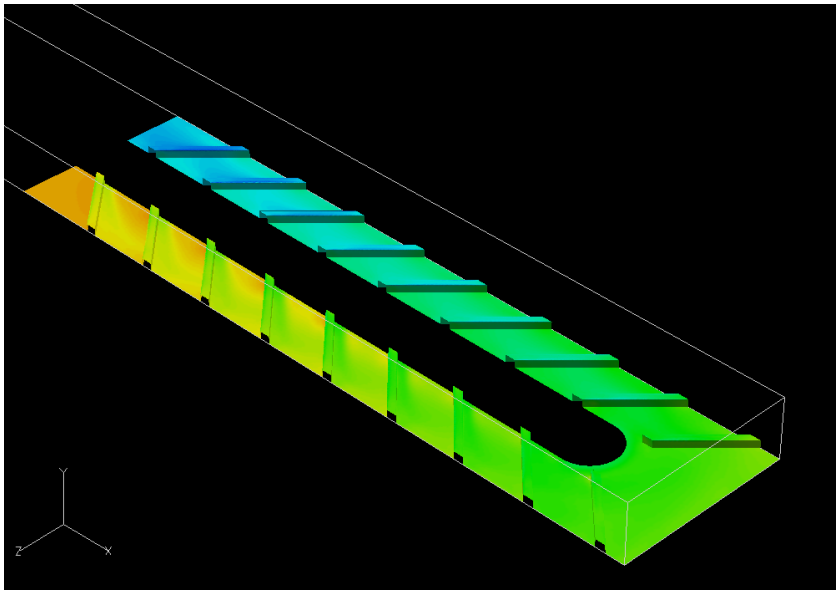

Figure 4.6 Pressure distribution, isometric view

wall and back into the main-stream flow along the mid-point of the channel. This swirling aids in the turbulent mixing and increases heat transfer from the walls to the coolant flow.

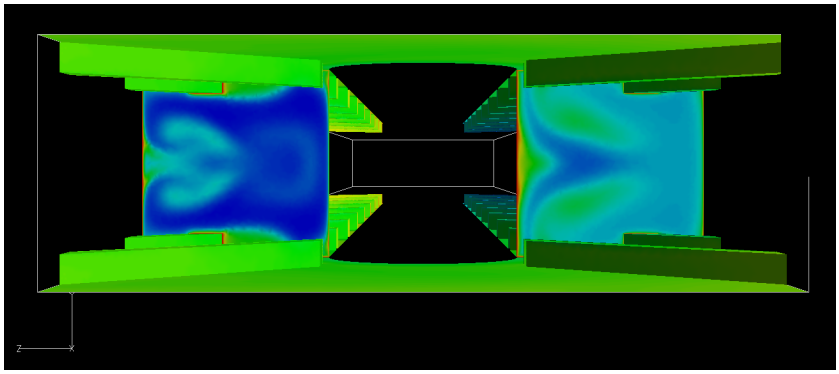

Figure 4.7 Temperature Distribution at $x/D_h = 10$

Figure 4.8 on the next page shows a top view of the channel with a cross-section placed midway down the channel at $x/D_h = 5$. The local temperature is visualized with the color spectrum changing from a high of $338°K$ at the wall, held constant by heaters, to a local minimum of $300°K$; the temperature of inlet flow, shown in blue. The first pass cross-section shows higher temperatures behind the ribs and along the middle of the outer wall.

This highlights the effect that the ribs have on forcing the flow toward the outer wall and then back into the bulk flow region. The second pass cross-section shows that there has been sufficient heat transfer to warm the bulk flow to a near uniform temperature.

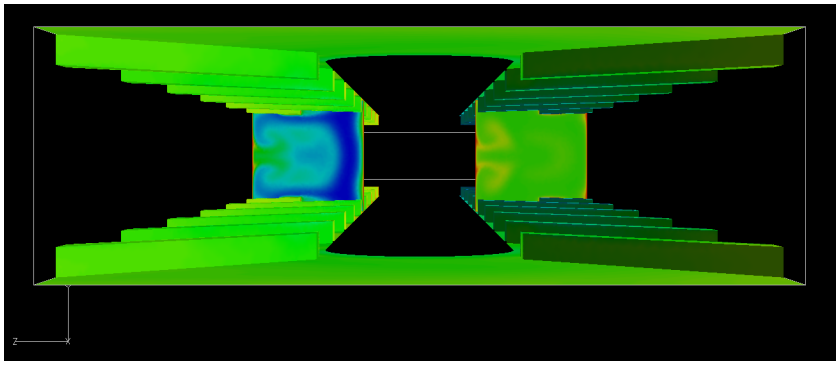

Figure 4.8 Temperature Distribution at $x/D_h = 5$

Figure 4.9 on the following page shows the results of Nusselt number ratios for $Re = 10,000$ and no rotation. Due to channel symmetry and no rotation, the leading and trailing surfaces have nearly identical Nusselt number ratios. With the exception of the region approaching the 180° turn ($X/D_h = 9$ and 11), the numerical Nusselt number ratios are nearly identical to the experimental values. The peak Nusselt number ratio occurs around the middle of the first pass ($X/D_h = 6$); due to the counter rotating cells and increased turbulence caused by the +45° parallel ribs. The Nusselt numbers are mostly between two and three times that of the baseline smooth tube Nusselt number, Nu_s.

Orthogonal Rotation

Figure 4.10 on the next page shows the effect that rotation has on Nusselt number ratios for the turbulator with $\beta = 90°$ and $Re = 10,000$. It is evident that the moderate rotation, $Ro = 0.059$, increases Nusselt number ratios on the first pass trailing and second pass leading surfaces. Alternatively, Nusselt number ratios for the first pass leading and

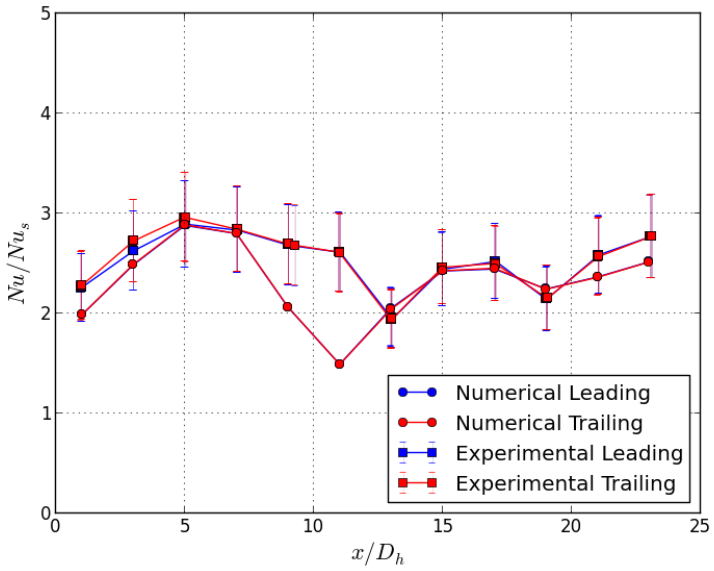

Figure 4.9 Square channel with Re = 10,000 and no rotation; Ro = 0.0

second pass trailing surfaces are lower. The numerical results again match the trend of the experimental results and fall mostly within the experimental uncertainty regions.

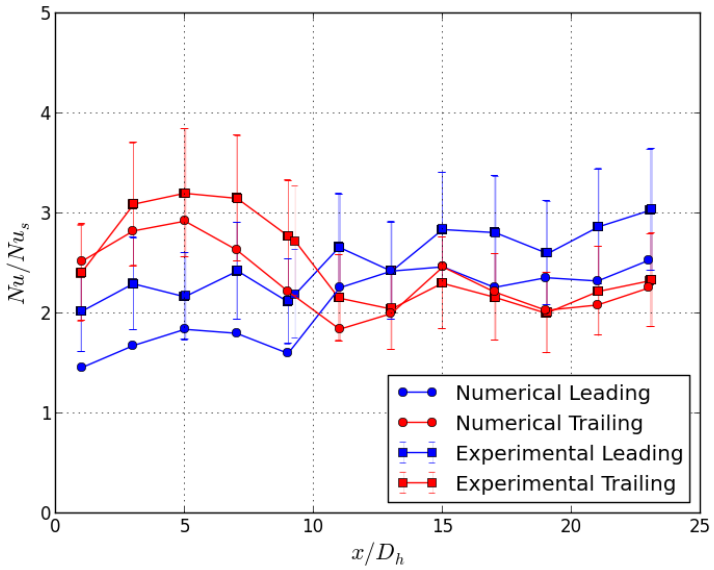

Figure 4.10 Square channel with Re = 10,000 and $\beta = 90°$; Ro = 0.059

Angled Rotation

Figure 4.11 compares numerical and experimental Nusselt number ratios subjected to $\beta = 135°$ angled channel orientation and $Re = 10,000$. The first pass trailing surfaces and second pass leading surfaces show moderately higher Nusselt number ratios than the first pass leading and second pass trailing surfaces, respectively. Given the moderate rotation rate, $Ro = 0.059$, and angled rotation of $\beta = 135°$, the differences between leading and trailing Nusselt number ratios are significantly reduced.

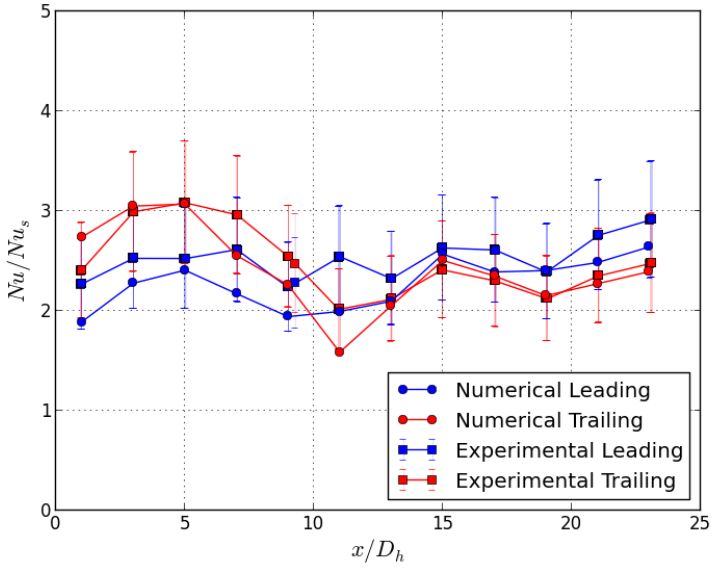

Figure 4.11 Square channel with Re = 10,000 and $\beta = 135°$; Ro = 0.059

Reynolds Number of 25,000

No Rotation

The numerical results for local Nusselt number ratios are compared to the experimental values in Figure 4.12 on the next page. The non-rotating Nusselt numbers are 2-3 times that

of the Nusselt number for fully developed turbulent flow in smooth circular tubes with no rotation correlated by Dittus-Boelter [36].

With no rotation, it is no surprise that, as dictated by the model symmetry, the leading and trailing surfaces have nearly identical Nusselt number ratios. Overall, the numerical Nusselt number ratios follow the trends of the experiment while remaining consistently lower across the heated flow passage. The peak Nusselt number ratio occurs around the middle of the first pass ($X/D_h = 6$); due to the counter rotating cells and increased turbulence caused by the $+45°$ parallel ribs. The Nusselt number ratios decrease as the fluid approaches the $180°$ turn ($X/D_h = 11$). In the second pass, The Nusselt number ratio increases then decreases moderately and increases again toward the end of the heated test section.

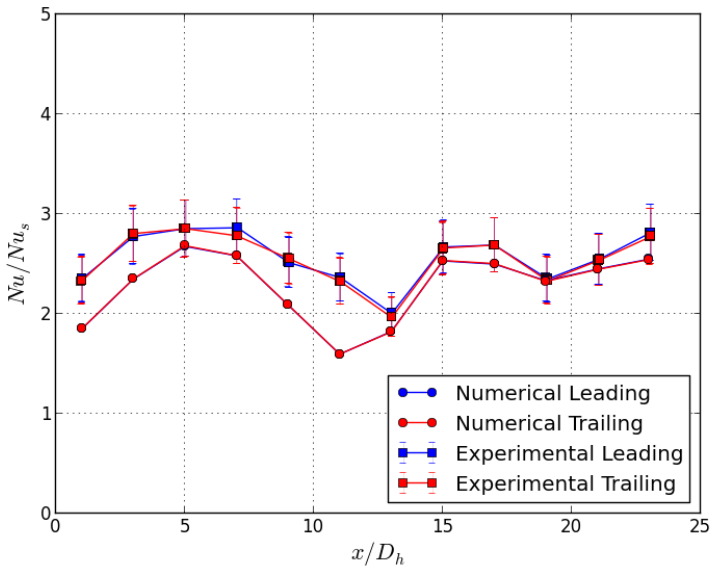

Figure 4.12 Square channel with Re = 25,000 and no rotation; Ro = 0.0

Orthogonal Rotation

Figure 4.13 on the following page shows the effect that rotation has on Nusselt number ratios for the turbulator with $\beta = 90°$. It is evident that rotation increases Nusselt number

ratios on the first pass trailing and second pass leading surfaces. However, Nusselt number ratios for the first pass leading and second pass trailing surfaces are lower. The numerical results again match the trend of the experimental results while remaining slightly lower.

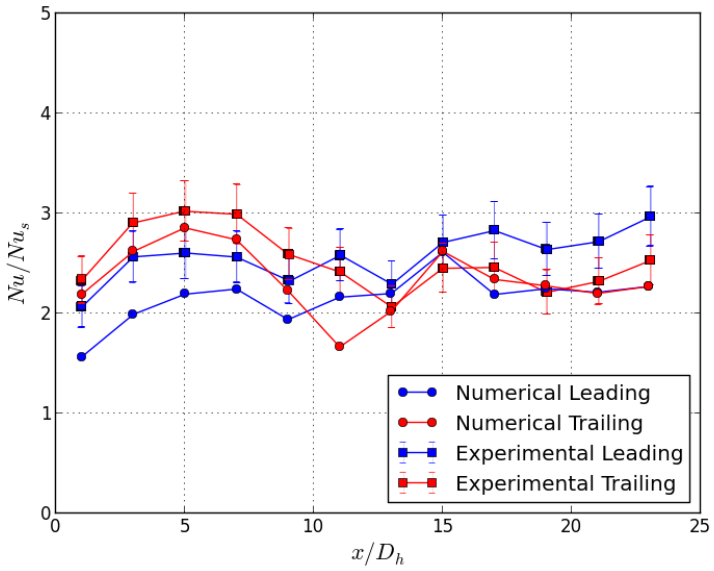

Figure 4.13 Square channel with Re = 25,000 and $\beta = 90°$; Ro = 0.024

Angled Rotation

Figure 4.14 on the next page shows that the 135° channel orientation also exhibits enhanced heat transfer caused by rotation. Specifically, the first pass trailing surfaces and the second pass leading surfaces show higher Nusselt number ratios, while the first pass leading and second pass trailing surfaces are lower. However, the difference between leading and trailing Nusselt number ratios in each pass is much less than what is seen for $\beta = 90°$. The reason for this is similar to that for angled rotation at lower Reynolds numbers such as those seen in section 4.

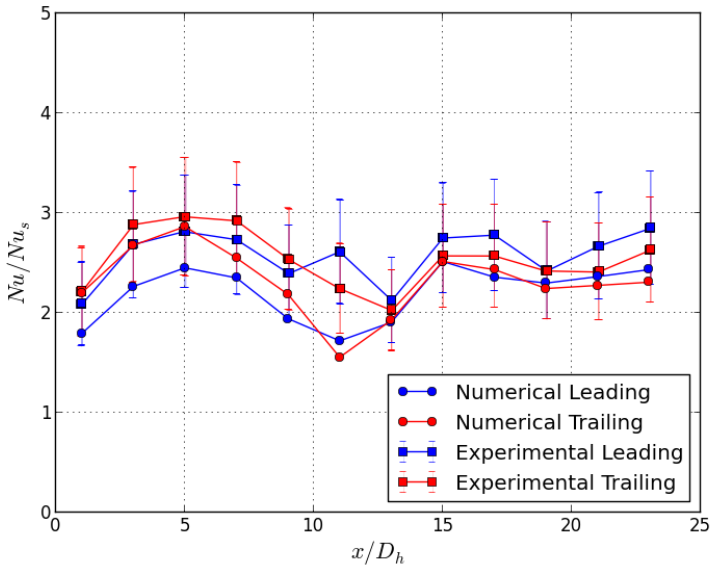

Figure 4.14 Square channel with Re = 25000 and $\beta = 135°$; Ro = 0.024

CHAPTER 5

RECTANGULAR CHANNEL RESULTS, AR = 2

Channel Description

This chapter shows the heat transfer results for the two-pass rectangular channel with smooth and rib-roughened surfaces. Figure 5.1 compares the rib types used. The 45° angled ribs are mirrored about the channel centerline to create two orientantions of 45° V-shaped ribs. The first orientation is called the 45° V-shaped rib while the second is called the inverted 45° V-shaped rib [39]. The conceptual views for rib-induced secondary flow vortices can also be seen in Figure 5.1. "It is conjectured that the 45° V-shaped rib creates two counter rotating vortices. as the fluid approaching the V-shaped rib, it splits into two streams" [39]. Each stream then moves along the rib toward the outer walls and then returns back to the centerline making a counter rotating vortex. Near surface fluid approaching the inverted 45° V-shaped rib starts converging from the outer walls toward the channel centerline. This creates a stagnation region as the fluid slows before traveling over the rib and creating two counter rotating vortices. The lack of a stagnation region leads to the expectation that the 45° V-shaped rib will perform better than the inverted ribs in non-rotating conditions.

Figure 5.2 shows a conceptual view of the two-pass rectangular channel without ribs for Case (a). The hydraulic diameter (D_h) of the rectangular test section is $16.9\overline{33}$ mm. The length of each channel is the same as that of the square channel. Figure 5.2 also indicates the model rotating about a centerline with flow moving radially outward in the first-pass and radially inward in the second-pass. The top views of the channel can be seen for both orthogonal and angled rotation with the secondary flow vortices induced by rotation shown as dashed lines. With flow moving radially outward in the first pass, the effect of the Coriolis

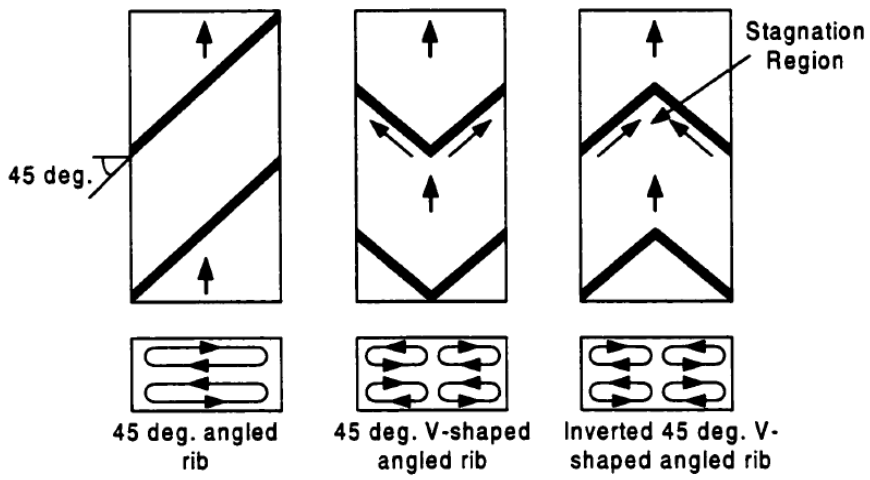

Figure 5.1 Conceptual view of rib-induced secondary flow vortices [39].

force pushes the bulk fluid flow toward the trailing surface creating increased heat transfer from the trailing surface and decreased heat transfer from the leading surface. Alternatively, the opposite case is true in the second pass where the fluid moves radially inward and the Coriolis force directs the bulk fluid flow toward the leading surface. This causes an increase of heat transfer from the leading surface and a decrease from the trailing surface for the second pass.

The experimental study uesd four different arrangements of the parallel 45° V-shaped ribs. Case (b) had V-shaped ribs in the first and second passes of the channel. Case (c) had inverted V-shaped ribs in the first pass and V-shaped ribs in the second pass. Case (d) had V-shaped ribs in the first pass and inverted V-shaped ribs in the second pass. Finally, case (e) had inverted V-shaped ribs in the first and second passes of the channel. Because of the similarity between these configurations, cases (c) and (d) were chosen to examine V-shaped rib effects in the first and second pass. This selection offered the ability to examine the effects that V-shaped and inverted V-shaped ribs had in the first and second pass channels.

Figure 5.3 shows the parallel arrangement of 45° V-shaped ribs attached to the leading and trailing surfaces to create Case (c). Inverted 45° V-shaped rib are place in the first

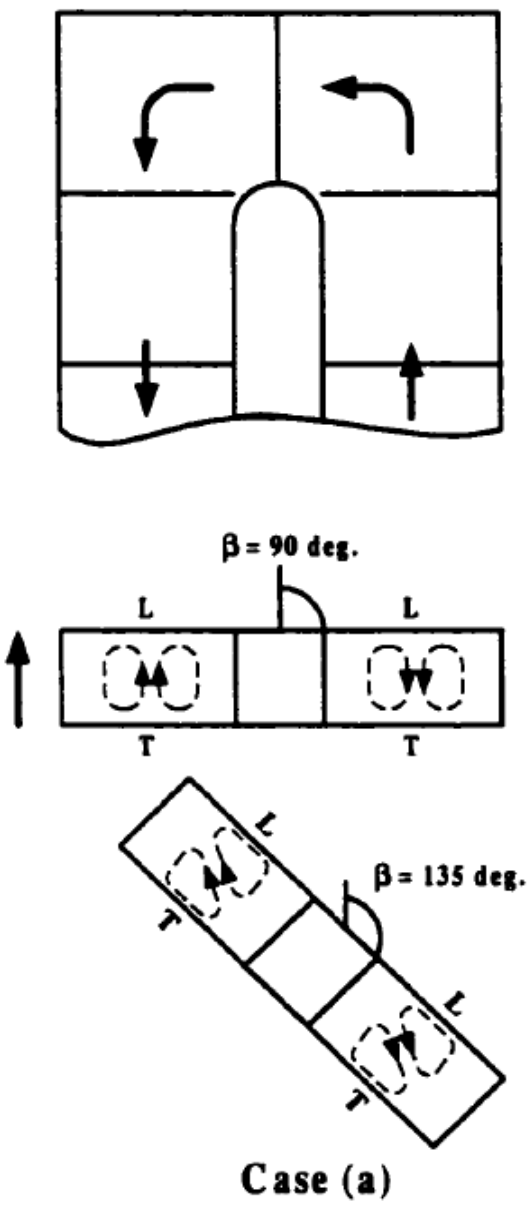

Figure 5.2 Conceptual view of rectangular channel Case (a), [39].

pass channel, while 45° V-shaped rib are place in the second pass channel. "As the channel angle changed to $\beta = 135°$, the rib induced secondary flow is unchanged, but the rotational secondary flows are shared between the principle surfaces (trailing, and leading) and side surfaces" [39]. Figure 5.4 shows the conceptual view for Case (d), which has 45° V-shaped

ribs in the first pass and inverted 45° V-shaped ribs in the second pass. The V-shaped ribs in the first pass cause the near wall fluid to flow from the channel center toward the outer walls before going over the ribs. Alternatively, the inverted V-shaped ribs cause the the near wall fluid to flow from the channel side walls toward the center before passing over the ribs.

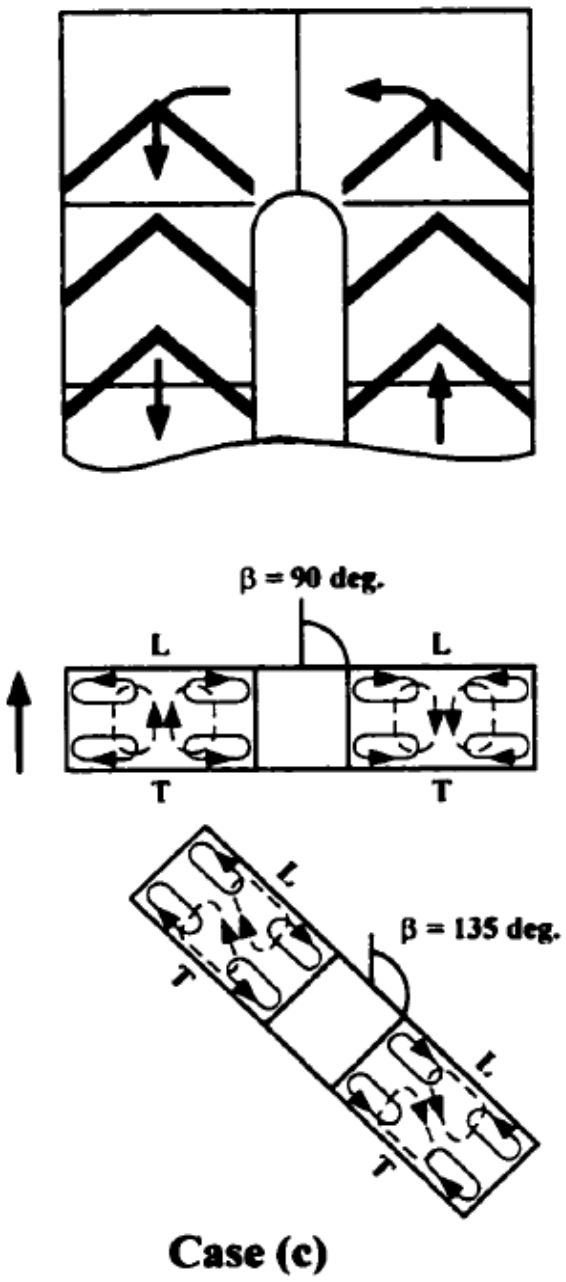

Figure 5.3 Conceptual view of rectangular channel Case (c), [39].

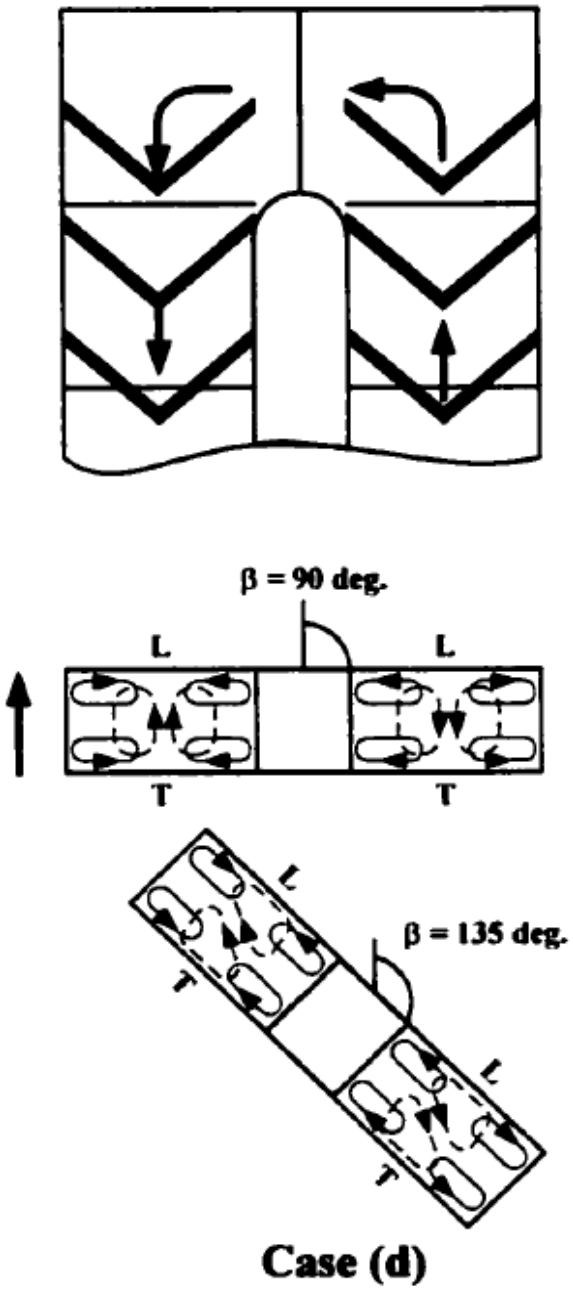

Figure 5.4 Conceptual view of rectangular channel Case (d), [39].

The following sections focus on the analysis of rectangular channel sections with various configurations of parallel V-shaped ribs.

Test Case Summary

Table 5.1 summarizes the cases run for the rectangular test channel. Inflow velocities were set to 4.63, 9.27, 23.17, and 37.08 m/s to match experimental Reynolds numbers of 5,000, 10,000, 25,000, and 40,000 respectively. For each Reynolds number, the channel was tested under stationary conditions, orthogonal rotation ($\beta = 90°$), and angled rotation ($\beta = 135°$). The rotation number decreases from 0.210 at $Re = 5,000$, down to 0.026 for $Re = 40,000$. The inlet fluid temperature is set to a constant 300 K for all cases. For low coolant flows of $Re = 5,000$, the average temperature of the fluid is 318 K at the exit of the heated channel. For higher flow rates, at $Re = 40,000$, the average temperature of the fluid is only 313 K by the time it reaches the channel exit. The Dittus-Boelter [36] relation includes the proportionality $Nu_s \propto Re^{0.8}$. Therefore, the baseline Nusselt numbers, Nu_s, are 18.36, 31.96, 66.53, and 96.90 for Reynolds numbers of 5,000, 10,000, 25,000, and 40,000 respectively. Using the Schlichting [38] approximation formula to determine the local skin friction coefficient, the non-dimensional wall distance, y^+, was computed for the rectangular channel. With Reynolds numbers ranging from 5,000 to 40,000, values of y^+ ranged from 2.32×10^{-3} to 1.42×10^{-2} due to a larger hydraulic diameter and different prism layer mesh than the square channel cases.

Table 5.1 Rectangular channel case summary

Re	**Orientation**	**Ro**	$\mathbf{V_i}$ (m/s)	$\mathbf{T_{exit}}$ (K)	$\mathbf{Nu_s}$
5,000	stationary	0.000	4.6349	318.4	18.36
5,000	$\beta = 90°$	0.210	4.6349	319.7	18.36
5,000	$\beta = 135°$	0.210	4.6349	318.2	18.36
10,000	stationary	0.000	9.2698	317.5	31.96
10,000	$\beta = 90°$	0.105	9.2698	318.1	31.96
10,000	$\beta = 135°$	0.105	9.2698	316.1	31.96
25,000	stationary	0.000	23.1746	314.4	66.53
25,000	$\beta = 90°$	0.042	23.1746	315.4	66.53
25,000	$\beta = 135°$	0.042	23.1746	313.7	66.53
40,000	stationary	0.000	37.0793	313.7	96.90
40,000	$\beta = 90°$	0.026	37.0793	313.4	96.90
40,000	$\beta = 135°$	0.026	37.0793	312.5	96.90

Case (a) Results

Case (a) encompasses the set of all experiments applied to a rectangular channel, of aspect ratio (AR) equal to 2, with no ribs attached to the walls. The tests were conducted with the Reynolds number, Re, ranging from 5,000 to 40,000. Additionally, the rotation number, Ro, varied from 0.0 to 0.210.

Figure 5.5 shows the regionally averaged Nusselt number ratios (Nu/Nu_s) from leading and trailing surfaces within the Case (a) model for $Re = 5,000$. The Nusselt number ratios decrease as the thermal boundary layer builds in the first pass. The 180° turn induces turbulent mixing which causes the Nusselt number ratios to rise to a maximum in the turn region from $x/D_h \approx 9$ to 11. The thermal boundary layer again increases in the second pass channel after the turn; causing a decrease in local Nusselt number ratios. Rotation induces a pair of counter rotating vortices in the channel. These vortices cause the flow to impinge upon the trailing surfaces in the first pass and leaading surfaces in the second pass. This in turn causes enhanced Nusselt number ratios for the first pass trailing and second pass leading surfaces.

Figure 5.6 shows the regionally averaged Nusselt number ratios (Nu/Nu_s) from leading and trailing surfaces within the Case (a) model for a Reynolds number of 10,000. The Nusselt number ratios show similar dependence on spacial location as the $Re = 5,000$ cases. However, the differences between leading and trailing surfaces are reduced as the rotation number decrease by half from 0.210 to 0.105 for $Re = 5,000$ and $10,000$ respectively.

For the stationary cases with no rotation, the Nusselt number ratio tends to decrease monotonically in the first pass. This steady decrease in Nusselt number ratio is attributed to the developing thermal boundary layer. Evidence of this is seen in Figure 5.7 and 5.8, which plot the temperature distribution in the first pass of the non-rotating channel of Case (a). We see a thermal boundary layer gradually increasing on the top and bottom surfaces as the coolant flow travels from the inlet of the heated section on the left, to the

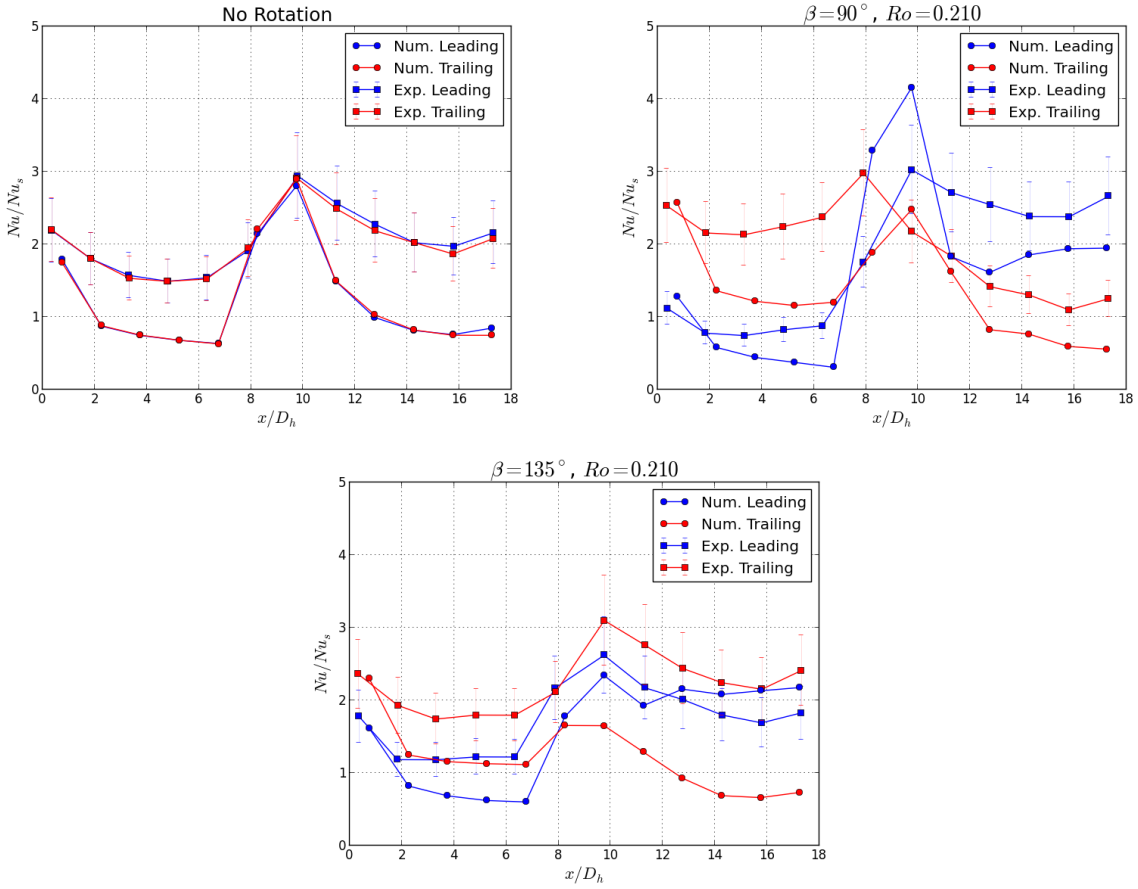

Figure 5.5 Nusselt number ratios for Case (a), Re = 5,000.

180° bend on the right. Heat is transferred from the walls with a maximum temperature set at 338 K, to the main stream flow having a local minimum temperature of 297 K.

The Nusselt number ratio increases in the turn region due to secondary flows induced by the 180° turn. The maximum Nusselt number ratio of nearly 3 is found within the 180° turn region at the entrance of the second pass. Figure 5.9 displays the temperature profile computed in the 180° turn region for Case (a) and Re=10,000. The velocity vectors are plotted at the center of the turn. The vector arrows are scaled by 1/4 for clarity, and are colored using a 16 degree color spectrum indicating the scalar temperature value held at each grid node. Two counter-rotating secondary flow vortices can be seen aiding in turbulent mixing and increasing local heat transfer in the turn region.

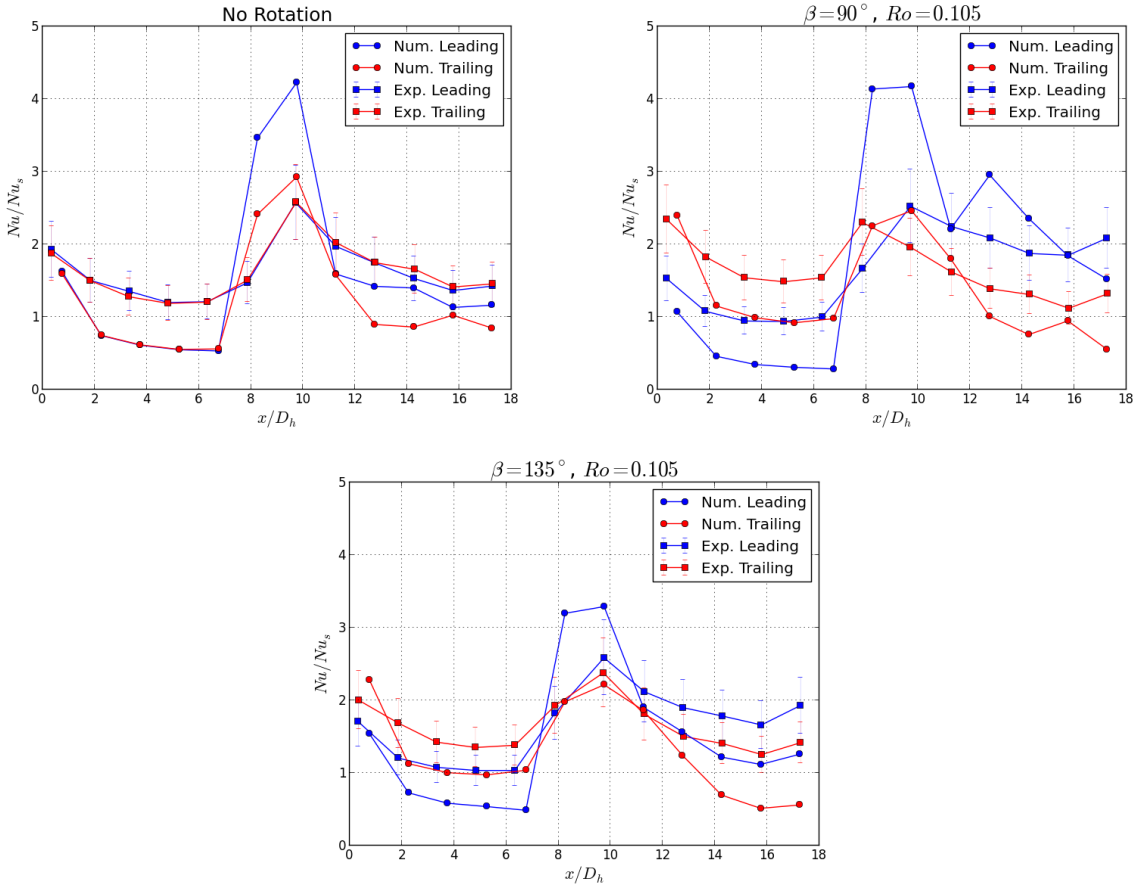

Figure 5.6 Nusselt number ratios for Case (a), Re = 10,000.

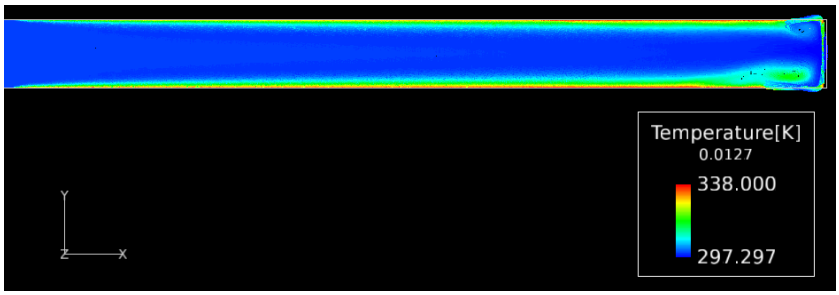

Figure 5.7 Thermal boundary layer development for Case (a), Re = 10,000.

The Nusselt number ratios again decrease in the second pass due to the dissipation of secondary flows induced by the 180° turn. Evidence of this can be seen in Figure 5.10, which shows the transition in flow behavior. The flow in the second pass channel transistions from being dominated by secondary flows toward a redevelopment of steady mainstream flow.

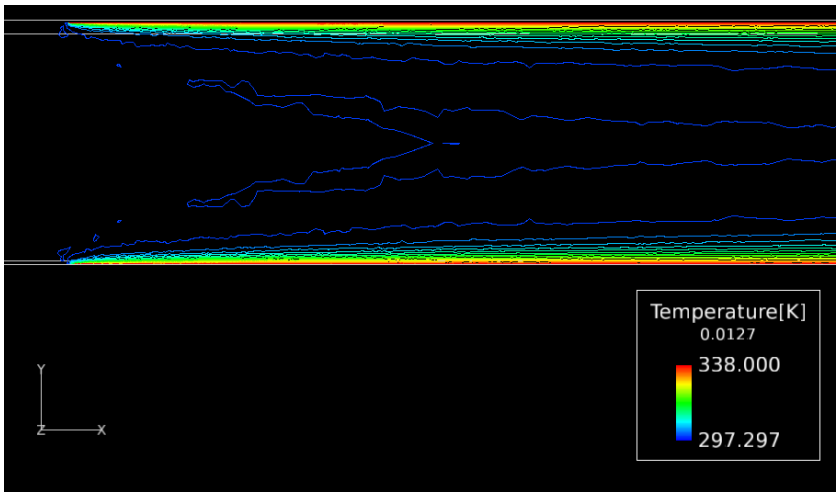

Figure 5.8 Temperature contours in first pass of Case (a), Re = 10,000.

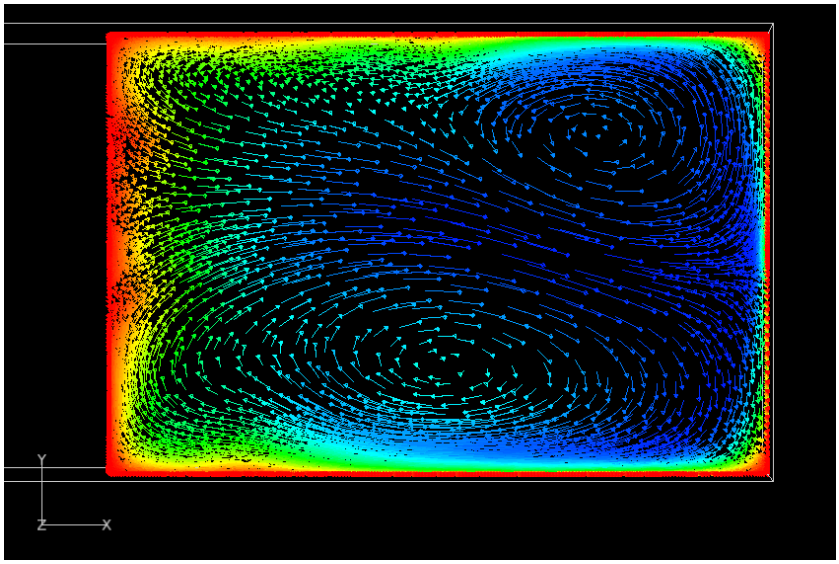

Figure 5.9 Temperature profile in 180° turn of Case (a), Re = 10,000.

The numerical results for Nusselt number ratio follow the general trends of the experiment, but are significantly lower in some zones outside the turn region. The smooth tube cases generally shows a higher dependance on boundary layer parameters than the ribbed channel cases. Thus, there tend to be larger discrepancies between experimental and numerical results when the near-wall flow phenomena are not sufficiently resolved.

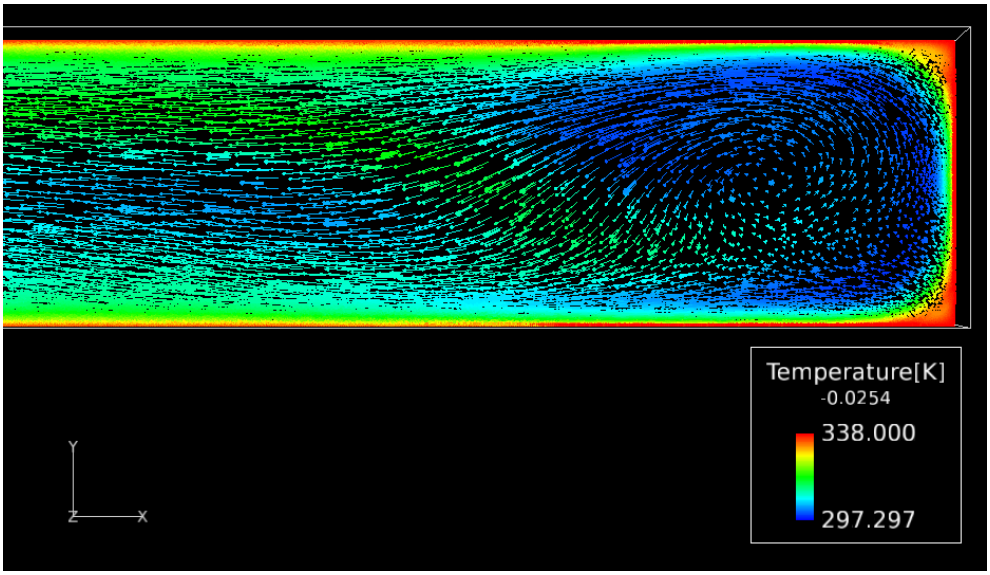

Figure 5.10 Temperature profile in second pass for Case (a), Re = 10,000.

Figure 5.11 shows the temperature contour distribution at $x/D_h = 5$ in the first pass channel subjected to Re=10,000 and orthogonal rotation, $\beta = 90°$, with $Ro = 0.105$. The temperature decreases from 338 K at the walls to a local minimum of 298.8 K in the mainstream flow region. It is also evident that the core coolant flow is forced closer to the trailing surface due to rotation and the secondary flow vorticies that are induced.

Figure 5.12 plots the contours of constant temperature at $x/D_h = 5$ in the second pass channel subjected to Re=10,000 and rotation with $\beta = 90°$. The lowest local temperature is 304.4 K in the core flow region. Secondary flow vortices impinge on the leading surface causing heat transfer to increase relative to the trailing surface in the second pass.

Figure 5.13 shows the temerature contour distribution at $x/D_h = 5$ in the first pass channel subjected to Re=10,000 and rotation with $\beta = 135°$. The temerature decreases from 338 K at the walls to a local minimum of 298.7 K. The core coolant flow is forced closer to the trailing surface due to rotation and the secondary flow vorticies that are induced.

Figure 5.14 plots the contours of constant temperature at $x/D_h = 5$ in the second pass channel subjected to Re=10,000 and rotation with $\beta = 135°$. The lowest local temperature

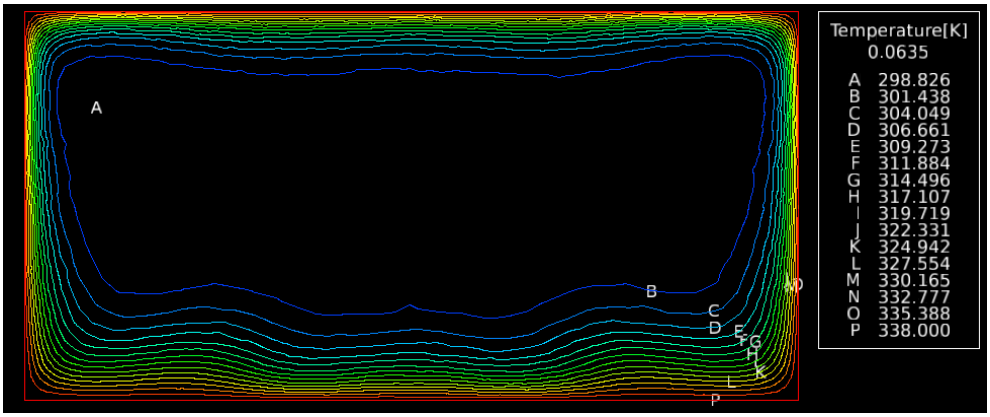

Figure 5.11 Temperature contours in first pass of Case (a), Re = 10,000, $\beta = 90°$.

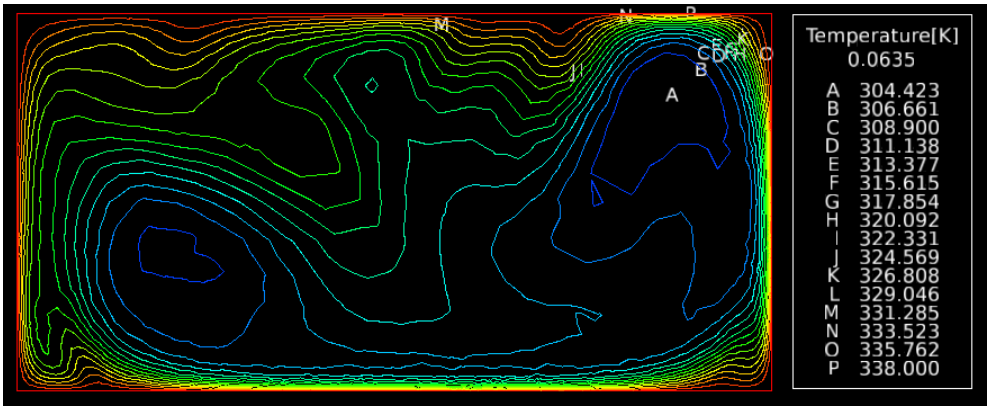

Figure 5.12 Temperature contours in second pass of Case (a), Re = 10,000, $\beta = 90°$.

is 305.1 K in the core flow region. Secondary flow vortices migrate diagonally from the top corner toward the middle of the channel.

Figures 5.15 and 5.16 show the regionally averaged Nusselt number ratios (Nu/Nu_s) from leading and trailing surfaces for Case (a) and Reynolds numbers of 25,000 and 40,000. The Nusselt number ratios for these higher Reynolds number cases generally show less variation with spacial distance within the channel. The high inlet velocities also lead to relatively low rotation numbers of 0.042 and 0.026 for $Re = 25,000$ and $40,000$ respectively. The differences between leading and trailing surfaces at the same spacial location are reduced due to the low rotation numbers. The Nusselt number ratio The plots show a significant overprediction of Nusselt number ratios in the turn region for the compututational results when compored

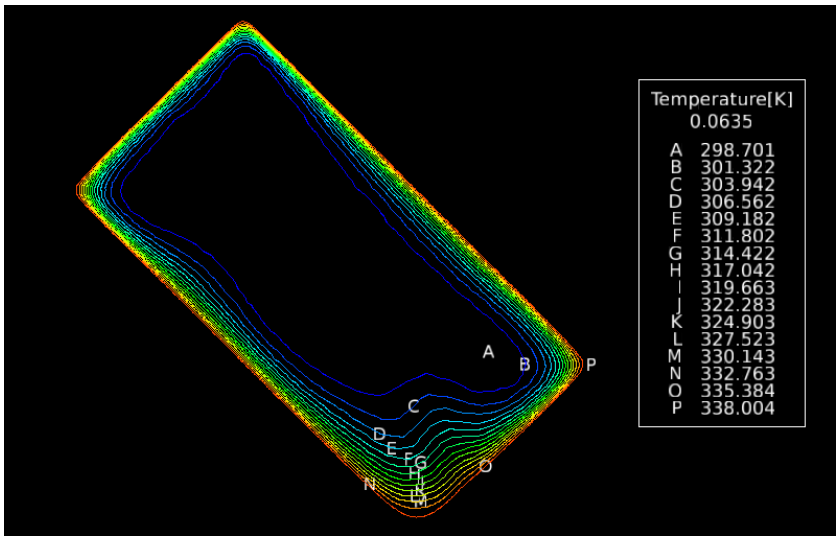

Figure 5.13 Temperatures in first pass of Case (a), Re = 10,000, $\beta = 135°$.

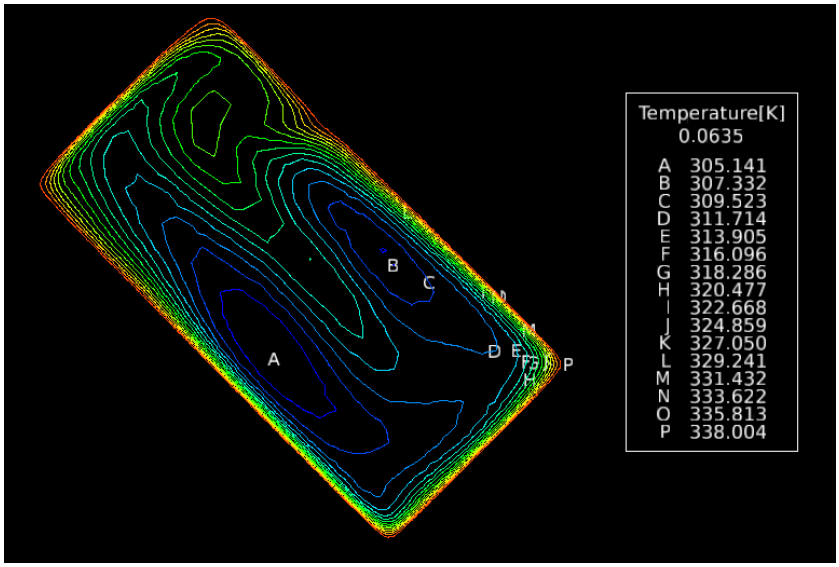

Figure 5.14 Temperatures in second pass of Case (a), Re = 10,000, $\beta = 135°$.

with experimental results. This may be attributable to inadequately calibrated turbulence model parameters. The smooth channel cases present cases that may have much different turbulent intensity and length scales than the cases implementing ribs.

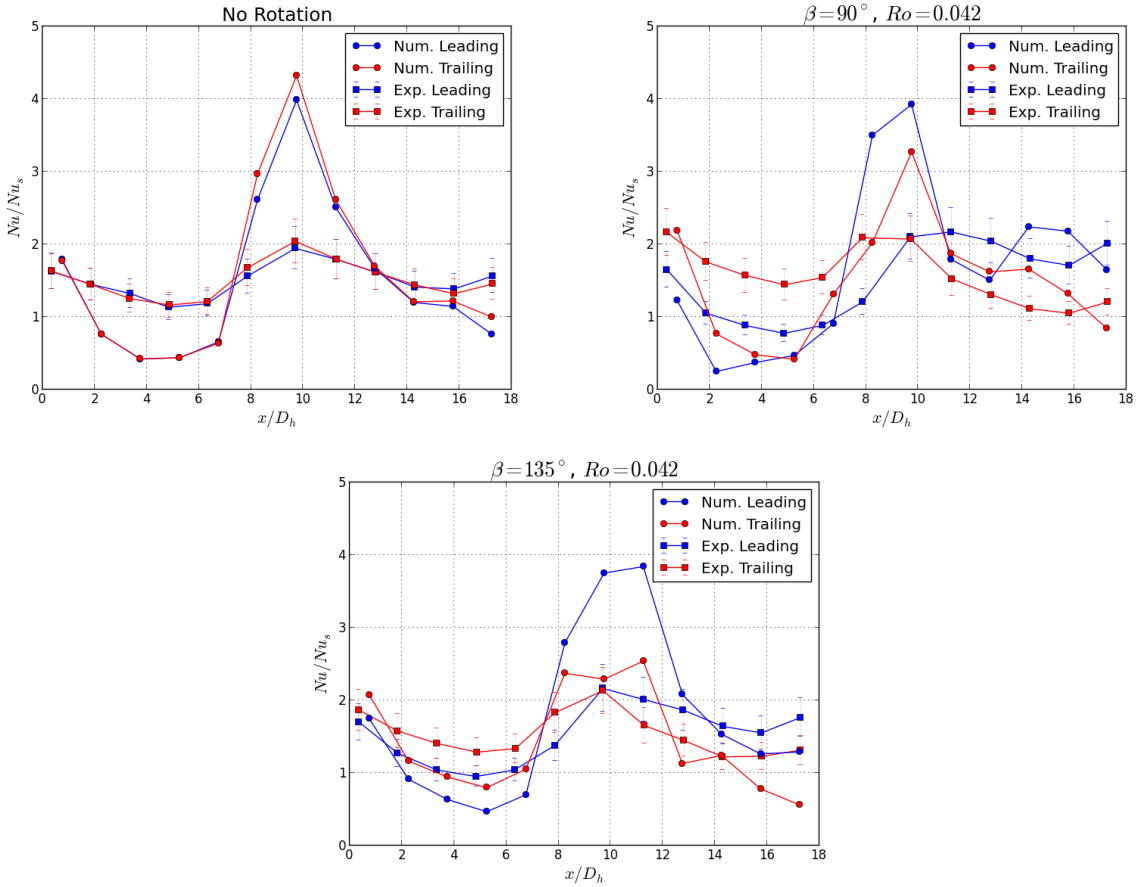

Figure 5.15 Nusselt number ratios for Case (a), Re = 25,000.

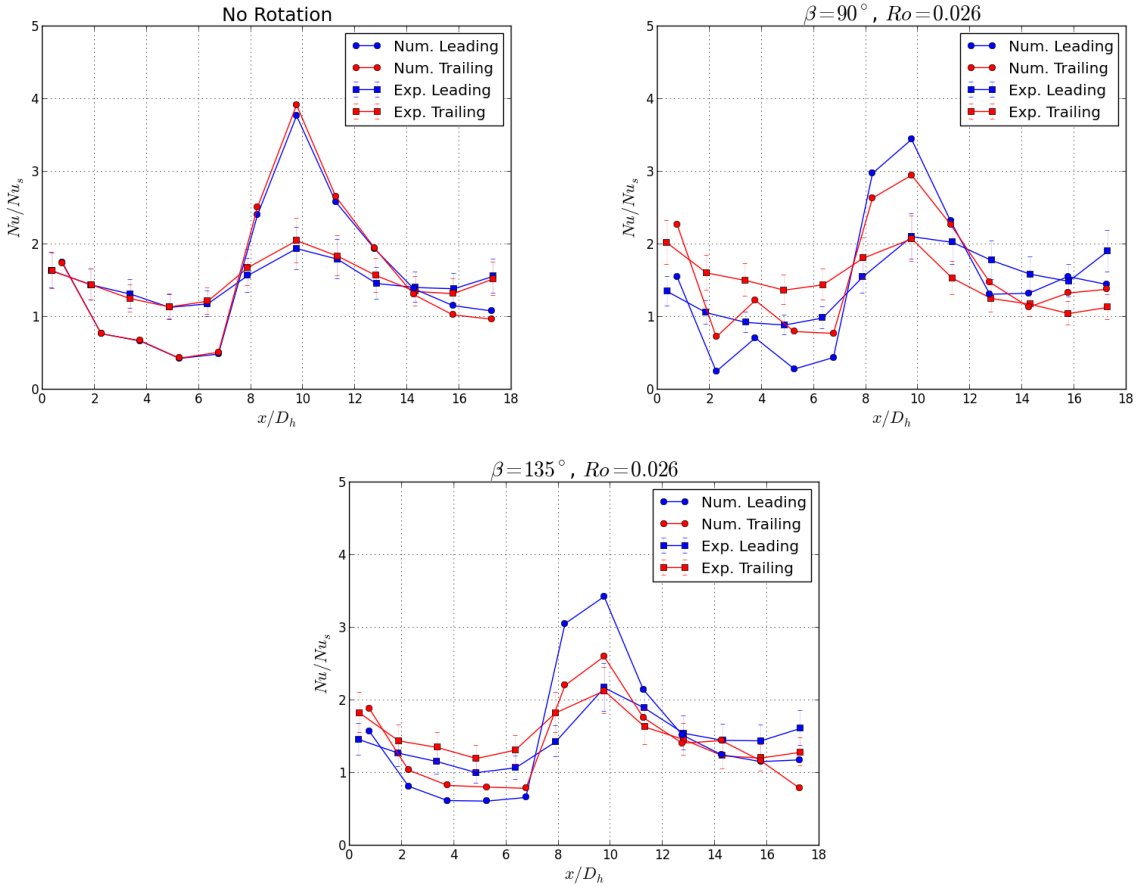

Figure 5.16 Nusselt number ratios for Case (a), Re = 40,000.

Case (c) Results

Case (c) is composed of a rectangular channel, of aspect ratio (AR) equal to 2, with parallel inverted 45° V-shaped ribs in the first pass channel and 45° V-shaped ribs in the second pass channel. Figure 5.17 shows the regionally averaged Nusselt number ratios (Nu/Nu_s) from leading and trailing surfaces within the Case (c) model for $Re = 5,000$. The Nusselt number ratios are the largest for this lowest Reynolds number case. This is both because the Nusselt numbers are normalized by a lower Nu_s which is dependent on Reynolds number, and because the flow is moving slowest in the channel and thus have longer resident times to increase in temperature. The 180° turn region, from $x/D_h \approx 9$ to 11, has the lowest Nusselt number ratios due to the lack of turbulence inducing ribs.

Figure 5.18 shows the regionally averaged Nusselt number ratios (Nu/Nu_s) from leading and trailing surfaces within the Case (c) model for a Reynolds number of 10,000. The lower Reynolds number decreases the Nusselt number ratios as well as the difference between leading and trailing surfaces at a given x/D_h spacial location. For orthogonal rotation of $\beta = 90°$, the trailing surfaces in the first pass channel have higher Nusselt number ratios due to the impingement of the pair of two counter rotating vortices. The directing of impingement switches to the leading surfaces in the second pass channel. Thus, the leading surfaces in the second pass have higher Nusselt number ratio than corresponding trailing surfaces.

For the stationary case, experimental results show the highest Nusselt number ratios occuring in the entrance region of the first pass. It is cited that this is because the thermal boundary layer has yet to become fully developed in this region. The numerical results are significantly lower than the corresponding experimental Nusselt numbers in this region. This can be largely attributed to the use of isothermal boundary conditions in the smooth channel leading up to the heated channel. While this implementation is sufficient in many cases, this case shows strong dependence on the behavior of a developing thermal boundary

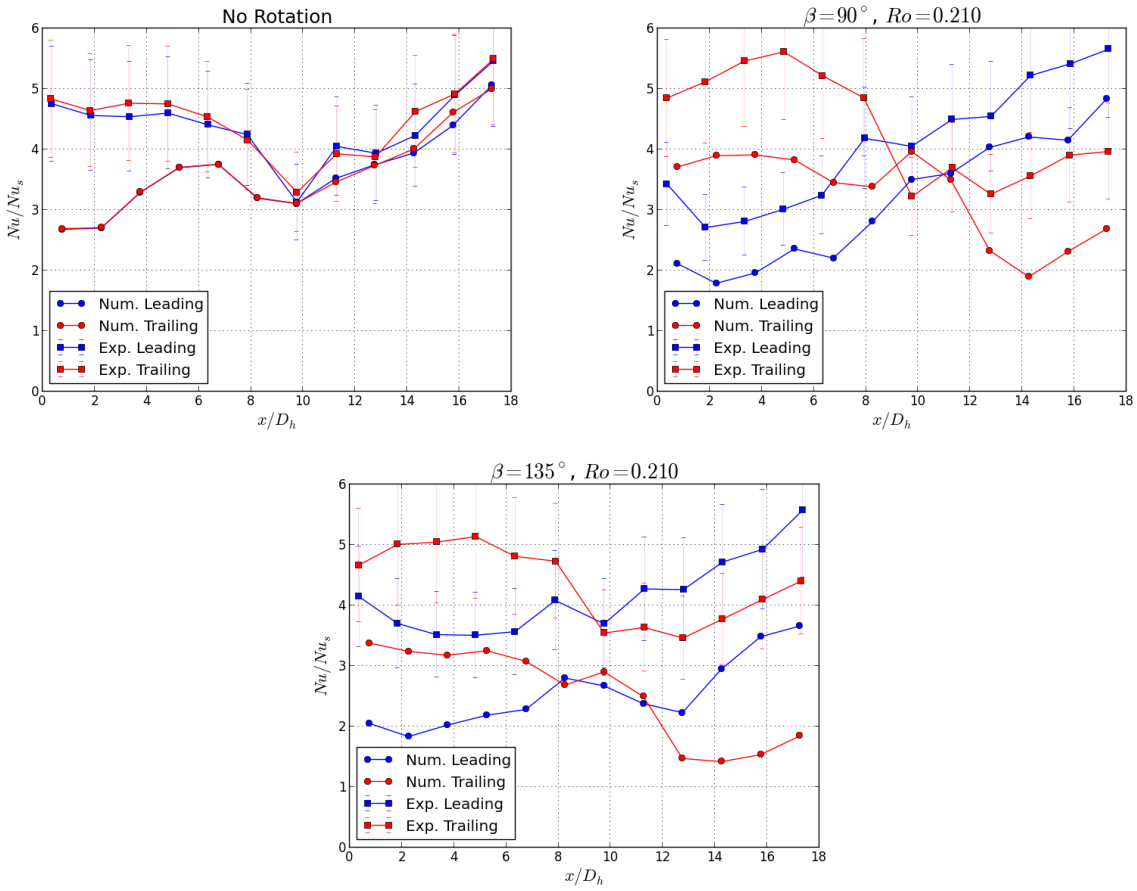

Figure 5.17 Nusselt number ratios for Case (c), Re = 5,000.

layer. The numerical Nusselt numbers tend to match the experiment more closely in the regions downstream of the entrance in the first pass.

Figure 5.19 shows the leading surface pressure distribution across the heated channel for Re = 10,000. The pressure field is displayed using 32 contour segments spanning the color spectrum. Pressure decreases from a maximum of 101,748.5 Pa in red to a local minimum of 101,198 Pa. The red contours at the center of the ribs in the first pass highlight the existence of local stagnation regions.

The inverted V-shaped ribs tend to funnel the near wall fluid toward the center of the channel. They also have the effect of creating a stagnation region at the ribs center. This stagnation region tends to weaken the pair of counter rotating vortices induced by the

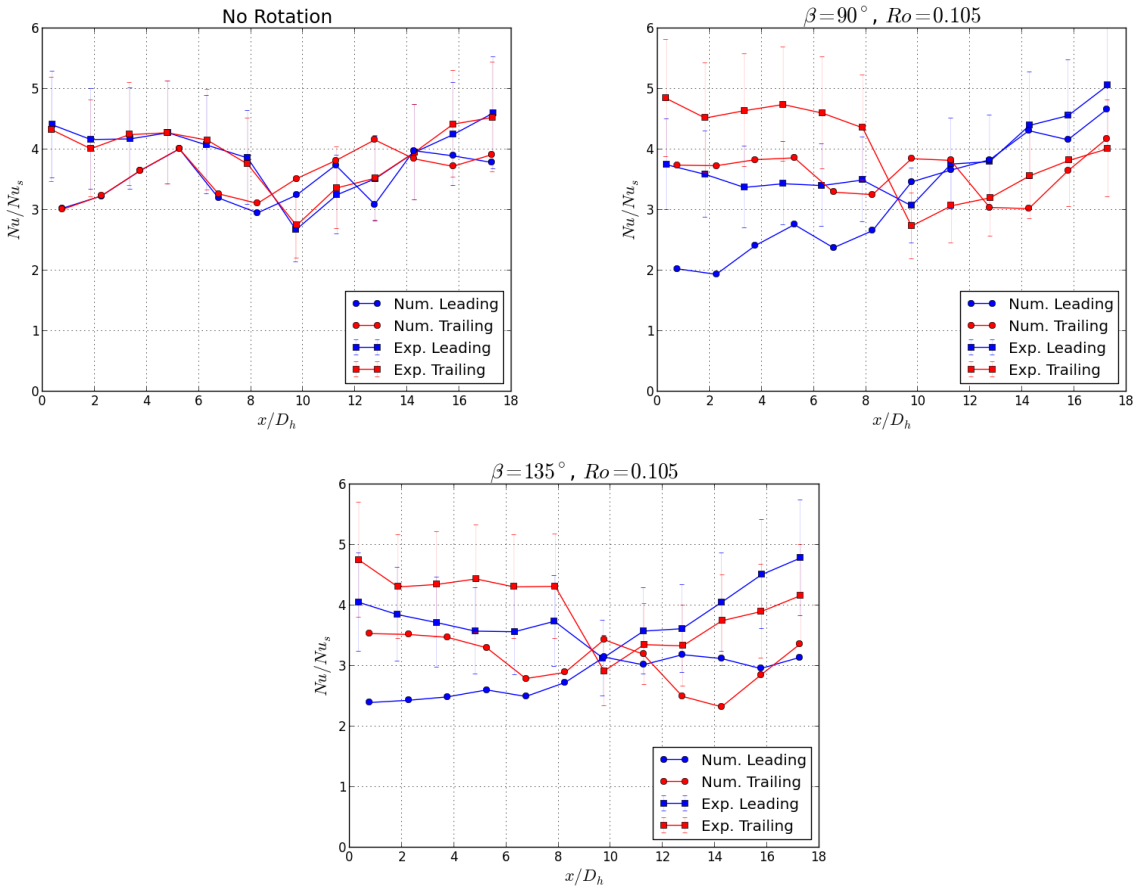

Figure 5.18 Nusselt number ratios for Case (c), Re = 10,000.

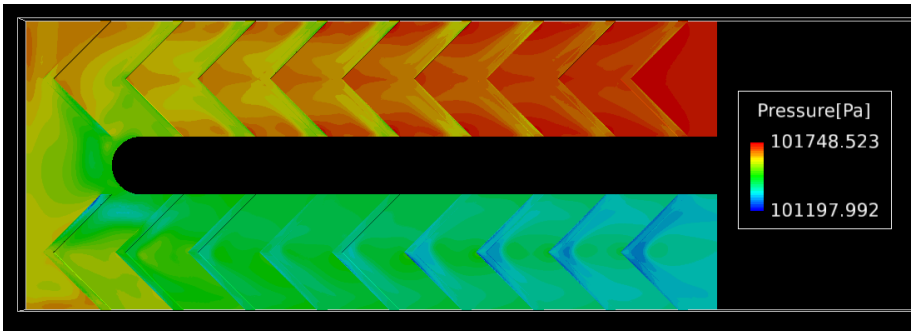

Figure 5.19 Pressure distribution for Case (c), Re = 10,000.

inverted 45° V-shaped ribs. A reduction of mixing between the near surface fluid and mean stream flow is observed as a result of the reduced secondary flow strength. The Nusselt number ratios decrease as the secondary flows are influenced by the sharp 180° turn. The Nusselt number ratios are generally at a minimum when entering the second pass channel. This is due to the decay of turbulence produced by the 180° turn. The Nusselt number ratios continue to increase in the second pass because of the increasing strength of the pair of counter rotating secondary flow vortices induced by the V-shaped ribs as the influence of the 180° turn subsides.

It is evident that rotation significantly increases Nusselt number ratios on the first pass trailing and second pass leading surfaces. This increase in heat tranfer compared to the non-rotating case comes at the expense of lower first pass leading and second pass trailing Nusselt number ratios. The rotation induced secondary flows create a pair of rotating vortices that are normally incident on the first pass trailing and second pass leading surfaces.

Figure 5.20 plots the temperature and velocity vectors on a cutting plane in center of the first pass channel. The temperature field is displayed using 16 contour segments on the color spectrum. The maximum temperature of 338 K at the walls decreases to a minimum of 299 K for the core flow. The thermal boundary layer is seen developing before the flow reaches the first ribs. The flow is then forced over the ribs and causes the core flow region to be quickly reduced by the near wall fluid being forced over the ribs.

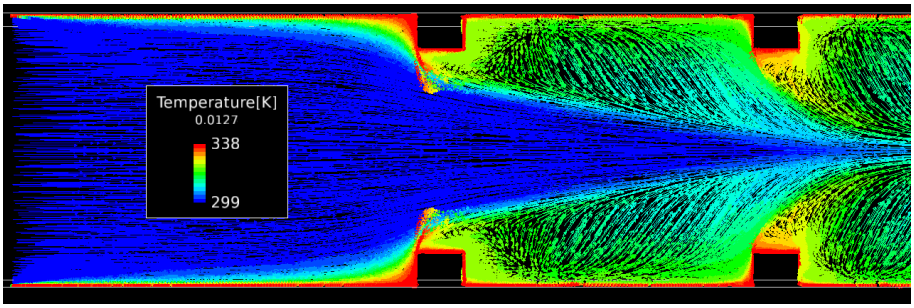

Figure 5.20 First pass temperatures for Case (c), Re = 10,000.

Figure 5.21 again plots the temperature and velocity vectors in the first pass, but on a cutting plane located at $z/D_h = 1/4$. This plane shows a significantly larger core flow region than the plane on the channel centerline. This is due to the parallel inverted 45° V-shaped ribs directing flow from the outer walls and toward the center of the channel. Increased heat transfer is also seen in the region behind the ribs.

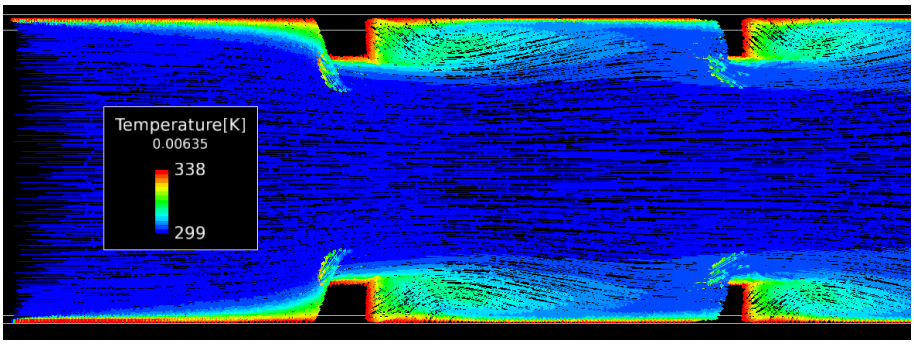

Figure 5.21 Case (c): temperatures at 1/4 channel width in first pass.

Figure 5.22 shows a $y - z$ cutting plane located midway down the first pass channel. It plots the Temperature and velocity distribution for Re = 10,000 and no rotation. The velocity vectors clearly indicate a pair of counter rotating secondary vortices.

Figure 5.23 plots the temperature contours in the first pass channel on a plane at $y = 1.59\ mm$, which is parallel to the top of the ribs. The hottest temperatures of 338 K shown in red are located on the walls and ribbed surfaces. The minimum temperature of 298.5 K shown in blue primarily in the core flow region of the entrance.

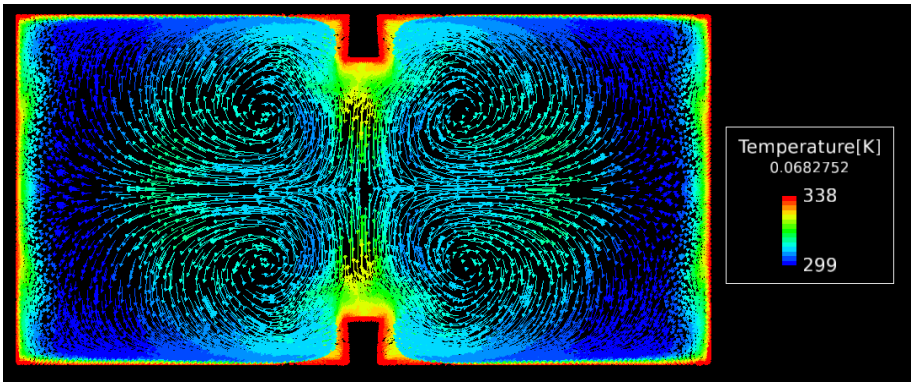

Figure 5.22 Case (c): temperatures midway down first pass channel.

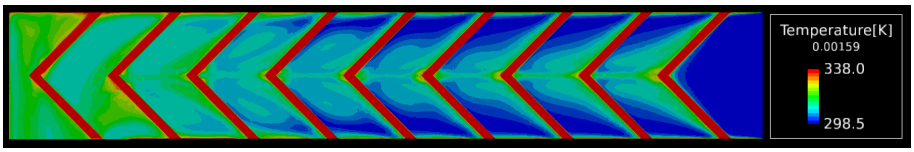

Figure 5.23 Case (c): temperatures on ribs in first pass channel.

Figure 5.24 shows the pressure distribution on the leading surfaces of the heated test section. Pressure decreases from a maximum of 102035 Pa to 101377 Pa. The channel rotation causes increased pressure on the leading surface in the 180° turn region.

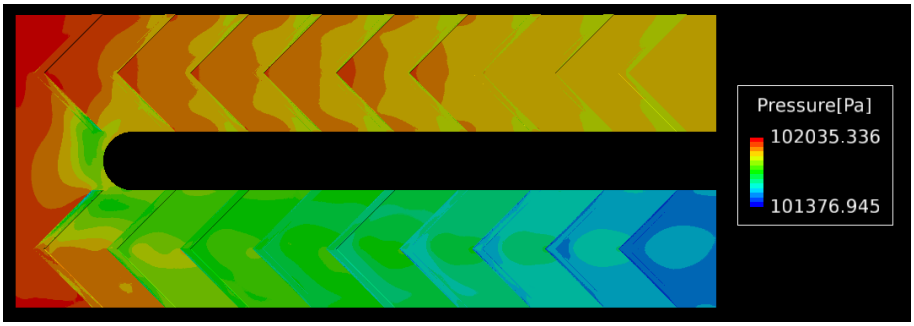

Figure 5.24 Case (c): leading surface pressure distribution, $\beta = 90°$.

Figure 5.25 shows the pressure distribution on the trailing surfaces of the heated test section. While the pressure range is similar to that of the leading surfaces, the zones of high pressure in the 180° turn region are significantly reduced for the trailing surfaces.

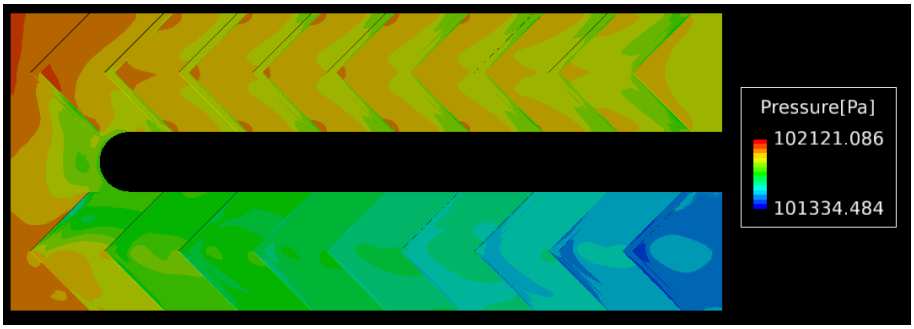

Figure 5.25 Case (c): trailing surface pressure distribution, $\beta = 90°$.

Figure 5.26 shows the temperature contours at the entrance of the first pass channel. The core coolant flow at 300 K is heated by the walls at 338 K. The rotation causes the trailing surface turbulence to increase and transfer more heat to the core flow. The leading surfaces at the bottom show a suppression of turbulence and less heat transfer.

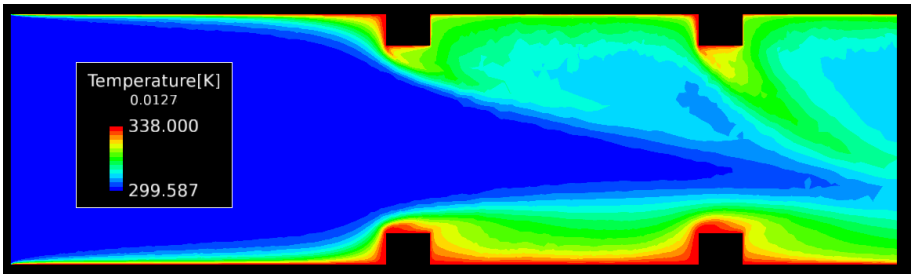

Figure 5.26 Case (c): temperature in first pass, $\beta = 90°$.

Figure 5.27 also shows the temperature contours at the entrance of the first pass channel, but at a 1/4 of the channel width. The near wall fluid is being pushed toward the center of the channel as well as over the ribs. The rotation causes the coldest core flow to move closer to the trailing surfaces than to the leading surfaces.

The temperature contours midway down the first pass channel are shown in Figure 5.28. The trailing surface is exposed to a higher temperature gradient at the surface due to the quick transition from 338 K at the wall to 300 K in the mainstream flow.

The pressure contours midway down the first pass channel are shown in Figure 5.29. The local pressure ranges from 101,871 to 101,956 Pa. It shows two large central vortices

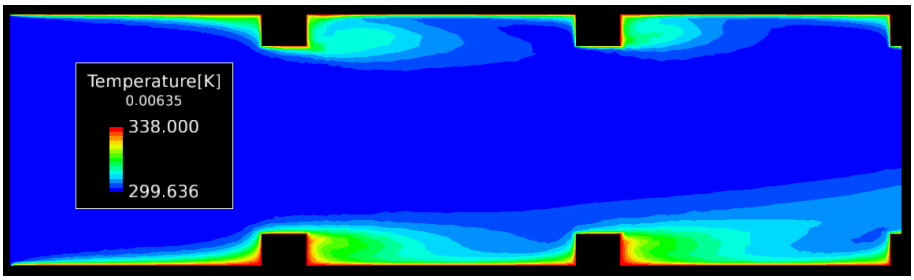

Figure 5.27 Case (c): temperature at $z/D_h = 1/4$ in first pass, $\beta = 90°$.

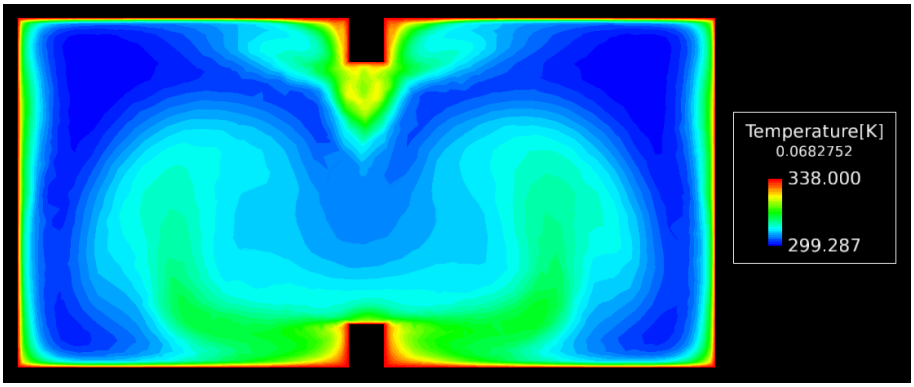

Figure 5.28 Case (c): temperatures midway down the first pass channel, $\beta = 90°$.

in the middle of the channel indicated by the lowest pressures of 101871 Pa in blue. Two more small vorices are seen near the trailing surface. The effect of rotation is to push the secondary vortices up toward the trailing surface.

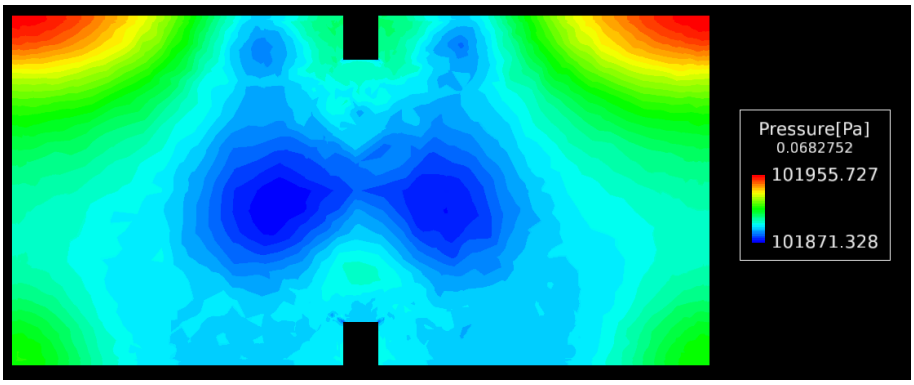

Figure 5.29 Case (c): pressures midway down the first pass channel, $\beta = 90°$.

Figure 5.30 shows the temperature distribution on a constant cross-section at the top of the leading surface ribs. The temperature is clearly increased more toward the center of the inverted 45° V-shaped ribs in the first pass. The second pass temperatures are heated to a near uniform 323 K by the end of the heated test section.

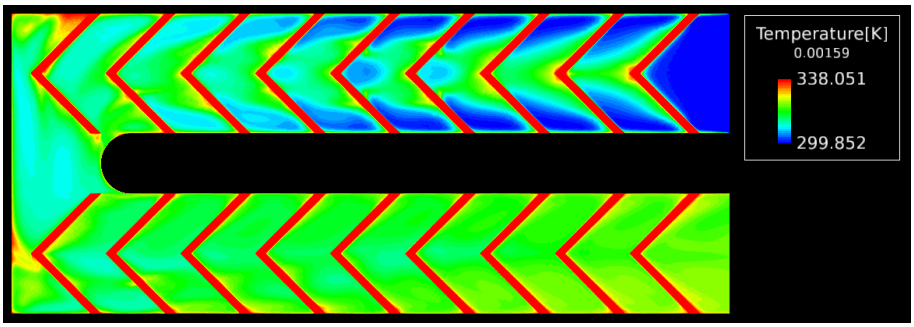

Figure 5.30 Case (c): temperatures at leading surface rib height, $\beta = 90°$.

Figure 5.31 shows the temperature distribution at the top of the trailing surface ribs. For the first pass channel, the regions of cold temperature exposure on the trailing surface are significanty larger than what is observed for the leading surface.

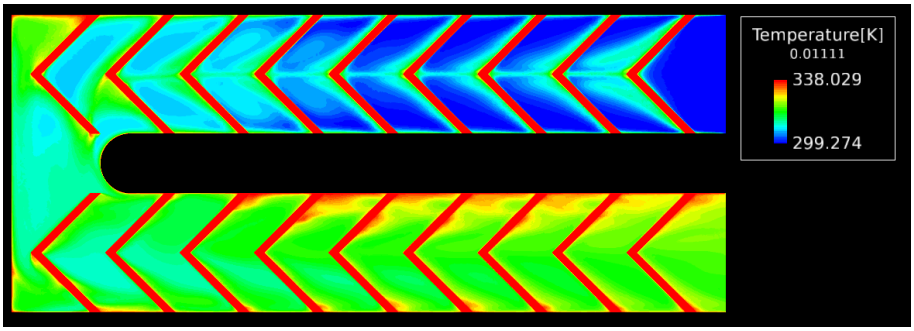

Figure 5.31 Case (c): temperatures at trailing surface rib height, $\beta = 90°$.

Figure 5.32 shows the temperature contours in a center cross-section between the leading and trailing surfaces. On this central plane, the core flow remains 300 K for a third of the first pass channel before it begins to be heated and influenced by the secondary vortices.

Figure 5.33 show the pressure distribution on a plane located midway down the first pass channel when the model is subjected to rotation with $\beta = 135°$. The rotational effects

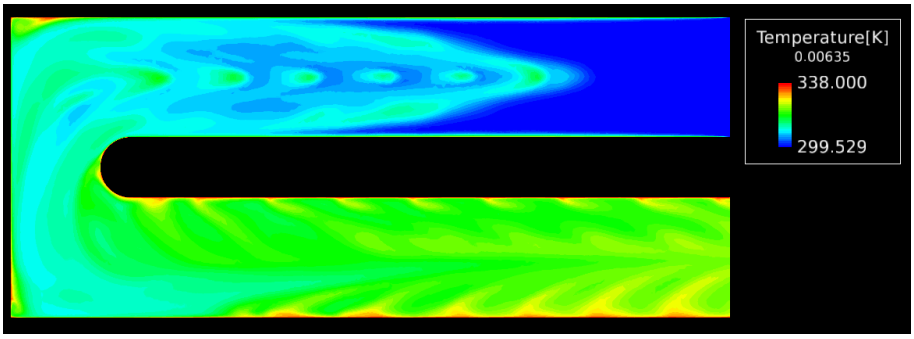

Figure 5.32 Case (c): temperatures in middle of channel, $\beta = 90°$.

are less significant for the 135° channel orientation because the heat transfer surfaces are not orthogonal to the plane of rotation and thus create angled secondary flow impingement. The secondary vortices toward the trailing corner of the channel become stronger than those toward the leading corner as indicated by the increased area of lower pressures around 101,806 Pa.

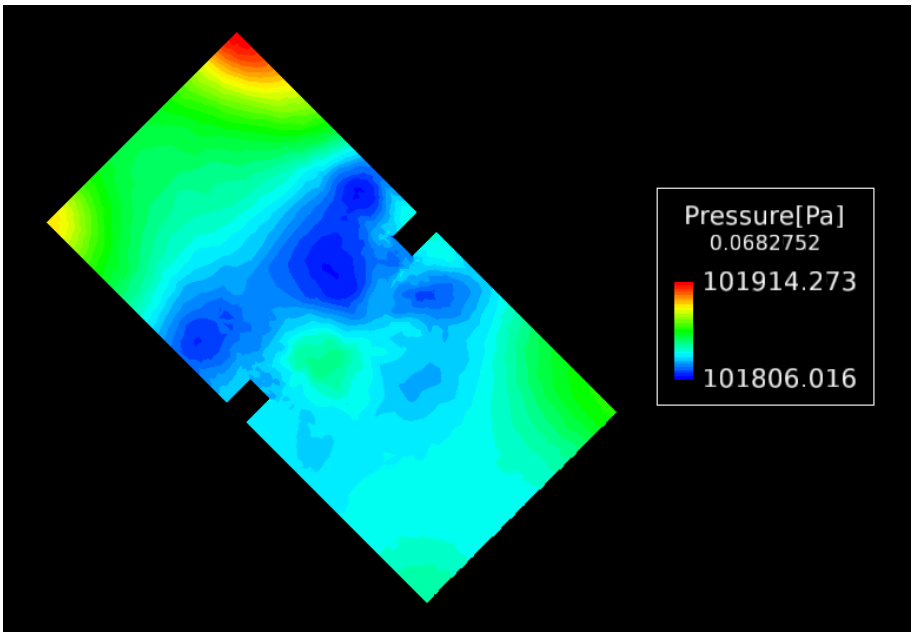

Figure 5.33 Case (c): pressure in first pass, Re = 10,000, $\beta = 135°$.

Figure 5.34 shows the temperatures in the first pass channel. Temperatures are segmented into 32 regions of constant temperatures ranging from 299.1 K to 338 K. The angled

rotation causes a more equal heat transfer from leading and trailing surfaces compared to the orthogonal rotation with $\beta = 90°$.

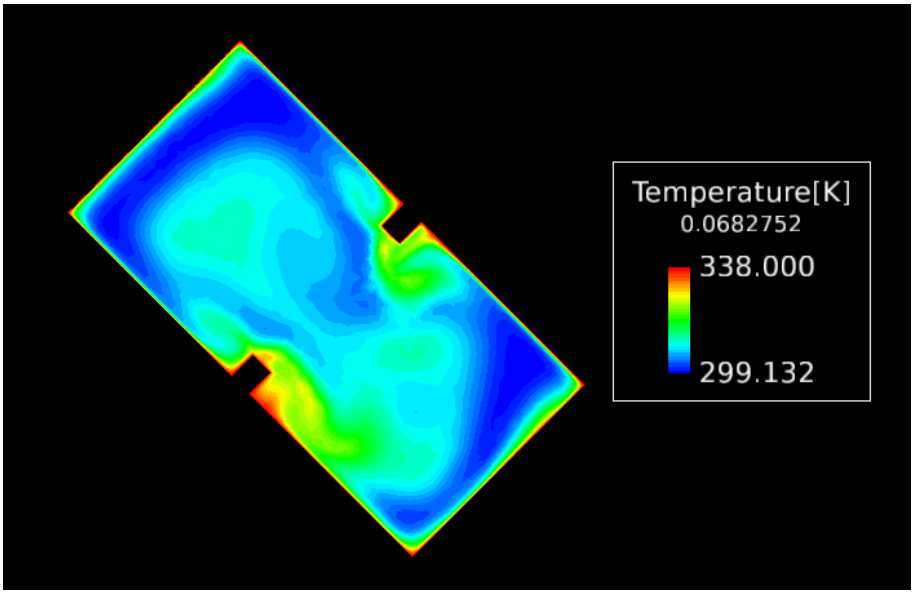

Figure 5.34 Case (c): temperatures in first pass, Re = 10,000, $\beta = 135°$.

Figures 5.35 and 5.36 show the regionally averaged Nusselt number ratios (Nu/Nu_s) from leading and trailing surfaces for Reynolds numbers of 25,000 and 40,000. The Nusselt number ratios for these higher Reynolds number cases show less variation with spacial distance. The high inlet velocities also lead to relatively low rotation numbers of 0.042 and 0.026 for $Re = 25,000$ and $40,000$ respectively. The differences between leading and trailing surfaces at the same spacial location are reduced due to the low rotation numbers.

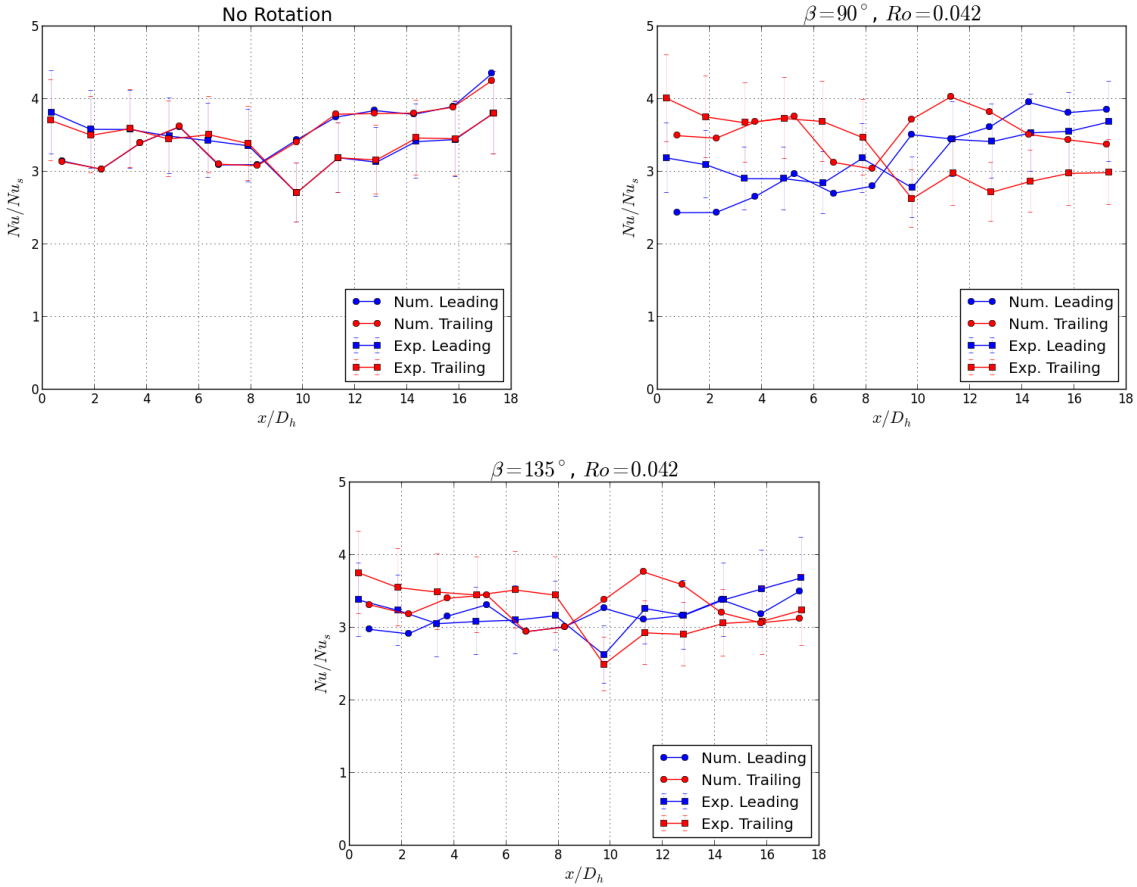

Figure 5.35 Nusselt number ratios for Case (c), Re = 25,000.

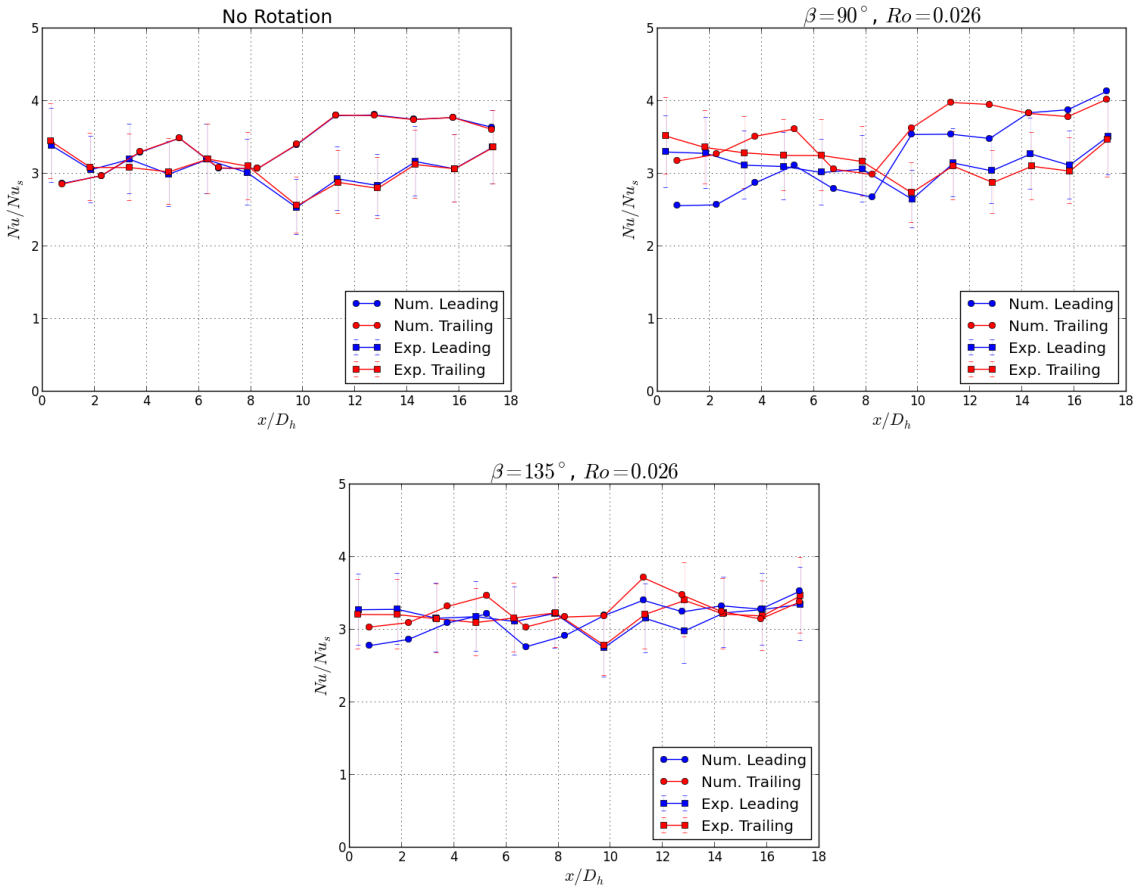

Figure 5.36 Nusselt number ratios for Case (c), Re = 40,000.

Case (d) Results

Case (d) is composed of a rectangular channel, of aspect ratio (AR) equal to 2, with parallel 45° V-shaped ribs in the first pass channel and 45° inverted V-shaped ribs in the second pass channel. Figure 5.37 shows the regionally averaged Nusselt number ratios (Nu/Nu_s) from leading and trailing surfaces within the Case (d) model for $Re = 5,000$. The Nusselt number ratios are the largest for this lowest Reynolds number case. This is both because the Nusselt numbers are normalized by a lower Nu_s which is dependent on Reynolds number, and because the flow is moving slowest in the channel and thus have longer resident times to increase in temperature. For this lowest Reynolds number case, the Nusselt number ratio variations with spacial location are most significant among the Reynold numbers tested. The strong rotational effects cause greatly increased heat transfer for the first pass trailing and second pass leading surfaces. The gradients were so high in certain locations of the flow field that the angled rotation case was not able to converge for $Re = 5,000$.

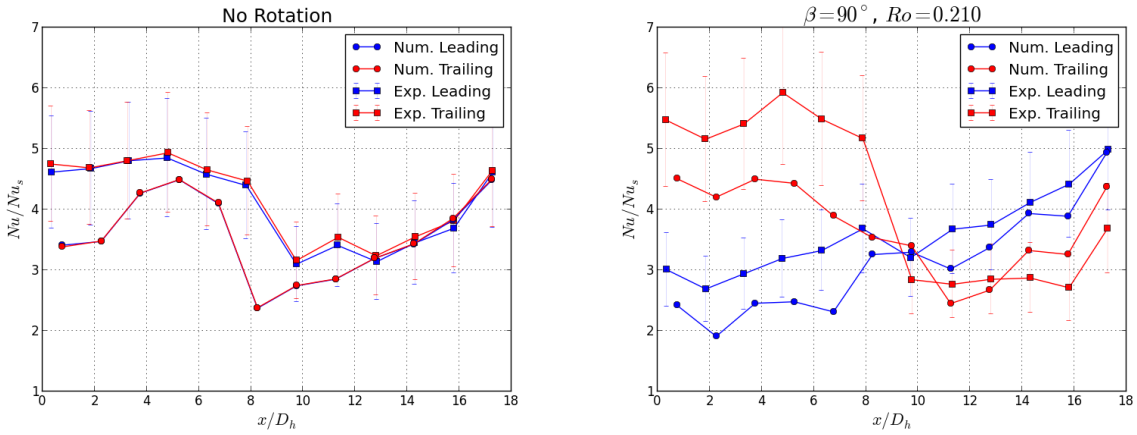

Figure 5.37 Nusselt number ratios for Case (d), Re = 5,000.

Figure 5.38 shows the regionally averaged Nusselt number ratios (Nu/Nu_s) from leading and trailing surfaces within the Case (d) model for a Reynolds number of 10,000. The Nusselt number ratios are highest in the first pass where the V-shaped ribs show good performance.

The second pass Nusselt number ratios tend to flatline with the inverted V-shaped ribs not looking as effective as the V-shaped ribs of the first pass. The Nusselt number ratios only increase because the Nusselt number is calculated with a compoonent divided by a bulk-flow-to-surfacee temperature difference which is getting closer to zero as the fluid is heated.

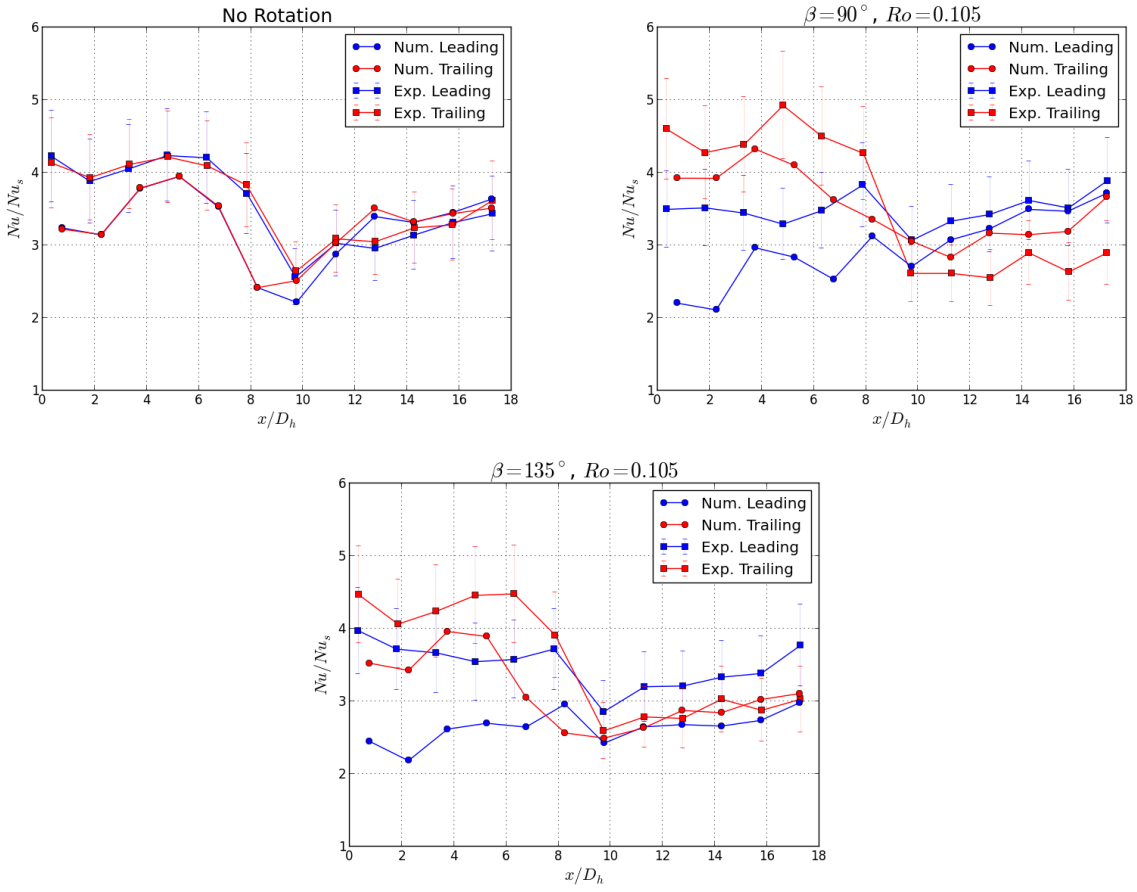

Figure 5.38 Nusselt number ratios for Case (d), Re = 10,000.

The stationary case results show high Nusselt number ratios in the first pass channel downstream of the inlet. This is attributed to the two pairs of counter rotating secondary flow vortices generated by the V-shaped ribs. The Nusselt number ratios then decrease significantly in the turn region as the 180° turn dominates the rib-induced secondary flows. The minimum Nusselt number ratio is found at the inlet of the second pass. With 45°

inverted V-shaped ribs in the second pass channel, the Nusselt number ratios are generally lower than those found in Case (c), which has higher performing parallel 45° V-shaped ribs. The V-shaped ribs tend to generate stronger pairs of counter rotating vortices than the inverted V-shaped ribs. Rotation again causes increased Nusselt number ratios for the first pass trailing and second pass leading surfaces. Results in the the first pass of the channel shows Nusselt number ratios in the first pass channel appear to be significantly influenced by rotation, while the second pass shows much less change when subjected to rotation.

Figure 5.39 shows the pressure distribution at a constant height located on the top of the leading surface ribs in the first pass channel for Re = 10,000 and no rotation. Pressure increases from 101,308 Pa to 101,783 Pa. Stagnation points at the center of each V-shaped rib in the first pass channel show a corresponding rise in pressure as the flow is slowed before it is diverted over the ribs.

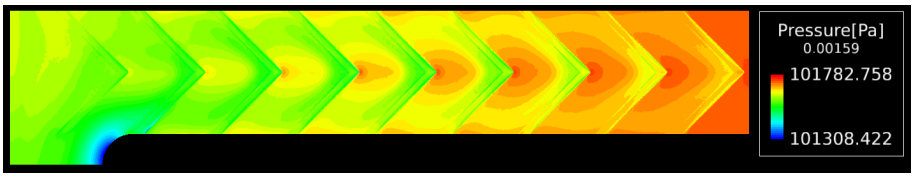

Figure 5.39 Pressure distribution for Case (d), Re = 10,000, no rotation.

Figure 5.40 shows the temperature distribution as well as velocity vectors for each node located on the cutting plane located midway down the first pass channel. The V-shaped ribs cause the near-rib flow to be pushed toward the outer walls. The flow then goes over the ribs and back toward the channel center spawning a pair of two counter rotating secondary vortices. Figure 5.41 shows the corresponding pressure profile at the same position as Figure 5.40, $x/D_h = 3.66$, in the first pass channel. The regions toward the four corners show the lowest local pressures of 101,638 Pa, where secondary flow vortices are induced as the flow goes over the ends of the ribs. High local pressures of 101,712 Pa, are seen at the center of both leading and trailing surfaces as the central flow slows in its approach to the next pair of V-shaped ribs.

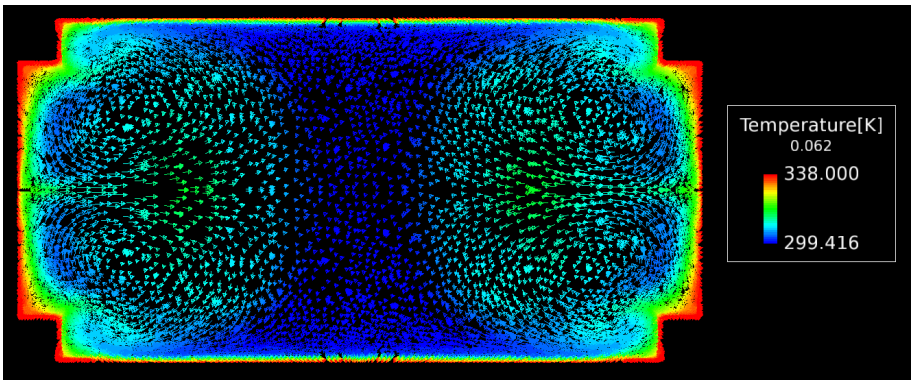

Figure 5.40 Temperatures midway down first pass channel.

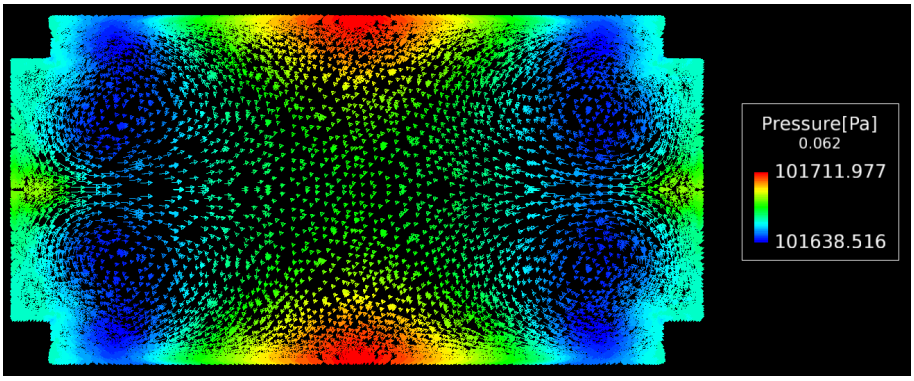

Figure 5.41 Pressures midway down first pass channel.

Figure 5.42 displays the temperature distribution across the heated test section at a height equal to the top of the ribs on the leading surface. The cold flow, with a minimum temperature of 298.9 K, is seen entering the test section from the top right. It is then redirected from the channel center toward the outer walls. Heat is continually transferred to the coolant flow by the walls at a constant 338 K until it exits the channel at the lower right with an average temperature of 323 K.

Figure 5.43 shows the temperature contours on a cross-section plane located midway down the first pass channel when the channel is subjected to orthogonal rotation, $\beta = 90°$, and $Ro = 0.105$. Temperature is delimited by 32 regions of constant temperature ranging from 299.65 K in the mainstream flow to 338 K at the walls. The secondary flow vortices

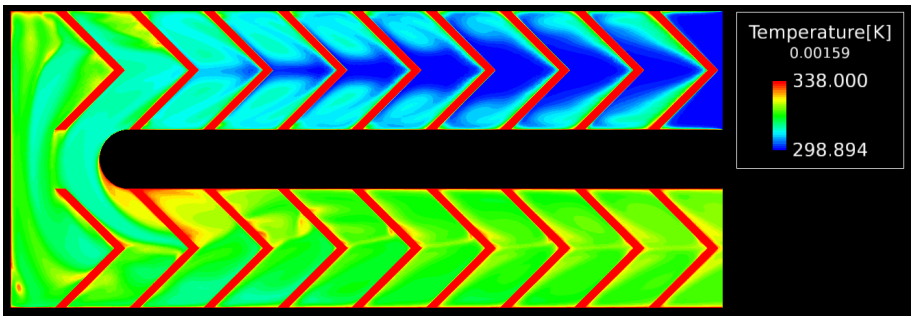

Figure 5.42 Temperature distribution at rib-height, Re = 10,000, no rotation.

induced by rotation cause the mainstream flow to be pushed toward the trailing surface. The secondary flow vortices induced by the ribs are also shifted toward the trailing surface.

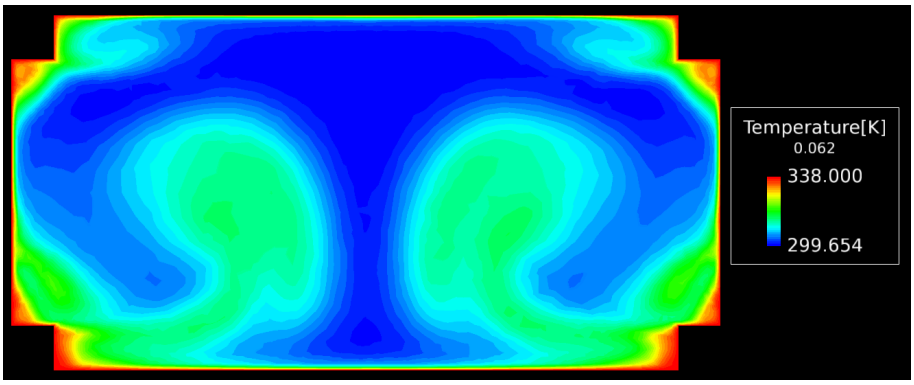

Figure 5.43 Temperatures midway down first pass, $\beta = 90°$.

Figure 5.44 shows the pressure distribution on the same plane in the first pass channel. The four lowest pressure regions at 101,848 Pa identify the locations of the two pair of secondary vortices induced by the ribs. Rotation also creates higher pressure on the trailing surface than the leading surface.

Figures 5.45 and 5.46 display the temperature distribution across the heated test section at a height equal to the top of the ribs on the leading and trailing surfaces, respectively. The cold flow is redirected from the channel center toward the outer walls in the first pass. Rotation causes the mainstream flow to move closer to the trailing surface in the first pass.

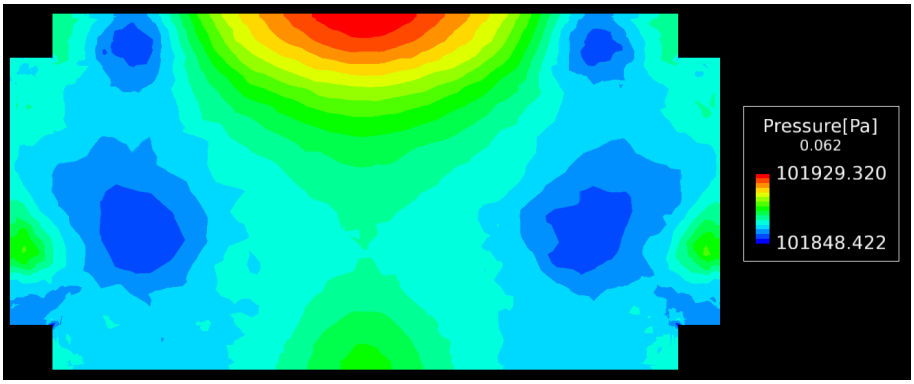

Figure 5.44 Pressures midway down first pass, $\beta = 90°$.

Heat is continually transferred to the coolant flow by the walls at a constant 338 K until it exits the channel at the lower right with an average temperature of 323.7 K.

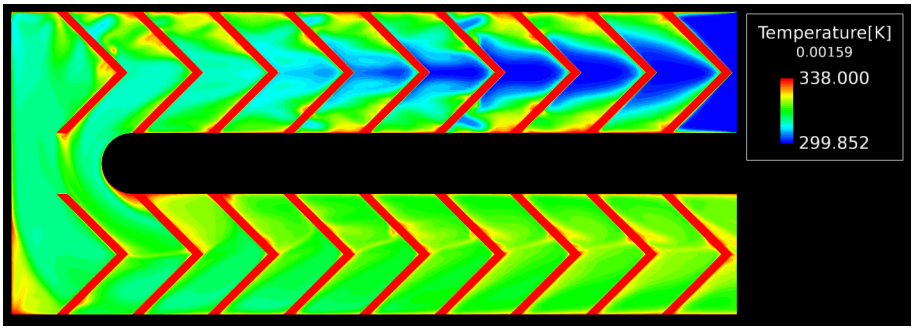

Figure 5.45 Temperatures at rib-height on leading surface, $\beta = 90°$.

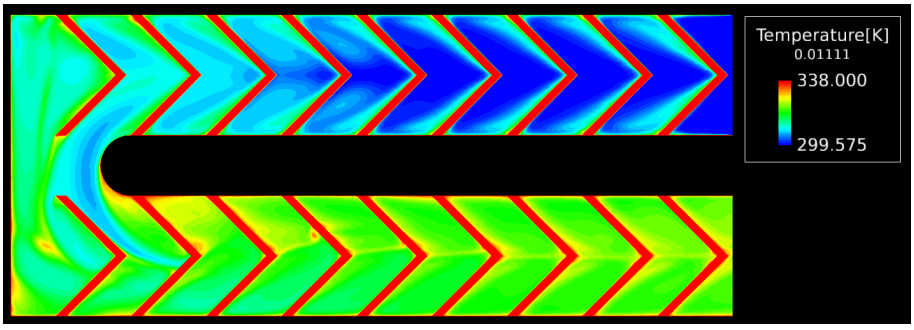

Figure 5.46 Temperatures at rib-height on trailing surface, $\beta = 90°$.

Figure 5.47 show the temperature distribution on a plane located midway down the first pass channel when the Case (d) model is subjected to rotation with $\beta = 135°$. The

rotational effects on heat transfer are less significant for the 135° channel orientation because the channel surfaces are not orthogonal to the plane of rotation and thus create angled secondary flow impingement. The secondary vortices caused by the angled rotation are directed from the bottom corner to the top corner. This causes a more equal heat transfer from leading and trailing surfaces compared to the orthogonal rotation with $\beta = 90°$.

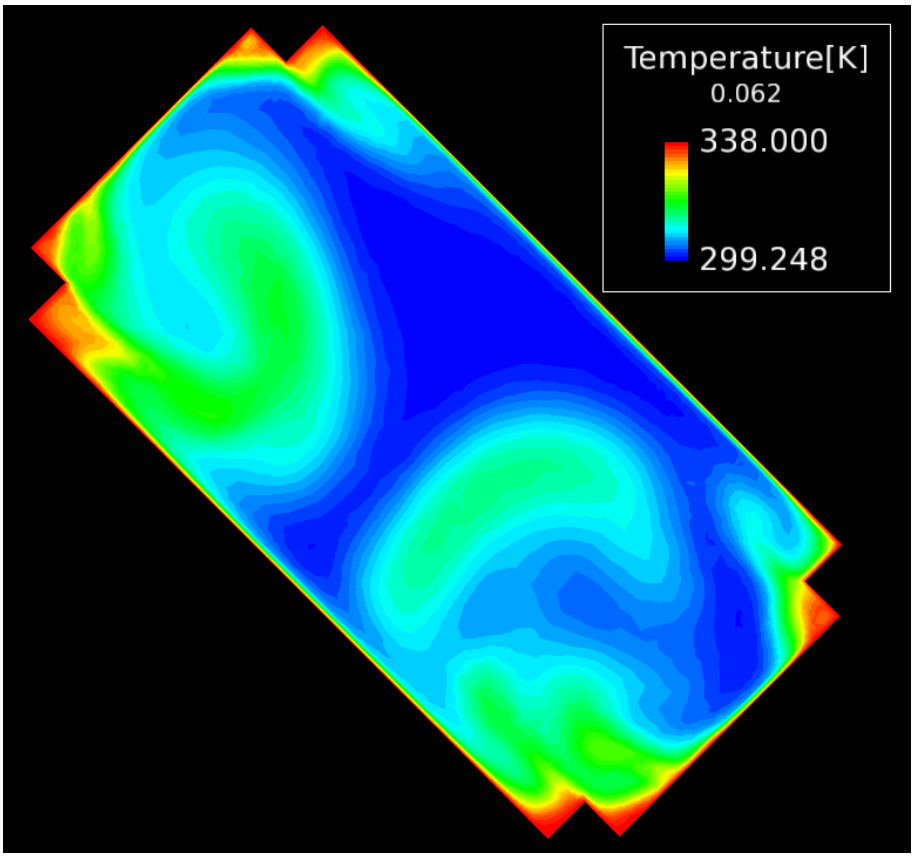

Figure 5.47 Temperatures midway down first pass, $\beta = 135°$.

Figures 5.48 and 5.49 show the regionally averaged Nusselt number ratios (Nu/Nu_s) from leading and trailing surfaces within the Case (d) model for Reynolds number of 25,000 and 40,000 respectively. The effectiveness of V-shaped ribs in the first pass is seen as the induced rotation creates higher Nusselt number ratios in the first pass. The higher Reynolds number necessitates a lower rotation number which results in less impact of rotation on Nusselt number ratios.

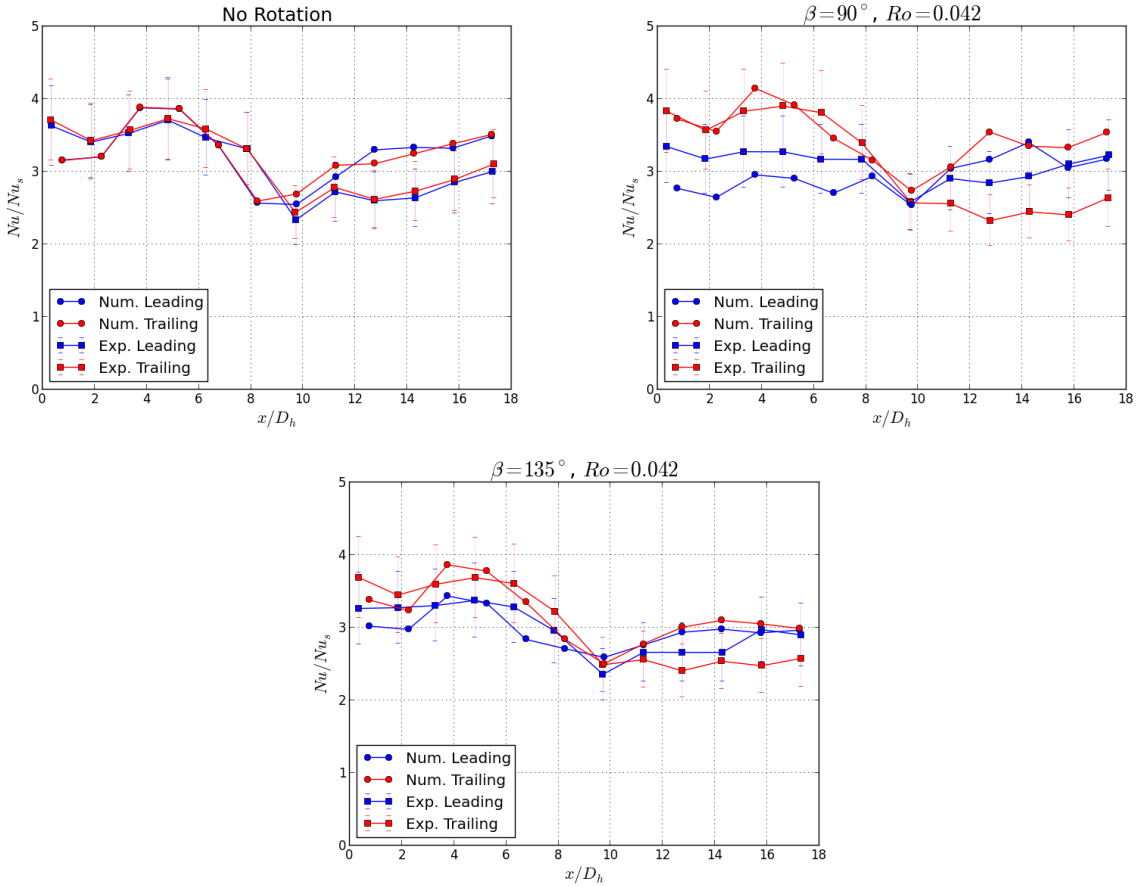

Figure 5.48 Nusselt number ratios for Case (d), Re = 25,000.

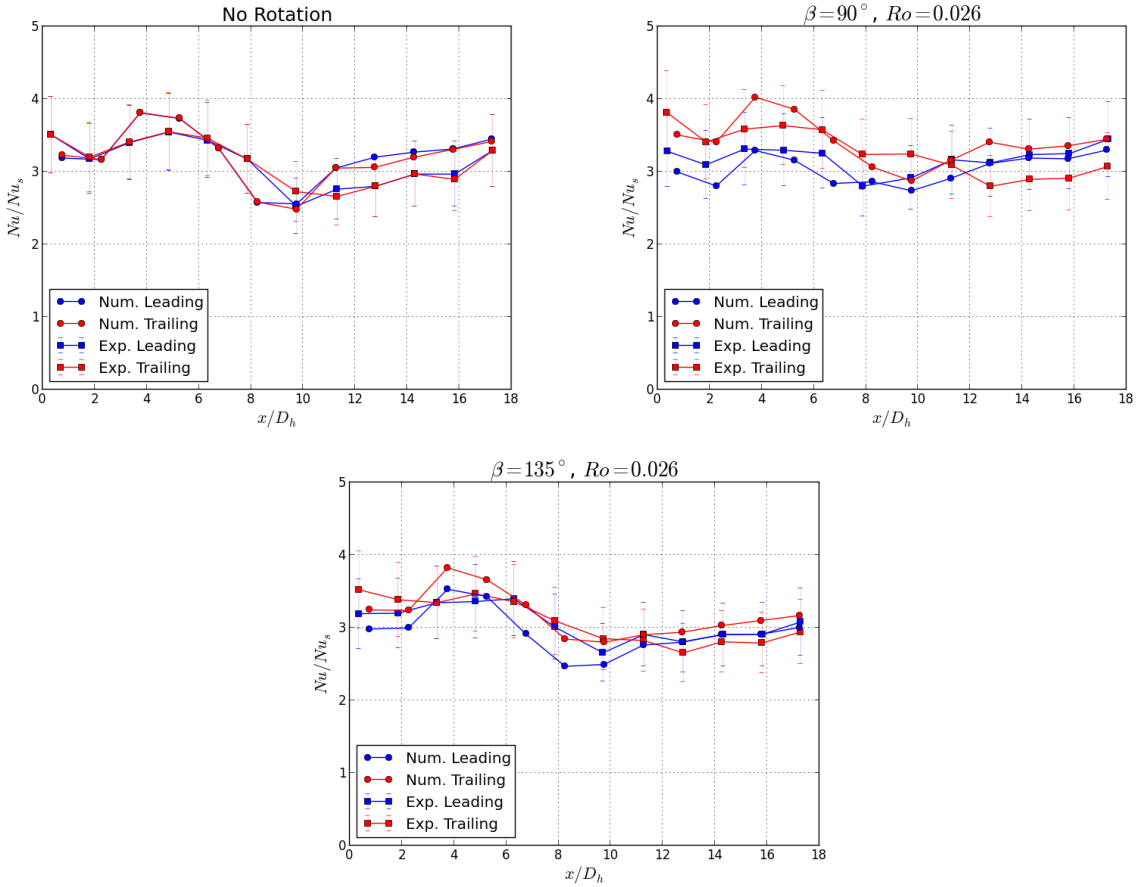

Figure 5.49 Nusselt number ratios for Case (d), Re = 40,000.

CHAPTER 6

CONCLUSIONS

Two-pass Square Channel

The influence of 45° angled ribs and channel orientation on the local Nusselt number ratios for leading and trailing surfaces in a two-pass square channel have been reported for Reynolds numbers from 5,000 to 25,000 and rotation numbers from 0.0 to 0.11. The finidings are:

Rotation causes significant changes to the local Nusselt number ratio distribution relative to stationary conditions. Generally, the first pass trailing and second pass leading surfaces have increased local Nusselt number ratios due to the secondary flow impingement induced by rotation. Alternatively, the first pass leading and second pass trailing surface Nusselt number ratios tend to decrease with increased rotation. The Coriolis forces causes flow moving radially outward to have a different dependence on rotation than bulk flow moving radially inward. The effect of the Coriolis force to induce cross-stream secondary flow is reduced as the channel orientation increases from $\beta = 90°$ to $\beta = 135°$. Results show the lowest Nusselt number ratios consistently occur in the 180° turn region; primarily due to the lack of ribs in this region.

Two-pass Rectangular Channel

The influence of channel orientation and 45° V-shaped rib arrangements on the local Nusselt number ratios for leading and trailing surfaces in a two-pass rectangular channel have been reported for Reynolds numbers from 5,000 to 40,000 and rotation numbers from 0.0 to 0.21. The finidings are:

Generally, the first pass trailing and second pass leading surfaces have increased local Nusselt number ratios due to the secondary flow impingement induced by rotation. Conversely, the local Nusselt number ratios for the first pass leading and second pass trailing surface tend to decrease with increased rotation. Rotation induces Coriolis forces and bouyancy forces which create cross-stream secondary flows that can both enhance and decrease local Nusselt number ratios. The effects of Coriolis forces are reduced as the channel orientation increases from $\beta = 90°$ to $\beta = 135°$. Thus, the local Nusselt number ratios for the first pass trailing and second pass leading surfaces decrease for $\beta = 135°$ compared to their corresponding configuration with the $\beta = 90°$ channel orientation. Also, the first pass leading and second pass trailing surfaces are enhanced for $\beta = 135°$ compared to similar configurations with $\beta = 90°$.

Limitations of the Present Work

The curent study uses air at atmospheric pressure as the coolant fluid. Turbine rotor blades would typically operate using compressed air at higher densities as a coolant. Wall temperatures in turbine blades would also are be much higher under normal operation than those used in this study to match experimental results. While these simulations use comparable non-dimensional operating parameters, the actual performance of real turbine conditions may vary significantly from predictions. The experimental data used for comparison have inherent uncertainties. It is unknown exactly how much heat is lost to the environment surrounding the rotating test section. The exact ribs placement with respect to entrance and turn region distribution is uknown. The exact geometry of the 180° turn is also an unknown. A thorough calibration of the buoyancy parameters and turbulence model would likely help to more accurately resolve the flow behavior in the channel.

Recommendations for Future Work

In the course of this study, various areas of further research where identified. Varying channel aspect ratios (AR) could lead to a deeper understanding of how internal channels in turbine blades could be improved to optimize coolant fluid flow and heat transfer. More research is needing into the effect of buoyancy and its impact on fluid flow behavior as a result of rotation and heat transfer. Models that implement real-world operating conditions could support the development of more accurate predictions of heat transfer. Different thermal boundary conditions such as high surface heat flux can be compared to effects of constant surface temperature conditions. Studies are needed to determine the effects of different rib configurations such as broken V-shaped ribs or wedges. Han and Chen, in their comprehensive review of turbine blade internal cooling, highlight the need for more studies involving "blade-shaped coolant passages (realistic cooling passage geometry, shape, and orientation) with high-performance turbulators and with or without film cooling holes under higher coolant flow (Reynolds number up to 5×10^5), thermal (buoyancy parameter up to 5), and rotation (rotation number up to 0.5) conditions" [22]. While we are currently able to run these cases numerically, the experimental results are lacking and we are therefore left without any direct comparison or validation of obtained results.

REFERENCES

[1] B. V. Johnson and J. H. Wagner and G. D. Steuber and F. C. Yeh, "Heat Transfer in Rotating Serpentine Passages with Selected Model Orentations for Smooth or Skewed Trip Walls," *ASME Journal of Turbomachinery*, Vol. 116, 1994, pp. 738–744. 1, 3, 4

[2] B. V. Johnson and J. H. Wagner and G. D. Steuber and F. C. Yeh, "Heat Transfer in Rotating Serpentine Passages with Trips Skewed to the Flow," *ASME Journal of Turbomachinery*, Vol. 116, 1994, pp. 113–123. 1, 3

[3] Han, J.-C., Dutta, S., and Ekkad, S., *Gas Turbine Heat Transfer and Cooling Technology*, Taylor & Francis, New York, 2000. 1

[4] J. C. Han and P. Zhang, "Effect of Rib-Angle Orientation on Local Mass Transfer Distribution in a Three-Pass Rib-Roughened Channel," *ASME Journal of Turbomachinery*, Vol. 113, 1991, pp. 123–130. 1, 2

[5] Han, J., Zhang, Y., and Lee, C., "Augmented heat transfer in square channels with parallel, crossed, and V-shaped angled ribs," *ASME Journal of Heat Transfer*, Vol. 113, 1991, pp. 590–596. 2

[6] Ekkad, S. V. and Han, J.-C., "Detailed Heat Transfer Distributions in Two-Pass Square Channels with Rib Turbulators," *International Journal of Heat and Mass Transfer*, Vol. 40, No. 11, 1997, pp. 2525–2537. 2

[7] Wagner, J., Johnson, B., and Hajek, T., "Heat transfer in rotating passage with smooth walls and radial outward flow," *ASME Journal of Turbomachinery*, Vol. 113, 1991, pp. 42–51. 2, 29

[8] Wagner, J., Johnson, B., and Kooper, F., "Heat transfer in rotating passage with smooth walls," *ASME Journal of Turbomachinery*, Vol. 113, No. 3, 1991, pp. 321–330. 2, 29

[9] Taslim, M. E., Rahman, A., and Spring, S. D., "An experimental investigation of heat transfer coefficients in a spanwise rotating channel with two opposite rib-roughened walls," *ASME Journal of Turbomachinery*, Vol. 113, 1991, pp. 75–82. 3

[10] Al-Hadhrami, L. and Han, J.-C., "Effect of Rotation on Heat Transfer in Two-Pass Square Channels with Five Different Orientations of 45° Angled Rib Turbulators," *International Journal of Heat and Mass Tranfser*, Vol. 46, 2003. 3, 8, 19, 20, 21, 22, 23, 24, 30

[11] Han, J., Zhang, Y., and Kalkuehler, K., "Uneven wall temperature effect on local heat transfer in a rotating two-pass square channel with smooth walls," *ASME Journal of Heat Transfer*, Vol. 115, No. 4, 1993, pp. 912–920. 4, 19

[12] Parsons, J. A., Han, J.-C., and Zhang, Y., "Wall heating effect on local heat transfer in a rotating two-pass square channel with 90° rib turbulators," *International Journal of Heat and Mass Transfer*, Vol. 37, No. 9, 1994, pp. 1411–1420. 4

[13] Parsons, J. A., Han, J.-C., and Zhang, Y., "Effect of model orientation and wall heating condition on local heat transfer in a rotating two-pass square channel with rib turbulators," *International Journal of Heat and Mass Transfer*, Vol. 38, No. 7, 1995, pp. 1151–1159. 4

[14] Dutta, S. and Han, J., "Local heat transfer in rotating smooth and ribbed two-pass square channels with three channel orientations," *ASME Journal of Heat Transfer*, Vol. 118, 1996, pp. 578–584. 4, 5

[15] Park, C. and Lau, S., "Effect of channel orientation of local heat (mass) distributions in a rotating two-pass square channel with smooth walls," *ASME Journal of Heat Transfer*, Vol. 120, 1998, pp. 624–632. 5

[16] Park, C., Yoon, C., and Lau, S., "Heat (mass) transfer in a diagonally oriented rotating two-pass channel with rib-roughened walls," *ASME Journal of Heat Transfer*, Vol. 122, 2000, pp. 208–211. 5

[17] Huh, M., Liu, Y.-H., and Han, J.-C., "Effect of rib height on heat transfer in a two pass rectangular channel (AR = 1:4) with a sharp entrance at high rotation numbers," *International Journal of Heat and Mass Transfer*, Vol. 52, 2009, pp. 4635–4649. 5

[18] Taslim, M., Bondi, L., and Kercher, D., "An experimental investigation of heat transfer in an orthogally rotating channel roughened with 45 degree criss-cross ribs on two opposite walls," *Journal of Turbomachinery*, Vol. 113, July 1991, pp. 346–353. 5

[19] Fu, W.-L., Wright, L. M., and Han, J.-C., "Heat transfer in two-pass rotating rectangular channels (AR=1:2 and AR=1:4) with 45 deg angled rib turbulators," *ASME Journal of Turbomachinery*, Vol. 127, January 2005, pp. 164–174. 5, 6

[20] Bonhoff, B., Parneix, S., Leusch, J., Johnson, B. V., Schabacker, J., and Bölcs, A., "Experimental and numerical study of developed flow and heat transfer in coolant channels with 45 degree ribs," *International Journal of Heat and Fluid Flow*, Vol. 20, 1999, pp. 311–319. 6

[21] Iacovides, H., Jackson, D. C., Kelemenis, G., and Lau, B. E., "Flow and heat transfer in a rotating U bend with 45 degree ribs," *International Journal of Heat and Fluid Flow*, Vol. 22, 2001, pp. 308–314. 6

[22] Han, J.-C. and Chen, H.-C., "Turbine Blade Internal Cooling Passages with Rib Turbulators," *AIAA Journal of Propulsion and Power*, Vol. 22, No. 2, March 2006. 6, 80

[23] Murata, A. and Mochizuki, S., "Comparison between laminar and turbulent heat transfer in a stationary square duct with transverse or angled rib turbulators," *International Journal of Heat and Mass Transfer*, Vol. 44, 2001, pp. 1127–1141. 6

[24] Viswanathan, A. and Tafti, D., "Detached eddy simulation of turbulent flow and heat transfer," *International Journal of Heat and Fluid Flow*, Vol. 27, 2006, pp. 1–20. 7

[25] Sewall, E. and Tafti, D., "Large Eddy Simulation of Flow and Heat Tranfer in the Developing Flow Region of a Rotating Gas Turbine Blade Internal Cooling Duct With Coriolis and Buoyancy Forces," *Journal of Turbomachinery*, Vol. 130, 2008, pp. 011005–1–011005–7. 7

[26] Valentino, M. I., Tran, L. V., Ricklick, M., and Kapat, J. S., "Comparison of Heat Transfer and Friction Augmentation for Symmetric and Non-Symmetric Wedge Turbulators on Two Opposite Walls," 1 [40], p. 6021, p. 6021. 7

[27] Taslim, M. E. and Spring, S., "Effects of Turbulator Profile and Spacing on Heat Transfer and Friction in a Channel," *Journal of Thermophysics and Heat Transfer*, Vol. 8, No. 3, July 1994. 8

[28] Kamali, R. and Binesh, A., "The importance of rib shape effects on the local heat transfer and flow friction characteristics of square ducts with ribbed internal surfaces," *International Communications in Heat and Mass Transfer*, Vol. 35, June 2008, pp. 1032–1040. 8

[29] Mahadevan, S., Ricklick, M., and Kapat, J., "End Wall Heat Transfer and Pressure Drop Measurements in a Rectangular
channel with porous turbulators," 4 [40], p. 6097, p. 6097. 8

[30] Liou, T.-M., Hwang, J.-J., and Chen, S.-H., "Turbulent Transport Phenomena in a Channel with Periodic Rib Turbulators," *Journal of Thermophysics and Heat Transfer*, Vol. 6, No. 3, July 1992. 8

[31] Rallabandi, A. P., Yang, H., and Han, J.-C., "Heat transfer and pressure drop correlations for square channels with 45 deg ribs at high reynolds numbers," *ASME Journal of Heat Transfer*, Vol. 131, July 2009. 8

[32] Taylor, L. K., *Unsteady Three-Dimensional Incompressible Algorithm Based on Artificial Compressibility*, Ph.D. thesis, Mississippi State University, May 1991. 11

[33] Hyams, D. G., *An Investigation of Parallel Implicit Solution Algorithms for Incompressible Flows on Unstructured Topologies*, Ph.D. thesis, Mississippi State University, May 2000. 12

[34] White, F. M., *Viscous Fluid Flow*, McGraw-Hill, New York, 3rd ed., 2006. 12

[35] Kress, J. E., *An Unstructured Grid Incompressible Navier-Stokes Algorithm for Convective Heat Transfer Based on Artificial Compressibility*, Ph.D. thesis, University of Tennessee at Chattanooga, Dec 2012. 16, 88

[36] Dittus, F. and Boelter, L., "Heat transfer in automobile radiators of the tubular type," *University of California Publications in Engineering*, Vol. 2, 1930, pp. 443–461. 23, 27, 37, 45

[37] Kline, S. and McClintock, F., "Describing uncertainty in single-sample experiments," *Mechanical Engineering*, Vol. 75, 1953, pp. 3–8. 23

[38] Schlichting, H., *Boundary Layer Theory*, McGraw-Hill, seventh ed., 1979. 27, 45

[39] Al-Hadhrami, L. M., *Rotating Heat Transfer in Turbine Rotor Blade Cooling Channels with Turbulence Promoters*, Ph.D. thesis, Texas A&M University, May 2002. 40, 41, 42, 43, 44

[40] AIAA/ASME/SAE/ASEE, *Joint Propulsion Conference & Exhibit*, San Diego, California, July 2011. 83, 84

APPENDIX

EIGENSYSTEM

EIGENSYSTEM

The flux Jacobian matrix is defined as $A = \frac{\partial F}{\partial Q}$. The entries of A are calculated by $A_{ij} = \frac{\partial F_{ij}}{\partial Q_{ij}}$, where the derivitive of the i^{th} F flux equation is taken with respect to the j^{th} Q variable. Performing these derivatives yields the following:

$$A = \begin{bmatrix} 0 & \beta n_x & \beta n_y & \beta n_z & 0 \\ \frac{n_x}{\rho} & \theta + u n_x & u n_y & u n_z & 0 \\ \frac{n_y}{\rho} & v n_x & \theta + v n_y & v n_z & 0 \\ \frac{n_z}{\rho} & w n_x & w n_y & \theta + w n_z & 0 \\ 0 & T n_x & T n_y & T n_z & 0 \end{bmatrix} \tag{1}$$

The following matrix κ is created by performing a similarity transformation on A:

$$M = \begin{bmatrix} 1 & 0 & 0 & 0 & 0 \\ \frac{u}{\beta} & 1 & 0 & 0 & 0 \\ \frac{v}{\beta} & 0 & 1 & 0 & 0 \\ \frac{w}{\beta} & 0 & 0 & 1 & 0 \\ 0 & 0 & 0 & 0 & 1 \end{bmatrix} \tag{2}$$

$$M^{-1} = \begin{bmatrix} 1 & 0 & 0 & 0 & 0 \\ -\frac{u}{\beta} & 1 & 0 & 0 & 0 \\ -\frac{v}{\beta} & 0 & 1 & 0 & 0 \\ -\frac{w}{\beta} & 0 & 0 & 1 & 0 \\ 0 & 0 & 0 & 0 & 1 \end{bmatrix} \tag{3}$$

The resulting matrix κ

$$\kappa = M^{-1} A M = \begin{bmatrix} \theta & \beta n_x & \beta n_y & \beta n_z & 0 \\ \frac{n_x}{\rho} + \frac{u}{\beta} & \theta & 0 & 0 & 0 \\ \frac{n_y}{\rho} + \frac{v}{\beta} & 0 & \theta & 0 & 0 \\ \frac{n_z}{\rho} + \frac{w}{\beta} & 0 & 0 & \theta & 0 \\ \frac{T\theta}{\beta} & T n_x & T n_y & T n_z & \theta \end{bmatrix} \tag{4}$$

The characteristic equation, $det(\kappa - I\lambda) = 0$, needs to be solved to find the eigenvalues:

$$\begin{vmatrix} \theta-\lambda & \beta n_x & \beta n_y & \beta n_z & 0 \\ \frac{n_x}{\rho}+\frac{u\theta}{\beta} & \theta-\lambda & 0 & 0 & \\ \frac{n_y}{\rho}+\frac{v\theta}{\beta} & 0 & \theta-\lambda & 0 & 0 \\ \frac{n_z}{\rho}+\frac{w\theta}{\beta} & 0 & 0 & \theta-\lambda & 0 \\ \frac{T\theta}{\beta} & Tn_x & Tn_y & Tn_z & \theta-\lambda \end{vmatrix} = 0 \tag{5}$$

Expansion of the determinant about the fourth column gives

$$(\theta-\lambda)^3\left((\theta-\lambda)^2-\theta^2-\frac{\beta}{\rho}(n_x^2+n_y^2+n_z^2)\right)=0$$

Solving this equation for λ yields:

$$\begin{gathered}\lambda_1,\lambda_2,\lambda_3=\theta \\ \lambda_4=\theta+c \\ \lambda_5=\theta-c\end{gathered}$$

where,

$$c=\sqrt{\theta^2+\frac{\beta}{\rho}(n_x^2+n_y^2+n_z^2)}$$

To finish the eigensystem, the right eigenvectors are solved according to the formula $(\kappa-\lambda_i I)R_i=0$, where R_i, is the right eigenvector corresponding to λ_i and has the following form:

$$R_i=\begin{bmatrix} r_i^1 \\ r_i^2 \\ r_i^3 \\ r_i^4 \\ r_i^5 \end{bmatrix}$$

With further details outlined in preceding research [35], the resulting matrix with the right eigenvectors as columns is:

$$E=\begin{bmatrix} 0 & 0 & 0 & c & -c \\ x_1 & x_2 & 0 & \frac{n_x}{\rho}+\frac{u\theta}{\beta} & \frac{n_x}{\rho}+\frac{u\theta}{\beta} \\ y_1 & y_2 & 0 & \frac{n_y}{\rho}+\frac{v\theta}{\beta} & \frac{n_y}{\rho}+\frac{v\theta}{\beta} \\ z_1 & z_2 & 0 & \frac{n_z}{\rho}+\frac{w\theta}{\beta} & \frac{n_z}{\rho}+\frac{w\theta}{\beta} \\ 0 & 0 & 1 & \frac{T}{c}\phi_1 & \frac{-T}{c}\phi_2 \end{bmatrix} \tag{6}$$

where

$$\begin{aligned}\phi_1&=\tfrac{1}{\rho}(n_x^2+n_y^2+n_z^2)+\tfrac{\theta}{\beta}\lambda_4 \\ \phi_2&=\tfrac{1}{\rho}(n_x^2+n_y^2+n_z^2)+\tfrac{\theta}{\beta}\lambda_5\end{aligned}$$

With E and E^{-1} being the eigenvector matrices for κ, R and L, the right and left eigenvector matrices for A can be computed by the relations $R = ME$, and $L = E^{-1}M^{-1}$. Applying these relations, the eigenvector matrices may be expressed as:

$$R = \begin{bmatrix} 0 & 0 & 0 & c & -c \\ x_1 & x_2 & 0 & \frac{uc}{\beta} + \phi_3 & -\frac{uc}{\beta} + \phi_3 \\ y_1 & y_2 & 0 & \frac{vc}{\beta} + \phi_4 & -\frac{vc}{\beta} + \phi_4 \\ z_1 & z_2 & 0 & \frac{wc}{\beta} + \phi_5 & -\frac{wc}{\beta} + \phi_5 \\ 0 & 0 & 1 & \frac{T}{c}\phi_1 & \frac{-T}{c}\phi_2 \end{bmatrix} \tag{7}$$

$$L = \frac{1}{det(E)} \begin{bmatrix} -\frac{2c}{\beta}(u(y_2\phi_5 - z_2\phi_4) & & & & \\ +v(z_2\phi_3 - x_2\phi_5) & 2c(y_2\phi_5 - z_2\phi_4) & 2c(z_2\phi_3 - x_2\phi_5) & 2c(x_2\phi_4 - y_2\phi_3) & 0 \\ +w(x_2\phi_4 - y_2\phi_3)) & & & & \\ -\frac{2c}{\beta}(u(z_1\phi_5 - y_1\phi_5) & & & & \\ +v(x_1\phi_5 - z_1\phi_3) & 2c(z_1\phi_4 - y_1\phi_5) & 2c(x_1\phi_5 - z_1\phi_3) & 2c(y_1\phi_3 - x_1\phi_4) & 0 \\ +w(y_1\phi_3 - x_1\phi_4)) & & & & \\ -\frac{T}{2c^2}(\phi_1 + \phi_2)det(E) & & & & \\ -\frac{T}{\beta}(\phi_2 - \phi_1)\theta & Tn_x(\phi_2 - \phi_1) & Tn_y(\phi_2 - \phi_1) & Tn_z(\phi_2 - \phi_1) & det(E) \\ \frac{det(E)}{2c} - \frac{c\theta}{\beta} & cn_x & cn_y & cn_z & 0 \\ -\frac{det(E)}{2c} - \frac{c\theta}{\beta} & cn_x & cn_y & cn_z & 0 \end{bmatrix} \tag{8}$$

VITA

Guy Austin Flynt was born in Rogersville, Tennessee in June of 1985, to the parents of Guy and Pegi Flynt. After graduating from Forest Lake Academy in Orlando, FL, he went on to complete a Bachelor's of Science degree in Mechanical Engineering at the University of Tennessee at Chattanooga, graduating in December, 2010 summa cum laude. Austin accepted a graduate research assistantship in the Sim Center at the University of Tennessee at Chattanooga, where he persued an M.S. degree in Computational Engineering. Austin plans to pursue a career in Aerospace/CFD engineering.